Changes in the Kuroshio and North Equatorial Current during the last 35,000 years

楊　海燕

(Yang Haiyan)

2022

Abstract

The last glacial age was characterized by millennial-scale climate variations and sea-level changes. Although the path and intensity of the Kuroshio Current (KC) during the last glacial age have been studied extensively, changes in the Kuroshio are still poorly understood because of limited observations and incomplete model configurations. Moreover, the North Equatorial Current (NEC), the upstream source of the KC whose bifurcation latitude determines the partitioning of the water mass as well as the heat transport between the KC and the Mindanao Current, also remains unexplored. Therefore, it is necessary to explore changes in the NEC in the paleo-ocean in terms of intensity and bifurcation location.

Using an improved ocean model and paleoclimate air–sea forcing field provided by multiple climate models, we explored the ensemble mean of changes in the Kuroshio region during the Last Glacial Maximum (LGM, ~ 21 ka BP) and carried out a preliminary evaluation of these models with the available sea surface temperature (SST) proxy observations. In addition, based on the results of Model for Interdisciplinary Research on Climate (MIROC4m), we further simulated the changes in the Kuroshio and North Equatorial Current from 35,000 years ago to the present.

Ensemble mean of SST from 10 LGM models indicated a cooling of 1.9 ± 0.5°C in the 15° S–15° N latitude band. According to model outputs of the East China Sea (ECS), a significant cooling exceeding 5°C occurred on the nearshore side along the KC axis, and a cooling of 1–2°C occurred on the offshore side. The ΔSST in the Pacific Ocean east of the Ryukyu Islands was approximately -2°C during the LGM. The SST cooling exceeded 6°C in the Japan Sea and the Kuroshio–Oyashio confluence region at 40° N, exhibiting the largest discrepancy among all model outputs. Model evaluation revealed that GISS-E2-R in Paleoclimate Modelling Intercomparison Project Phase 3 (PMIP3) performed best for both annual and summer mean

ΔSST simulations, whereas MIROC-ES2L in Paleoclimate Modelling Intercomparison Project Phase 4 (PMIP4) performed the poorest.

The KC at 6 ka BP had the same path, volume transport, and strength as the modern KC. Regardless of changes in the sea-level and climate, the KC path remained inside the ECS. However, the glacial Kuroshio transport increased and the KC axis migrated slightly seaward. The ensemble mean of the ten models also confirmed that the Kuroshio axis migrates slightly seaward with an increase in volume transport in the ECS. With a lowering sea level and variations in climate during glacial times, the Kuroshio path south of Japan shifted northward. The Kuroshio Extension shifted southward within a range of 0.5 to 3.5°, depending on the longitude.

Relative to the present location of the NEC bifurcation, the bifurcation latitude at the surface (500 m) was southward by 0.1° (0°), 0.9° (2.9°), 1.0° (3.0°), and 0.7° (2.4°) at 6 ka BP, LGM, 30 ka BP, and 35 ka BP, respectively. This southward movement at the surface corresponds to the southward shift of the zero-wind-stress curl lines. However, the 10 LGM model results did not yield a correspondence between the latitudinal shift of the NEC bifurcation and the location of the zero wind-stress curl. Furthermore, NEC bifurcation exhibited a poleward tilting with increasing depth in the paleo-ocean, and the degree of tilting did not entirely depend on the ratio of the wind stress curl intensity of the subtropical gyre to that of the tropical gyre.

The North Pacific subtropical gyre, including its southern and northern boundaries (i.e., NEC and Kuroshio Extension), had shifted southward during the glacial age, which was associated with changes in the wind-stress curl over the North Pacific. As found in the modern ocean, the latitudinal shift of the NEC bifurcation was highly correlated with changes in NEC and KC transport, and the southward shift of the NEC bifurcation resulted in an intensified upstream Kuroshio. When the NEC bifurcation shifted southward during the last glacial period, the NEC and its northern branch (i.e., Kuroshio) were enhanced. Consequently, the Kuroshio transport increased with higher surface velocity in the southern and middle ECS.

Considering the strength of Kuroshio, the horizontal gradient of the subsurface temperature may be a better indicator than the commonly used palaeoceanographic index upper-ocean vertical thermal gradient.

Table of contents

List of Tables

List of Figures

Chapter 1: Introduction

1.1 Background

The Kuroshio Current (KC) originates in the northern branch of the North Equatorial Current (NEC) at approximately 15° N to the east of the Philippine coast and is a strong western boundary current in the North Pacific. The KC continues northward, entering the Okinawa Trough via the Yonaguni Depression off the eastern coast of Taiwan, flowing along the continental slope of the East China Sea (ECS), and eventually turning eastward through the Tokara Strait. After passing south of Japan, the KC separates from the coast of Japan and flows eastward as the Kuroshio Extension (KE). The Kuroshio transports warm water from the tropics to mid-latitudes, and variations in its path and volume transport may profoundly influence the climate in East Asia (Gallagher et al., 2015; Kim et al., 2017).

The KC and the Mindanao Current (MC) are the two northward and southward branches bifurcated from the NEC along the Philippine coast. Eventually, the two western boundary currents return to the KE and North Equatorial Countercurrent (NECC) (Toole et al., 1990). NEC is generally regarded as both the southern limb of the subtropical gyre and the northern limb of the tropical gyre (Toole et al., 1990; Z. Zhang et al., 2017). The bifurcation latitude of the NEC is related to the partitioning of the NEC mass and heat between the KC and MC. This determines the extent to which subtropical water penetrates tropical circulation through the MC and how much it turns poleward to subtropical circulation through the Kuroshio (Qu & Lukas, 2003).

Changes in ice sheets over timescales of 10^3–10^5 years play important roles in sea-level variations (Yokoyama et al., 2019). The Last Glacial Maximum (LGM, ~ 21 ka BP) is a glacial period during which the global surface air temperature cooled by 4.0–7.0 ± 1.0 °C (Annan &

Hargreaves, 2013), with significantly different climatic conditions from that of the present. Large ice sheets over North America and Northern Europe characterized the LGM, and previous observations indicated a fall in sea-level fall by 130–140 m during this period (Clark et al., 2009; Lambeck et al., 2014; Yokoyama et al., 2018). However, this was followed by a comparably rapid rise in sea level that started around 20 ka BP, and the sea-level changes did not slow down until 6 ka BP (Figure 1.1). The global mean sea level increased by more than 100 m between 20 and 6 ka BP, driven by melting ice sheets.

Paleoclimate modeling provides an opportunity to study changes in climatic and oceanic conditions, and numerous climate models in the PMIP have been used to simulate the climate of the LGM (Kageyama et al., 2021). Multiple PMIP models have shown that the westerly jet at 850 hPa shifted southward over the North Pacific during the LGM (N. Wang et al., 2018b). However, these climate models still exhibit problems with the quality of the regional ocean flow because of their coarse resolution (Nooteboom et al., 2022).

In addition, geochemical proxies and foraminiferal species assemblages have been used to investigate millennial-scale changes in the strength and location of the Kuroshio, but they suffer from low spatial and temporal resolution and offer uncertainty in the path of the paleo-Kuroshio (Gallagher et al., 2015; Ijiri et al., 2005; Kawahata & Ohshima, 2002; Q. Li et al., 2020; Sawada & Handa, 1998; Thompson & Shackleton, 1980; H. Ujiié & Ujiié, 1999; Y. Ujiié et al., 2003; Yamamoto, 2009). In recent decades, ocean models have contributed to further research on the variability in the Kuroshio since the LGM (Kao et al., 2006; Lee et al., 2013; Vogt-Vincent & Mitarai, 2020; Zheng et al., 2016), but the results have been inconsistent in terms of the Kuroshio path and intensity.

1.2 Motivation and Thesis Outline

The coupled atmosphere-ocean models of PMIP, with global coverage, are too coarse to study the regional variability of the Kuroshio. Moreover, a few observations have given rise to speculation on the variability of the paleo-Kuroshio, and understanding the evolution of the paleo-Kuroshio remains difficult due to significant spatial and temporal limitations. Although the model resolved spatial insufficiency in observations, such models studying the paleo-Kuroshio have focused on the ECS, neglecting the changes in the KE and its source (i.e., NEC). Thus far, the millennial-scale variability of the Kuroshio system, including the NEC and KE, remains unclear.

The condition of the KC is affected by millennial-scale changes in the atmosphere and equatorial Pacific (Ujiié et al., 2016). The KE dynamics are influenced by wind forcing over the mid-latitude North Pacific, and KE variability is mainly due to westward-propagating mesoscale eddies from the central and eastern regions of the North Pacific (Qiu, 2003; Qiu et al., 2014; Sasaki & Schneider, 2011). Therefore, a large-scale ocean model for studying the Kuroshio region, including the KE system, is necessary.

In this thesis, the global climate model is downscaled to an ocean model which considers the climatic (air-sea heat flux and wind stresses) and sea-level changes across the whole North Pacific, making it possible to obtain an ensemble of changes in the Kuroshio region at the LGM based on the results of multiple climate models from PMIP. Additionally, the downscaled ocean model will help to explore how the Kuroshio system (i.e., KC, KE, and NEC) responds to the combined changes in five historical ages- 0 (i.e., present), 6, 21 (i.e., LGM), 30 and 35 ka BP. This thesis is organized as follows:

Chapter 1 provides a general introduction to the background of the research and an outline of the thesis.

Chapter 2 describes the input data and configuration of the ocean model, followed by validation of the model.

Chapter 3 discusses the ensemble mean of ten LGM climate models in the Kuroshio region, including the Kuroshio volume and NEC bifurcation. The reconstructed paleo-SST data were used for preliminary model evaluation.

Chapter 4 shows the changes in the Kuroshio (i.e., path, surface current, and strength) and NEC bifurcation from 35 ka BP and explains the reasons for these changes.

Chapter 5 summarizes the thesis research and describes plans for future research.

Figures

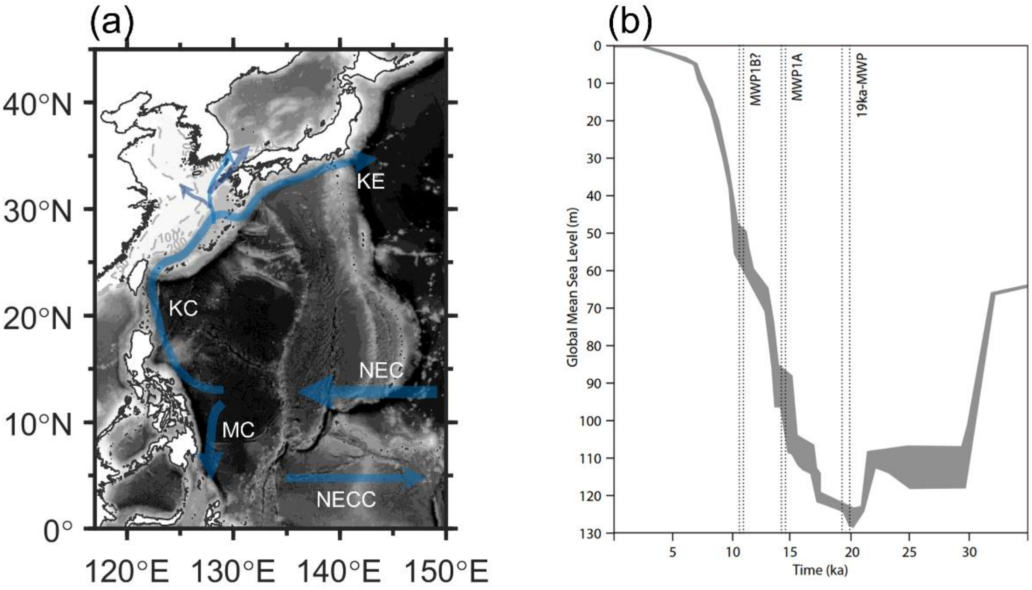

Figure 1.1 (a) Northwest Pacific Ocean bathymetry (shaded colors; unit: m) and ocean circulation (semitransparent blue arrows) map. The acronyms NEC, NECC, MC, KC, and KE stand for North Equatorial Current, North Equatorial Countercurrent, Mindanao Current, Kuroshio Current, and Kuroshio Extension, respectively. (b) Newly obtained global mean sea levels from fossil coral reef materials obtained from the Great Barrier Reef during the Integrated Ocean Drilling Program Expedition 325 combined with data from a glacial hydro isostatic adjustment model. Dotted lines represent previously proposed rapid melting events since the Last Glacial Maximum. (Figure and caption sourced from Yokoyama et al., 2019).

Chapter 2: Model description and validation

2.1 Introduction

Previous studies have sought to infer changes in water temperatures at the LGM using various proxies (foraminiferal, radiolarian, diatom, and geochemical proxies). Reconstructed SSTs in the Kuroshio region have been used to explore the intensity and position of the Kuroshio (Chang et al., 2008; Ijiri et al., 2005; Kubota et al., 2017; Ruan et al., 2017; Sawada & Handa, 1998; Vats et al., 2020). The sedimentary features and biogeographic patterns from the proxies reflect the regional oceanographic features.

In recent decades, some ocean models have been used to explore the effect of sea-level lowering on the Kuroshio in the Okinawa Trough (Kao et al., 2006; Lee et al., 2013; Zheng et al., 2016), but they were configured with low horizontal resolutions (e.g., 1/8° or coarser than 1°), which are insufficient to resolve eddies. Moreover, a high-resolution ocean model that considered climate change (Vogt-Vincent & Mitarai, 2020) excluded the NEC and KE regions. Therefore, the results were largely limited by the specified boundary conditions.

The LGM experiment and corresponding pre-industrial (PI) control experiments (representing 1850 CE) were carried out using the coupled atmosphere-ocean models in the PMIP. The LGM helps understand the response of climate models to large changes in radiative forcing (Annan & Hargreaves, 2013). However, the coupled atmosphere-ocean general circulation models have problems with simulating regional climate and flow correctly because of the coarse resolution (1° or coarser horizontally for the ocean) (Delworth et al., 2012; Griffies et al., 2015; Hewitt et al., 2020; Nooteboom et al., 2020). Compared with the low-resolution climate model, the high-resolution model showed a higher surface temperature near Antarctica and a lower value near the equator, which agree better with the reconstructed values (Nooteboom et al., 2022). In addition, Kirtman et al. (2012) used the climate model with eddy-resolving resolution (1/12°) that showed marginal improvement in depicting the SST-wind stress relation than with eddy-permitting resolution (1/4°).

The spatial resolution of the global climate models is too coarse to resolve mesoscale eddies in the ocean. The Kuroshio region is characterized by active mesoscale eddy activity, and the magnitude of the eddy kinetic energy in the model strongly depends on the model resolution (Hewitt et al., 2020). A higher-resolution model can simulate more realistic mesoscale eddies, including their magnitude and movements and therefore can represent their influence on the KC and KE.

To confirm this point, we show the annual mean sea levels in Figure 2.1a and 2.1b calculated from the final 5-year daily data in 1/4° and 1/12° models. Sea surface height (SSH) variability is related to mesoscale activities. We calculated the root mean square (RMS) amplitude of the model sea level to show the SSH variability in each model (Figure 2.1c and 2.1d). RMS of the model sea level is defined as $\sqrt{\frac{1}{N-1}\sum_{i=1}^{N}(\eta_i - \bar{\eta})^2}$, where η_i denotes the SSH of the ith data in a time series and $\bar{\eta}$ is the average of η_i over all data N. As shown in these figures, the Kuroshio Extension region is very sensitive to model resolution because of the presence of high mesoscale eddy activity in the North Pacific (Qiu & Chen, 2010). In addition, the mean positions of KC and KE were also slightly different between these two models.

Here, our eddy-resolving ocean model, with horizontal resolution 1/12°, considers the climatic (i.e., air-sea heat flux and wind stresses) and sea-level changes over the entire North Pacific. The regional ocean model was used to downscale the climate models from PMIP3, PMIP4, and MIROC4m in Chapters 3 and 4. These models showed significant differences in the simulations of SST and ocean currents.

2.2 Data and methods

2.2.1 Calculation of net air-sea heat flux

The net air-sea heat flux entering the ocean (Q_{net}) includes net short-wave solar radiation (Q_{sw}), net long-wave radiation (Q_{lw}), latent heat flux due to evaporation (Q_{lat}), and sensible heat flux due to air and water with different surface temperatures (Q_{sen}): $Q_{net} = Q_{sw} + Q_{lw} + Q_{lat} + Q_{sen}$. The different parts were calculated as follows.

1) Net short-wave solar radiation (Q_{sw}):

$$Q_{sw} = \mathrm{Q}_s^{sky}\{0.77 - 0.5C^2\}(1.0 - \alpha), \tag{2.1}$$

where Q_s^{sky} is the solar radiation incident on the ocean under clear sky, C is the fraction of cloud cover ($0 \le C \le 100$), and α is the ocean surface albedo set at 0.08.

2) Net long-wave radiation (Q_{lw}):

$$Q_{lw} = \varepsilon\sigma(t_s)^4\left(0.39 - 0.05\sqrt{e_a}\right)\{1.0 - 0.8C\} + 4.0\varepsilon\sigma(t_s)^3(t_s - t_a), \tag{2.2}$$

where ε is the emissivity of the ocean (ε=0.97), σ is the Stefan–Boltzmann constant (σ = 5.67 × 10^{-8} W m^{-2} K^{-4}), t_s is SST, t_a is 2 m air temperature, and $e_a$is vapor pressure as estimated from q_a (specific humidity).

3) Latent heat flux (Q_{lat}):

$$Q_{lat} = L\rho_a C_E\sqrt{{u_{2m}}^2 + {v_{2m}}^2}(q_s - q_a), \tag{2.3}$$

L is the latent heat of fusion equal to 2.501×10^6 J kg^{-1}, ρ_a is the air density at sea level equal to 1.225 kg m^{-3}, $C_E$is the turbulent exchange coefficient estimated based on the formulas of Kondo (1975), and u_{2m} and v_{2m} are the zonal and meridional wind velocities at 2 m above sea level, respectively. They were transferred from a wind speed of 10 m according to the logarithmic wind speed (Kondo, 1975). q_s is the saturated specific humidity:

$$q_s = \frac{0.622\times(6.1078\times)10^{\frac{7.5\times(t_S-273.15)}{t_S}}}{1-0.378\times(6.1078\times10^{\frac{7.5\times(t_S-273.15)}{t_S}})}.$$

4) Sensible heat flux (Q_{sen}):

$$Q_{sen} = c_p \rho_a C_H \sqrt{{u_{2m}}^2 + {v_{2m}}^2}(t_s - t_a), \tag{2.4}$$

c_p is the specific heat capacity equal to 1.005 × 10^3 J kg^{-1} K^{-1}, and C_H is the turbulent exchange coefficient based on the formula of Kondo (1975).

2.2.2 Data for 0 ka BP and model settings

Based on the above equations, the air-sea heat flux and wind stresses were calculated from monthly climatological data derived from the 6-hourly Environmental Prediction/National Center for Atmospheric Research (NCEP/NCAR) reanalysis data during the 1992–2017 period, which was regarded as the standard 0 ka BP data in the study.

The Stony Brook Parallel Ocean Model (sbPOM), which is a parallel sigma-coordinate ocean circulation model based on the Princeton Ocean Model (POM) developed by Jordi and Wang (2012) was used. The model domain covered the entire North Pacific and part of the South Pacific (30° S–62° N, 100° E–90° W) with a horizontal resolution of 1/12° and 47 sigma levels in the vertical direction (Figure 2.2b). The model bathymetry was prepared from ETOPO1, which is a 1 arc-minute global relief model of the Earth's surface (Amante & Eakins, 2009). In the model, the minimum and maximum depths were set to 10 m and 6500 m, respectively. The topography was smoothed as $\frac{|H_{i+1}-H_i|}{H_{i+1}+H_i} \leq 0.2$, where H_{i+1}, H_i are two adjacent cells.

The models were driven by wind stress, heat flux, and salt flux at the sea surface. Retroaction terms with climatological monthly SST and SSS were added to the surface heat fluxes and salt fluxes, which were 35 W m^{-2} K^{-1} and 10 m/month, respectively.

Each model was forced from an initial no-motion condition with monthly climatological temperature and salinity. We used the gridded 0.25° × 0.25° climatological monthly mean temperature and salinity data from WOA2018 (Locarnini et al., 2019; Zweng et al., 2019) for 0 ka BP. In addition, the model was forced by the climatological monthly mean heat flux and wind stresses and was subsequently integrated for 30 years. The final 5-year results were used in the analysis.

2.3 Validity of the model

To verify the model results, the zonal velocity and potential density along 137 °E are shown in Figure 2.3a, where the strong current at ~33 °N is the Kuroshio, which generally flows eastward along the southern coast of Japan. The NEC, i.e., the origin of the Kuroshio, flows westward in the area between 8 and 15° N, and the NECC can be found south of the NEC in the upper 200 m from the sea surface. Both the current and density contours were consistent with the corresponding observations of Qiu et al. (2017). In addition, other currents, such as the westward South Equatorial Current (SEC), eastward NECC, Equatorial Undercurrent (EUC), and North Intermediate Countercurrent (NICC), have been shown in the section along 143° E (Figure 2.3b), and the distribution was comparable to the mooring observations of Zhang et al. (2018).

In addition, compared to the 20-year (i.e., 1993–2013) average annual mean SST calculated by the Japanese Ocean Flux Data Sets with Use of Remote Sensing Observations 3 (J-OFURO3; Tomita et al., 2019) (https://j-ofuro.isee.nagoya-u.ac.jp), our model can reproduce the SST distribution and values better (Figure 2.4). The highest temperature exists in the warm pool located in the western Pacific, with a value exceeding 27° C. The spatial correlation coefficient between the modeled SSTs and SSTs in J-OFURO3, based on 200359 grid points, was 0.99.

Figure 2.5a shows the annual mean surface current in KC and KE region at 0 ka BP. The KC originates from the NEC and intrudes into the South China Sea in a looping path through the Luzon Strait. After entering the ECS, the KC flows northeastward along the 200 m isobath and exits through the Tokara Strait. In the area south of Japan, the Kuroshio shows an offshore meander southeast of the Kii Peninsula. After that, the KC enters the open basin of the North Pacific and becomes the eastward KE. This result is in agreement with the 25-year (1993–2017) mean velocity field obtained by a combination of the satellite data and model results generated by AVISO (Figure 2.5b, Rio et al., 2014) (https://resources.marine.copernicus.eu/products).

Figures

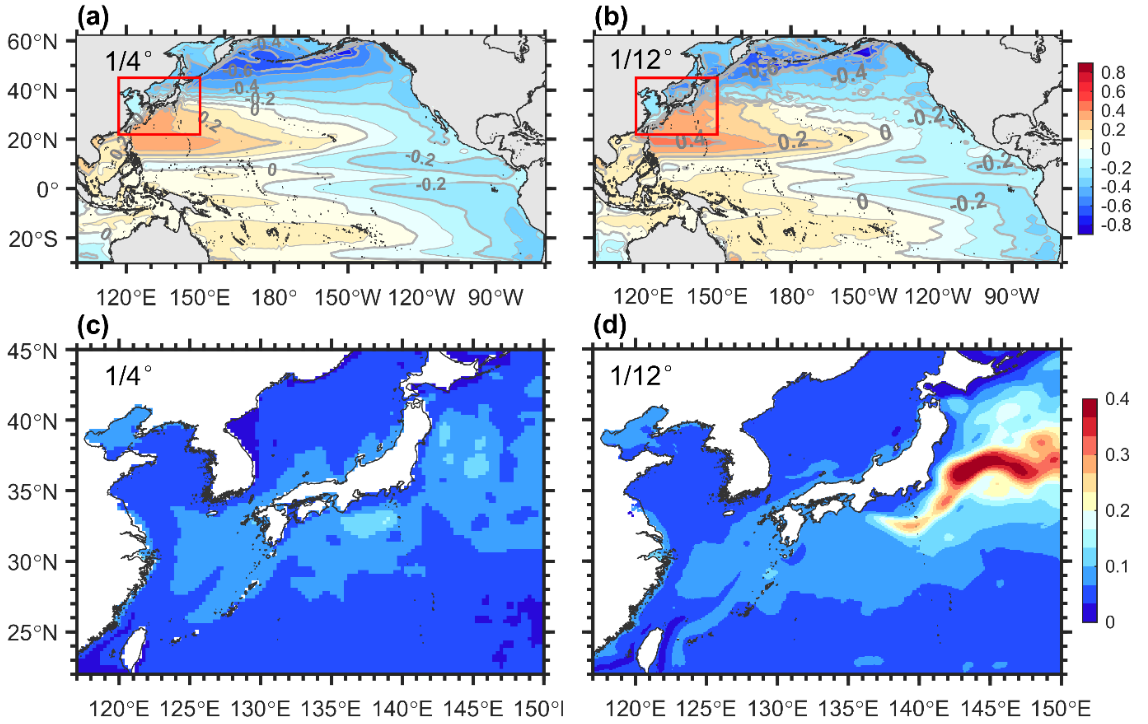

Figure 2.1 Annual mean sea levels (unit: m) in (a) 1/4° model and (b) 1/12° model. The RMS of sea surface height (SSH) (unit: m) in the red box (c) 1/4° model and (d) 1/12° model.

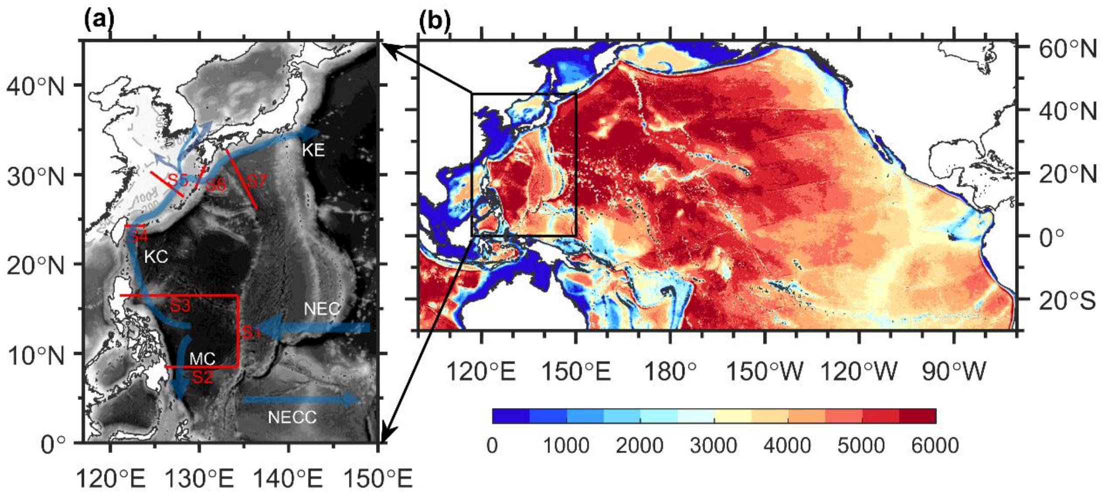

Figure 2.2 (a) Northwest Pacific Ocean bathymetry (shaded colors; unit: m) and ocean circulation (semitransparent blue arrows) map. Red lines indicate sections used for volume transports in Table 3.1. (b) Domain and bathymetry chart of the model. Colors indicate model bathymetry (unit: m).

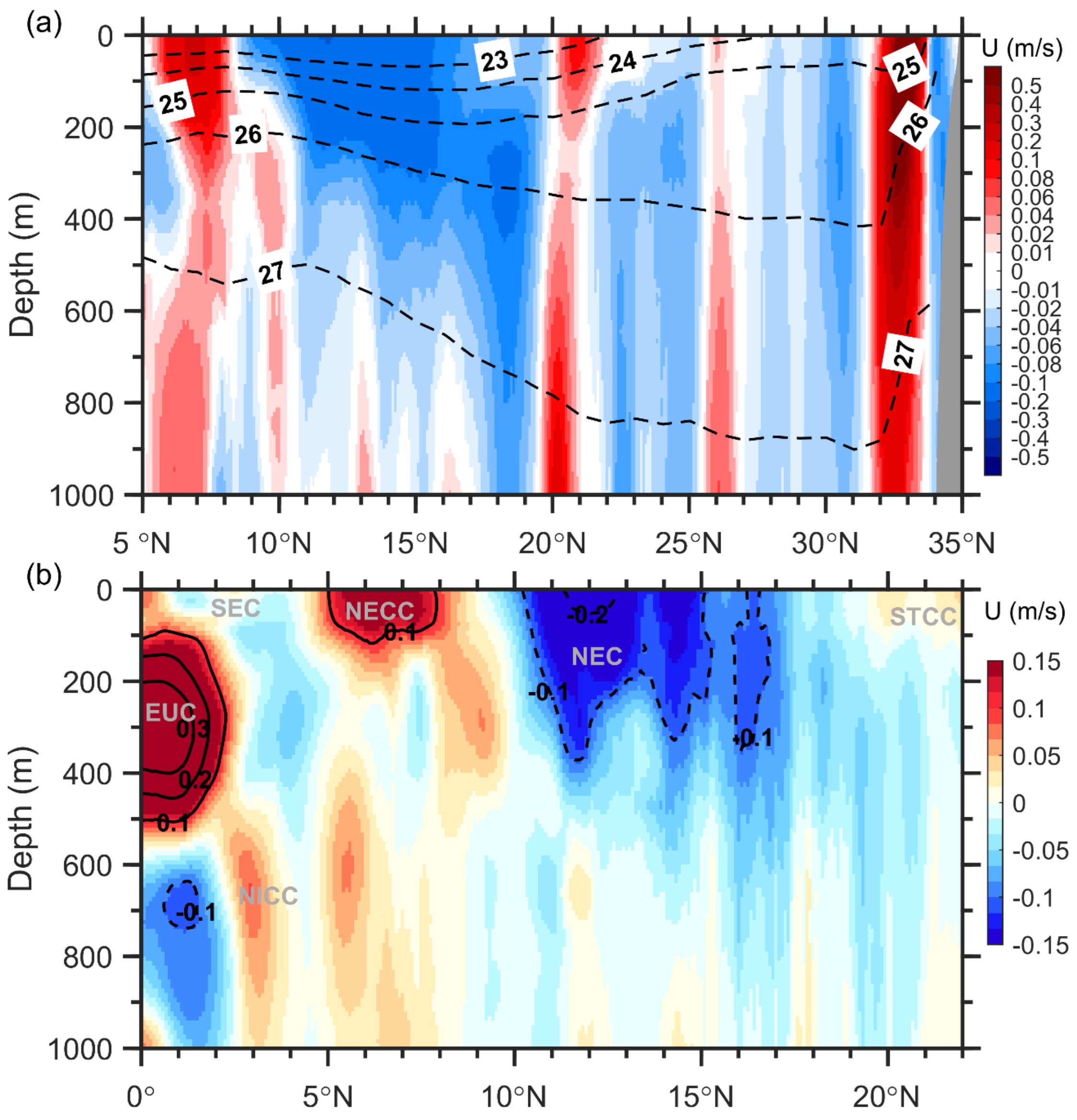

Figure 2.3 (a) Annual mean zonal velocity (color shaded) and potential density $\boldsymbol{\sigma_\theta}$ (dotted black contours) at a section along 137° E. (b) Annual mean zonal velocity at a section along 143° E. Shaded colors with contours indicate the zonal velocity U (unit: m/s); The acronyms SEC, EUC, NECC, NEC, NICC, and STCC stand for South Equatorial Current, Equatorial Undercurrent, North Equatorial Countercurrent, North Equatorial Current, North Intermediate Countercurrent, and Subtropical Countercurrent, respectively.

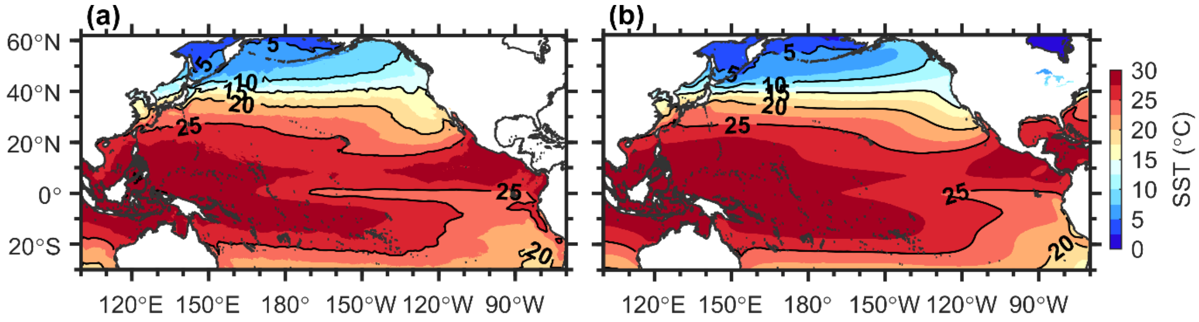

Figure 2.4 Comparison of the distribution of annual mean sea surface temperature (SST) between (a) model results at 0 ka BP and (b) 20-year annual mean values from J-OFURO3.

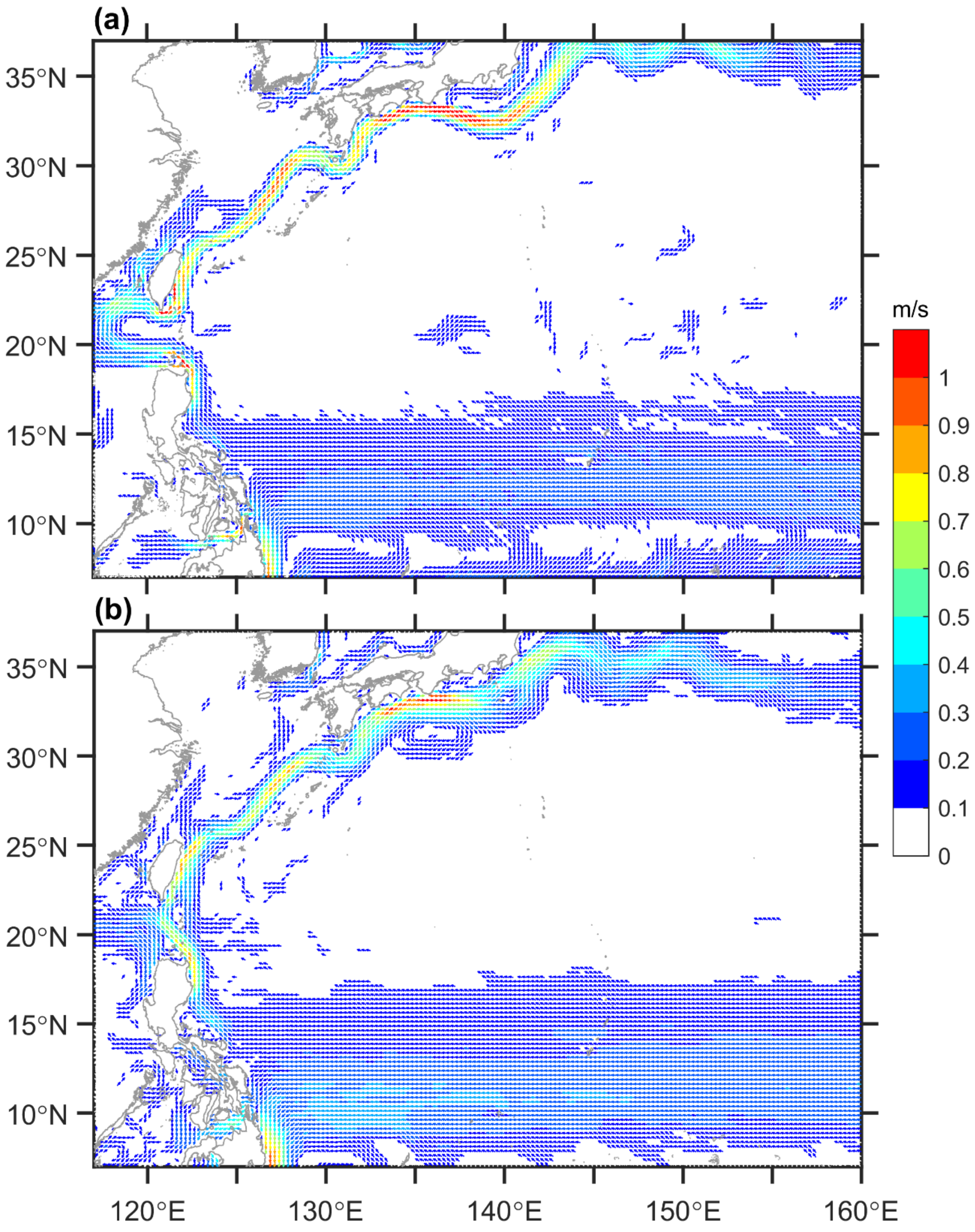

Figure 2.5 Comparison of the annual mean surface current between (a) model results at 0 ka BP and (b) observed current derived from satellite altimetry data (1993–2017).

Chapter 3: Ensemble of the Kuroshio and North Equatorial Current during the Last Glacial Maximum

3.1 Introduction

Ocean models have significantly improved our understanding of the paleo-KC, especially that during the LGM. Earlier models have shown that the KC entered the Okinawa Trough during the LGM (Kao et al., 2006; Lee et al., 2013; Vogt-Vincent & Mitarai, 2020; Zheng et al., 2016), while Kao et al. (2006) showed that the Kuroshio mainstream flowed out of the Okinawa Trough through the Kerama Gap instead of the Tokara Strait, with a sea level 135 m lower than the level today. These simulations presented a stronger Kuroshio surface current in the ECS during the LGM relative to the present (Kao et al., 2006; Lee et al., 2013; Vogt-Vincent & Mitarai, 2020), but the mechanism of the enhanced Kuroshio has not been adequately explained. Most modeling studies have considered only the effect of sea-level lowering on the KC, using low-resolution models that were unable to adequately resolve eddies. Moreover, earlier regional models, which were greatly restricted by specified boundary conditions from climate models, focused on the ECS, but excluded the KE system.

A large-scale ocean model for studying the Kuroshio region, including the KE system, which has an active ocean-atmosphere interaction in the North Pacific and plays a crucial role in the climate and ecosystem, is therefore necessary. Basin-scale atmospheric forcing can influence the Kuroshio meanders south of Japan as well as the KE (Nonaka et al., 2012; Saito et al., 2019). It has been indicated that the westerly jet stream over the North Pacific during the LGM was south of its present position (Gray et al., 2020; Wang et al., 2018; Yanase & Abe-Ouchi, 2010). However, few existing modeling studies have explicitly explored the relative extent of the paleo-KE under the combined influences of sea level and climate.

In addition to the analysis of models, another major issue concerning the paleo-KC is the Okinawa Trough and KE region during the LGM based on different proxies such as geochemical and foraminiferal proxies. The KC was thought to be deflected eastward into the Pacific because of the land bridge between the Ryukyu Arc and Taiwan during the LGM (Ahagon et al., 1993; Ujiie et al., 1991; Ujiié & Ujiié, 1999; Ujiié et al., 2003), but recent proxies inside the Okinawa Trough indicate the inflow of the KC into the ECS during the LGM (Amano & Itaki, 2016; Ijiri et al., 2005; Kawahata & Ohshima, 2004; Kim et al., 2015; Li et al., 2018; Xu & Oda, 1999). However, observation interpolations are still constrained by spatial shortages and proxy uncertainties.

For the central tropical Pacific, the Multiproxy Approach for the Reconstruction of the Glacial Ocean Surface (MARGO) project found little to no SST change (Waelbroeck et al., 2009), but Monteagudo et al. (2021) suggested a ~2°C cooling during the LGM. With regard to SST in the equatorial Pacific, previous studies offered different opinions: one proposed a more pronounced cooling in the eastern equatorial Pacific (Tierney et al., 2020), but others proposed a greater cooling in the western equatorial Pacific (Ford et al., 2015). Consequently, the spatial pattern of tropical Pacific SST changes remains unclear.

Above all, it is necessary to investigate the ensemble mean of the changes in the Kuroshio region and equatorial Pacific using multiple climate models. The remainder of this paper is organized as follows. Section 3.2 introduces information about climate models and methods. Section 3.3 presents the ensemble mean of the Kuroshio axis, the volume transport, and NEC bifurcation. It then shows a preliminary evaluation of the LGM model based on the available reconstructed annual mean SSTs and summer mean SSTs. Section 3.4 gives a summary.

3.2 Data and methods

3.2.1 Input data and model description

The available model outputs were required to finish the PI experiment at 1850 CE and the LGM experiments; therefore, we chose nine PMIP models (six models from PMIP3 and three models from PMIP4), which are listed as follows: CNRM-CM5, GISS-E2-R, MIROC-ESM, MRI-CGCM3, CCSM4, MPI-ESM-P, AWI-ESM, MIROC-ES2L, and MPI-ESM1-2 See Table 3.1 for more information). In the following sections, these models are abbreviated as CNRM, GISS, MIROC, MRI, CCSM, MPI, AWI4, MIROC4, and MPI4, respectively. In addition to the nine PMIP models, a Model for Interdisciplinary Research on Climate (MIROC4m) is also available to provide useful data. We analyzed the changes in the Kuroshio region and NEC bifurcation during the LGM using ten coupled atmosphere-ocean models.

In both PMIIP3 and PMIP4, the PI experiment at 1850 CE was used as the control run, and the boundary conditions in the LGM experiment included changes in Earth's orbital parameters, ice-sheet extent, land-sea distribution, and atmospheric greenhouse gas concentrations relative to the PI experiment. Changes in ocean bathymetry during the LGM depend on the area of large continental ice sheets. The ice sheet for the LGM experiment in PMIP4 can be set to one of three different ice sheet reconstructions: PMIP3 (Abe-Ouchi et al., 2015), ICE-6G_C (Peltier et al., 2015), or GLAC-1D (Ivanovic et al., 2016).

Regarding MIROC4m, the atmospheric model was employed with 2.8° horizontal resolution and 20 sigma levels, whereas the ocean model had approximately 1.4° horizontal resolution and 43 vertical levels (Chan et al., 2011).

Based on the monthly mean meteorological and oceanic data, the net air-sea heat flux (Q_{net}) at the LGM for MIROC4m was calculated from the equations in section 2.2.1. The climatological monthly mean net air-sea heat flux (Q_{net}) in the PMIP model was calculated from surface downwelling shortwave radiation, surface upwelling shortwave radiation, surface downwelling longwave radiation, surface upwelling longwave radiation, surface latent heat flux, and surface sensible heat flux in contrast to that from MIROC4m.

For the original low-resolution oceanic data from climate models, inter-model comparisons indicated significant differences in the Kuroshio axis and changes in LGM ΔSST for the ten models (Figure 3.1) because of their different boundary conditions. Low-resolution ocean models are not sufficient to capture regional flow accurately (Nooteboom et al., 2022). These independent models demonstrate a large degree of uncertainty in the ocean environment during the LGM.

To remove the bias between NCEP/NCAR and each climate model, we regarded NCEP/NCAR reanalysis data as the standard 0 ka BP and modified the wind stress heat flux and eastward and northward wind-stress components for the LGM experiments using the following equation:

$$\mathrm{F}(\mathrm{x},\mathrm{y}) = \mathrm{F_o}(\mathrm{x},\mathrm{y}) - \Delta\mathrm{F}(\mathrm{x},\mathrm{y}),$$

where $\mathrm{F}(\mathrm{x},\mathrm{y})$ and $\mathrm{F_o}(\mathrm{x},\mathrm{y})$ denote the modified and original monthly averaged variables of each climate model, respectively, and $\Delta\mathrm{F}(\mathrm{x},\mathrm{y})$ is the bias for the same variable between PI in the climate model and standard 0 ka BP (NCEP/NCAR). The correction was applied to the net air-sea heat flux and eastward and northward wind-stress components.

The model settings are introduced in Section 2.2.2. The topographies for the ten LGM models were same, with the sea level lowered by 130 m compared to the present level. For each LGM model, both surface and boundary conditions were provided by the PMIP3/PMIP4 output, and each model was forced from an initial no-motion condition with modified monthly climatological temperature and salinity. In addition, the model was forced by the climatological monthly heat flux and wind stresses and was subsequently integrated for 30 years. The final 5-

year results were used in the analysis. The mean of the multi-model ensemble was obtained using the same weights.

3.2.2 Methods

In this section, based on the annual mean current, the upper 1000 m integrated volume transport stream function is calculated as

$$\Psi(x, y) = \int_{x_E}^{x} \int_{-1000m}^{0} v(x, y, z) dz dx, \tag{3.1}$$

where Ψ is the stream function, x_E denotes the eastern boundary of the Pacific, and $v(\mathrm{x}, \mathrm{y}, \mathrm{z})$ is the northward velocity at points with x, y, and z coordinates (i.e., longitude, latitude, and depth, respectively).

The NEC bifurcates at the eastern coast of the Philippines and forms the southward MC and northward KC. As defined, the NEC bifurcation latitude is the point where the averaged meridional flow within 2° band off the Philippine coast is zero (Kim et al., 2004). We didn't consider the NEC bifurcation around the Luzon Strait (17°N–22° N). The model results show that the bifurcation latitude was located at 13.3° N at the surface at 0 ka BP.

3.3 Results and discussion

3.3.1 Ensemble of the Kuroshio path and transport

As mentioned in Section 2.1, we calculated the root mean square (RMS) amplitude of the model sea level to show mesoscale activities in each model. As shown in Figure 3.2, the mesoscale variation in the Kuroshio region is different among the LGM models, especially in the KE region, which has abundant high mesoscale eddy activity.

Based on the annual mean surface current (0–100 m), the Kuroshio axes in the different LGM models and the ensemble mean of the Kuroshio axis are shown in Figure 3.3. The LGM-

Kuroshio enters the Okinawa Trough and shows a slight seaward migration in the ECS, which is consistent with the results from all models. This seaward migration can be seen at section PN in 10 models (Figure 3.4), and the maximum current speed of the LGM-Kuroshio increased to 1.4 ± 0.1 m/s (present value is 0.9 m/s). In the ECS, seaward displacement of the Kuroshio axis has been suggested in previous studies (Kubota et al., 2017; Vogt-Vincent & Mitarai, 2020). Moreover, the KC was enhanced offshore and weakened nearshore, in agreement with previous model results (Lee et al., 2013; Vogt-Vincent & Mitarai, 2020). The displacement of the Kuroshio axis in the ECS is attributed to sea-level lowering (Vogt-Vincent & Mitarai, 2020).

In all the models, after the Kuroshio passes through the Tokara Strait, its axis shows no significant differences in the south of Japan. The Kuroshio in the southeast of the Kii Peninsula showed a smaller meander in seven models, a larger meander in two models (CCSM and MIROC4), and no change in MPI4. The ensemble mean of 10 models shows that the LGM-Kuroshio appears to shift northward by 1° in southeastern Honshu.

Under the influence of eddies in the KE region (142.0–145.0° E), the Kuroshio axis meanders significantly southward in the GISS model, displaying a large discrepancy compared to the other nine models. If we look at section 146° E, the LGM-Kuroshio shifts southward by 0.8°–3.1° in 10 models, with an average southward shift of 2.0° relative to the modern position. Previous investigations into planktic foraminifera at a Northwest Pacific site suggested a southward shift of the KE axis during the LGM (Seo et al., 2018), which has also been found in the Central Pacific (Kawahata & Ohshima, 2002). According to the results of MIROC4m in Section 2.4, we found a close relationship between the latitudinal shift of the KE axis and the zero-wind-stress curl position. Here, the ensemble mean of the zero wind-stress curls was located at 41.0 ± 0.8° N, with large deviations for the different LGM models (Figure 3.5). Compared to the present location (41.2° N), the southward shift of the zero wind-stress curl was insignificant. A linkage between the latitudinal shift of the subarctic boundary and tropical

Pacific changes has been suggested by Yamamoto et al. (2005), so the latitudinal shift of the KE axis may also be influenced by other factors (e.g., eddy activities, net air-sea heat flux, and tropical changes).

In the northwest Pacific subtropical gyre, the volume transports in the upper 1000 m in six sections (Figure 2.2a) across the main currents are listed in Table 3.2. The westward volume transport of the NEC as the source of the Kuroshio increased in the 10 LGM models, reaching 52.7 ± 7.1 Sv. Correspondingly, the northward transport of the LGM-Kuroshio at 16.5° N increased to 23.1 ± 6.1 Sv, an increase of 12.1 ± 6.1 Sv compared to the present value (i.e., 11.0 Sv), and the volume transport in eastern Taiwan also increased by 3.9 ± 1.7 Sv. The Kuroshio transport in the ECS during LGM (i.e., at section PN) increased by 0.9–3.3 Sv in 7 models but decreased by 0.2–1.4 Sv in the remaining 3 models, contributing to an average increase of 1.0 Sv, based on the results from all the models. Merging with the Ryukyu Current, the net volume transport of the KC south of Japan (i.e., section ASUKA) increased to 40.3 ± 3.1 Sv. Overall, the results of all 10 models revealed enhanced meridional transport from the tropics to the mid-latitudes in the North Pacific.

According to Equation (3.1) in Section 3.2.2, zonally integrated volume transport from the east coast to 137° E in each model was calculated, and the ensemble mean of 10 LGM models is shown with solid lines in Figure 3.6. During the LGM, the meridional transport was zero at 12.8° N, with southward transport north of 12.8° N and northward transport south of 12.8° N. The zero position shifted southward compared to the present position (i.e., 14.2° N). The ensemble of ten models shows that the meridional transport value from 12.8 to 30.0° N increases by approximately 10 Sv in comparison with the present value, which also reflects the enhanced subtropical gyre.

Large-scale upper ocean circulation is mainly driven by wind stress. The Sverdrup balance relates meridional mass transport (i.e., Sverdrup transport) to the wind-stress curl (Sverdrup, 1947). Using this relation, we calculated the Sverdrup-transport stream function Ψ by integrating the wind-stress curl from the eastern boundary ($\mathrm{x_E}$) at different latitudes (y), as follows:

$$\Psi(\mathrm{x,y}) = -\frac{1}{\rho_0\beta}\int_{\mathrm{x}}^{\mathrm{x_E}} \nabla \times \boldsymbol{\tau}\,\mathrm{dx} + \Psi(\mathrm{x_E, y}), \tag{3.2}$$

where β is the meridional gradient of the Coriolis parameter, ρ_0 is the mean density of seawater (i.e., 1025 kg/m^3), x is the longitude, $\boldsymbol{\tau} = (\tau_x, \tau_y)$ is the wind stress vector, and $\Psi(\mathrm{x_E, y})$ is zero at the east boundary. We used Equation (3.2) to calculate the corresponding wind-driven Sverdrup transport from the east coast to 137° E for 10 LGM models. The ensemble mean values are shown in Figure 3.6 (red dashed line). The obtained ensemble mean values show that wind-driven Sverdrup transport from 14.6 to 31° N was stronger at LGM than at present, suggesting that the subtropical gyre was enhanced at LGM, corresponding to the depth-integrated volume transport, as projected in the model. As Wang et al. (2016) stated, the basin-scale wind stress curl provided dynamic conditions for changes in the Kuroshio transport according to the Sverdrup transport. However, the gyre strength between 31 and 32.5° N was slightly weakened during LGM, whereas that at the north of 32.5° N was the same as the present gyre strength, which was not consistent with wind-driven Sverdrup transport. In addition, it is noticeable that the largest difference in gyre intensity among the LGM models existed between 31° and 33° N. Likewise, the air-sea heat flux in the Northwest Pacific between 30 and 40° N changed dramatically at LGM with a large discrepancy in models (Figure 3.7). According to the suggestion that surface buoyancy fluxes are essential for ocean-gyre transport (Hogg & Gayen, 2020), gyre transport in the region of 30 and 40° N may be significantly influenced by surface buoyancy fluxes.

3.3.2 Ensemble of the North Equatorial Current

Based on the definition of the NEC bifurcation latitude in Section 3.2, the NEC bifurcation latitudes at the surface and 500 m and their latitudinal shift relative to the present locations are shown in Table 3.3. During the LGM, the latitude of the NEC bifurcation moved toward the north with increasing depth, reaching 12.1–13.9° N at the surface and 13.5–15.2° N at 500 m, with an average of 12.6 ± 0.5° N and 14.7 ± 0.5° N, respectively. Compared to the current position at the surface (13.3° N), the bifurcation latitude shifted southward by 0.3–1.1° in nine models and shifts northward by 0.6° in CNRM, yielding an average southward displacement of 0.7° during the LGM. Regarding the bifurcation latitude at 500 m (17.3° N), a southward displacement appeared consistently in 10 models, with an average shift of 2.5°. The magnitude of the northward shift from the sea surface to a depth of 500 m decreased during the LGM, reflecting the same result as that obtained in the previous chapter.

For MIROC4m, we found that the latitudinal shift of NEC bifurcation from 35 to 0 ka BP is associated with the shift of the zero wind-stress curl line integrated from east to west, which is in agreement with the Sverdrup theory. As Table 3.3 shows, the ensemble mean of the zero wind-stress curl in 10 LGM models showed a southward shift of 0.5°, corresponding to the southward movement of NEC bifurcation at the surface and 500 m. The latitudinal shift of the NEC bifurcation at the surface and the zero wind-stress line were consistent in the six LGM models but not in CNRM, MPI, and AWI4. Although the NEC bifurcation at 500 m shifted southward in all LGM models, the zero wind stress lines shifted northward in MPI and AWI4. Furthermore, the location of the zero wind-stress line in MPI4 was the same as that at 0 ka BP, and the NEC bifurcation latitude showed a southward shift from the surface to a depth of 500 m. Therefore, the latitudinal shift of the NEC bifurcation in different LGM models was not entirely determined by the location of the zero wind-stress curl.

We calculated the wind stress curl ratio (r_{curl}) and bifurcation latitude slope (s) according to the definitions in Section 3.4.2; the values are listed in Table 3.3. Compared with the present value of r_{curl} (i.e., 2.24) and s (i.e., 8.0 $x10^{-3}$ °/m), the ensemble mean of 10 LGM models shows that r_{curl} and s reduced to 1.97 and 4.3 $x10^{-3}$ °/m, respectively. This result agrees with the demonstration that a weaker poleward shift of the NEC bifurcation latitude with increasing depth is determined by the smaller intensity differences between the subtropical and tropical gyres (Guo et al., 2019). However, if we compare each LGM model to the respective 0 ka BP model, the r_{curl} and s values in 9 models decreased by 1.77–2.18 and 1.5 $x10^{-3}$ °/m –5.4 $x10^{-3}$ °/m, respectively, with the reversal of r_{curl} and s changes, increasing by 0.05 and decreasing by 3.1 $x10^{-3}$ °/m, respectively, in CCSM. We conclude that no significant positive correlation existed between r_{curl} and s values in the 10 LGM models. A pure wind-driven model without buoyancy forcing was considered incomplete and could not be used to explain the poleward shift of NEC bifurcation in a previous study by Guo et al. (2019).

3.3.3 Ensemble of the sea surface temperatures and model evaluation

The annual mean SST obtained from the 10-model ensemble mean and spatial distribution in LGM cooling are shown in Figure 3.8a and 3.8b. In our study, the ensemble mean of SST from 10 models indicated a cooling of 1.9 ± 0.5°C during LGM in the 15° S–15° N latitude band, comparable to 2.5 ± 0.1°C from reconstructed SSTs (Monteagudo et al., 2021), but slightly larger than 1.2 ± 1.1°C suggested by MARGO (Waelbroeck et al., 2009). In the central equatorial Pacific, there was a slight cooling in the SST, about 1°C. Our result is consistent with that of MARGO which suggests little SST change in most of the central Pacific; however, disagrees with the previous result that foraminifera-based SSTs in the glacial central equatorial Pacific showed ~2°C cooling (Monteagudo et al., 2021). For the western and eastern equatorial Pacific, the distribution of Mg/Ca-base temperatures suggested a stronger LGM cooling in the western warm pool region (~2.7°) than in the eastern cold tongue region (~1.6°C) (Ford et al., 2015). Likewise, the ensemble mean of our model results showed LGM cooling of 2.2 ± 2.4°C, 1.9 ± 0.5°C in the western warm pool region and in the eastern cold tongue region, respectively. In contrast, a recent multi-proxy data assimilation study showed enhanced cooling during the LGM in the eastern equatorial Pacific (Tierney et al., 2020).

In Figure 3.8, the areas where ΔSSTs exceed -6° are located in the Japan Sea and the Kuroshio–Oyashio confluence region at 40° N, which resembles the spatial patterns of the assimilated ΔSST field shown by Tierney et al. (2020). The strong LGM cooling near 40° N in the Pacific is considered to be related to the southward shift in the subpolar gyre (Tierney et al., 2020), and our models showed a southward shift (~2.0°) in the KE during the LGM.

If we look at the Kuroshio region, our modeled ΔSST in the Pacific Ocean east of the Ryukyu Islands was approximately -2°C during the LGM, similar in magnitude to other recent model results (Tierney et al., 2020; Vogt-Vincent & Mitarai, 2020). In the ECS, a significant cooling exceeding 5°C occurred on the nearshore side along the KC axis and a cooling of 1–2°C on the offshore side. Vogt-Vincent and Mitarai (2020) suggested that the temperature drop in the ECS except in the northern Okinawa Trough was dominated by climatic signals. Based on different SST proxies in the Okinawa Trough, R. A. Kim et al. (2015) suggested that SSTs during the LGM were 3°C lower than their current values under the influence of the Kuroshio. In our models, the SST in the northern Okinawa Trough decreased by 4–5°C during the LGM, as the Kuroshio inflow was suppressed by the closure of the Tsushima Strait. Moreover, in the southern Okinawa Trough, the LGM SST cooling was relatively small, with a value of 1–2°C. A similar distribution of ΔSST at the LGM has also been shown in previous model results (Vogt-Vincent & Mitarai, 2020). Besides, another assimilated model by Tierney et al. (2020) was configured with a much lower resolution, so it only showed the SST cooling at the LGM with a higher value (~2.5°C) in the southern Okinawa Trough.

We show the corresponding spatial distribution of the standard deviation for the ensemble mean of ΔSSTs in Figure 3.8c. Considering that low values indicate little spread around the mean ΔSSTs and robust results, the ΔSSTs with low standard deviations (smaller than 0.5°C) in the western equatorial Pacific region were well consistent in the 10 LGM models. In the subtropical region and central equatorial Pacific, the standard deviation of ΔSST was 0.5–1°C and 1°C respectively. The standard deviation of ΔSST was elevated (2–2.5°C) in the Kuroshio–Oyashio confluence region, resulting from high eddy activity (Figure 3.2). Across all models, the largest spread of ΔSST occurred in the Japan Sea, and many of the models showed a widespread cool or warm anomaly relative to the ensemble mean (i.e., CNRM, GISS, MIROC, MRI, and AWI4 in Figure 3.9). Likewise, as shown in Figure 3.8d, SST cooling in the western Japan Sea was shown to occur in 8 out of 10 models, except for CNRM and MRI. Overall, a large discrepancy was observed among the models in the region north of 30° N.

A previous comparison between proxy SST estimates suggested that alkenone unsaturation ($\mathrm{U}_{37}^{\mathrm{K}'}$) and Ma/Ca ratio seemed to be more reliable in the Okinawa Trough (R. A. Kim et al., 2015). Therefore, we used the SSTs reconstructed from $\mathrm{U}_{37}^{\mathrm{K}'}$, oxygen isotopes, and the Mg/Ca ratio for model evaluation with available SST values at the core top, Late Holocene (3–0 ka BP), and LGM periods. Our analysis focused on the Kuroshio region, including the NEC (0–38° N, 100°–180° E).

For the above three proxies, we collected 32, 13, and 26 core sites and compared the proxy-based SSTs at 0 ka BP (i.e., core top or Late Holocene) with modeled SSTs at 0 ka BP interpolated to corresponding locations. All the reconstructed and modeled SSTs were correlated at the 99% confidence level with a correlation coefficient $r = 0.86$, corresponding to 0.92 for the annual mean SSTs (i.e., $\mathrm{U}_{37}^{\mathrm{K}'}$-based and oxygen isotope-based) and 0.53 for the summer mean SSTs (i.e., Mg/Ca-based). The Taylor diagram (Taylor, 2001) was used to investigate the ability of the 10 LGM models to simulate ΔSST (ΔSST = SST_{LGM}-SST_{0ka}) in the Kuroshio region by comparing the observed and simulated annual mean values and summer mean values, respectively (Figure 3.10).

According to the values in Table 3.4, the GISS and CNRM results are closest to the observed annual ΔSSTs, with correlation coefficients of 0.51 and 0.40 at the 99% confidence level. In the comparison of the summer ΔSST, the GISS simulation had the strongest correlations significant at the 99% confidence level with r = 0.50. Concerning both the annual and summer ΔSST simulations, the correlations in MIROC4m, MIROC, and GISS were statistically significant above the 95% confidence level. However, MRI, AWI4, and MPI4 showed poor performance in simulating ΔSSTs, with a confidence level lower than 95 %. The annual mean ΔSST correlation in CNRM reached a confidence level of more than 95 %, but the summer value was below 90%. In contrast, MIROC4 and CCSM had better summer ΔSST correlations than annual means.

In the 10 models, except for MIROC4, the standard deviation of the annual mean ΔSST was less than one (Figure 3.10), indicating a lower variation than that observed in the Kuroshio Region. Four models (CNRM, MIROC, MRI, and MIROC4) showed larger variations in mean summer ΔSST with standard deviations greater than 1, as well as greater normalized centered root-mean-square differences. It can be noted that MIROC4 exhibited the largest variation and a large normalized centered root-mean-square difference (RMSD) in the ΔSST simulation. Above all, GISS performed best for the ΔSST simulation, while MIROC4 displayed the largest difference from the observations.

Considering that the significance of the correlation coefficient depends on the sample size, a simple evaluation of LGM models based on the limited numbers of observed ΔSSTs in the mid-and low-latitude Northwest Pacific is insufficient. More reliable observations are required to validate the model further. In addition, the quality of the projected SSTs in our model depended strongly on the quality of the climatic boundary conditions and background temperatures. Hence, improving the accuracy of the climate models is of vital importance in simulating regional ocean models.

3.4 Summary

Based on the results of MIROC4m and other nine PMIP3/4 models at the LGM, the ensemble mean of the Kuroshio axis suggests a slight seaward displacement in the ECS, a northward shift of 1° in southeast Honshu, and an average southward shift of 2.0° at section 146° E in the KE region.

A comparison of the depth-integrated and wind-driven Sverdrup transports revealed that the North Pacific subtropical gyre was enhanced during the LGM, dominated by the wind stress curl in the 14.6 to 31° N region.

The NEC bifurcation latitude at the LGM shifted southward by 0.7° and 2.5° at the surface and 500 m, respectively, for the 10 LGM model ensemble mean. However, the latitudinal shift of the NEC bifurcation did not completely correspond to the location of the zero wind-stress curl in the different models.

The ΔSSTs reconstructed from $U_{37}^{K'}$, oxygen isotopes and the Mg/Ca ratio in the Kuroshio region were used for model evaluation. We found that GISS-E2-R in PMIP3 performed best for the ΔSST simulation, and MIROC-ES2L in PMIP4 displayed the largest difference from the observations.

Figures

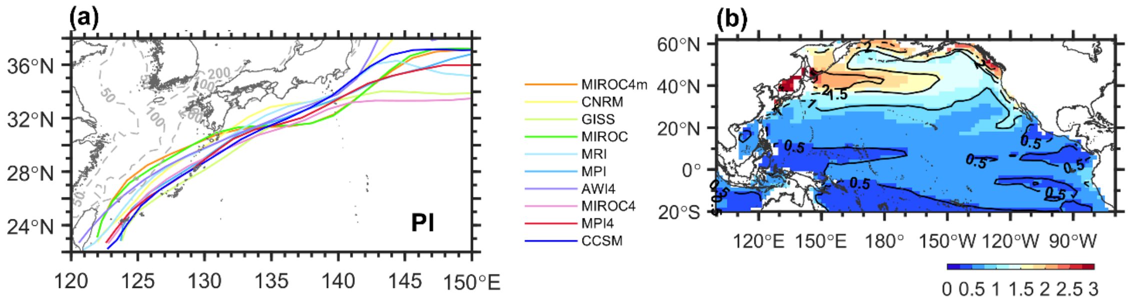

Figure 3.1 (a) Kuroshio axes obtained from original PI experiments in ten climate models. (b) The standard deviation of the original ∆ SST (unit: °C, $\Delta T = SST_{LGM} - SubST_{PI}$) during the LGM.

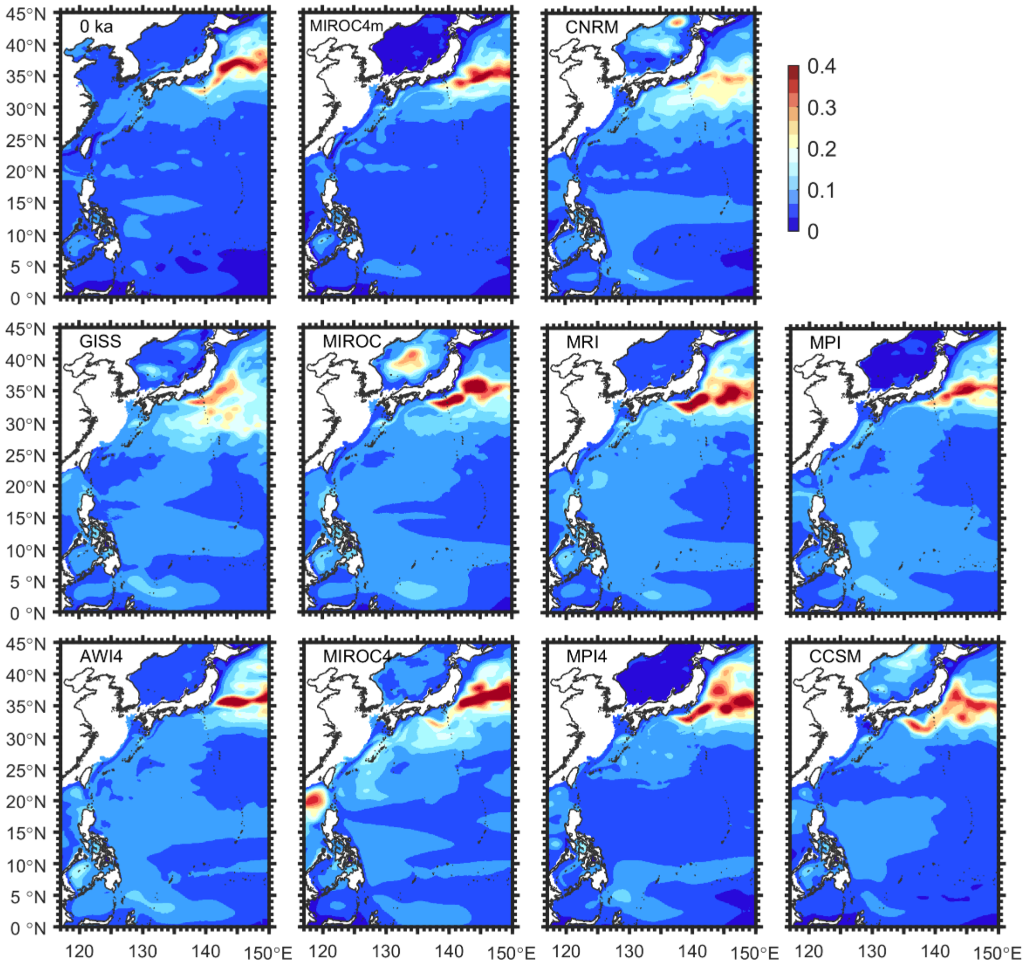

Figure 3.2 The root mean square of SSH (unit: m) in the Kuroshio region for different LGM models.

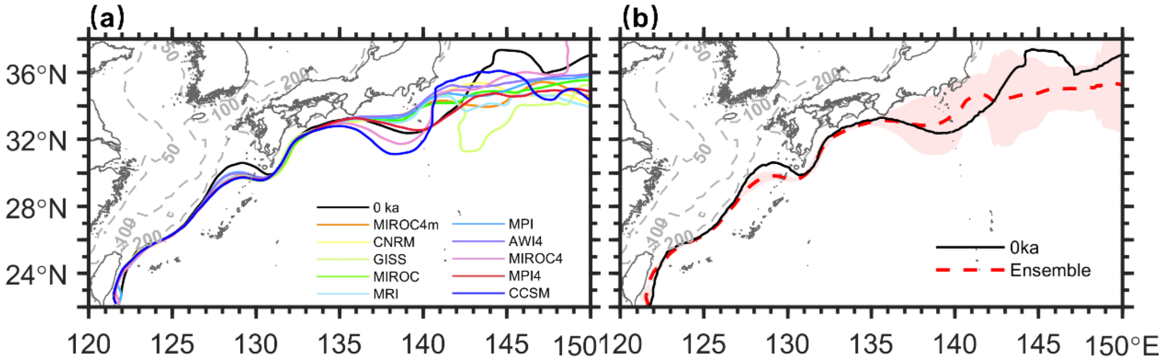

Figure 3.3 Kuroshio axes at 0 ka BP, (a) different LGM models, and (b) ensemble mean of models. Gray dotted lines indicate the East China Sea depths. Pink shading indicates the 95% confidence level of the Kuroshio axis at LGM.

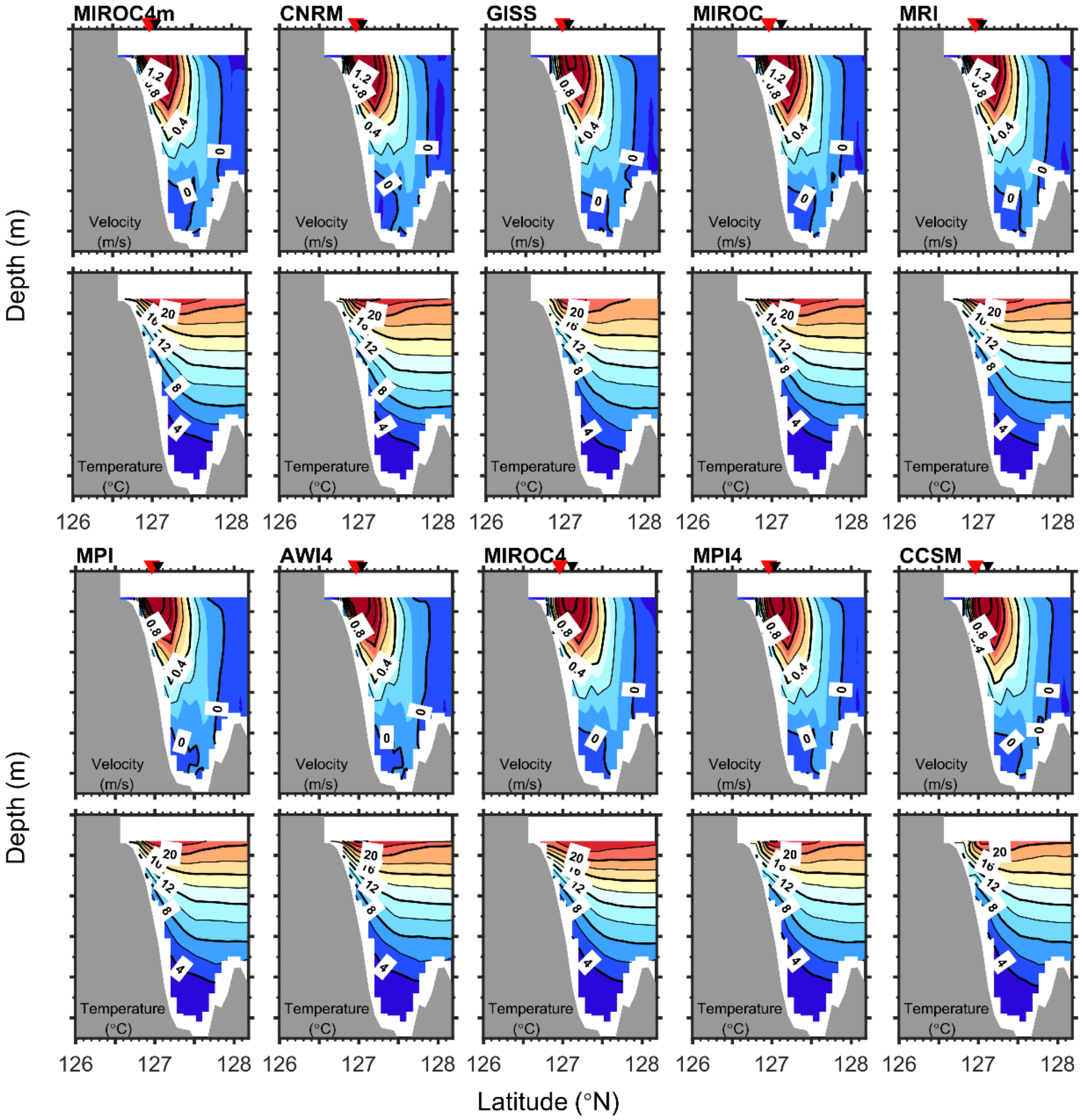

Figure 3.4 Vertical distributions of modeled velocity and potential temperature for the PN line during the LGM. Black contours in the upper panels indicate the current speed with a 0.2 m/s interval, and those in the lower panels indicate the potential temperature with a 2°C interval. Inverted triangles indicate the locations of maximum current speeds at 0 ka BP (red) and LGM (black).

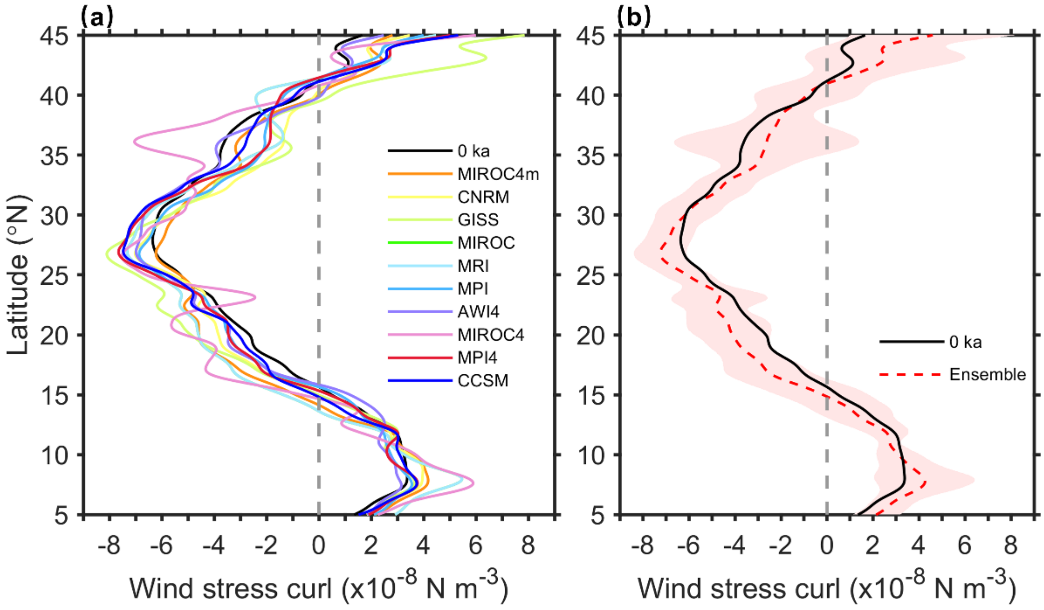

Figure 3.5 Zonal mean wind-stress curls in the North Pacific (i.e., 100° E–80° W) at 0 ka BP, (a) each LGM model, and (b) ensemble mean of models. Pink shading indicates the 95% confidence level of the Kuroshio wind-stress curl at LGM.

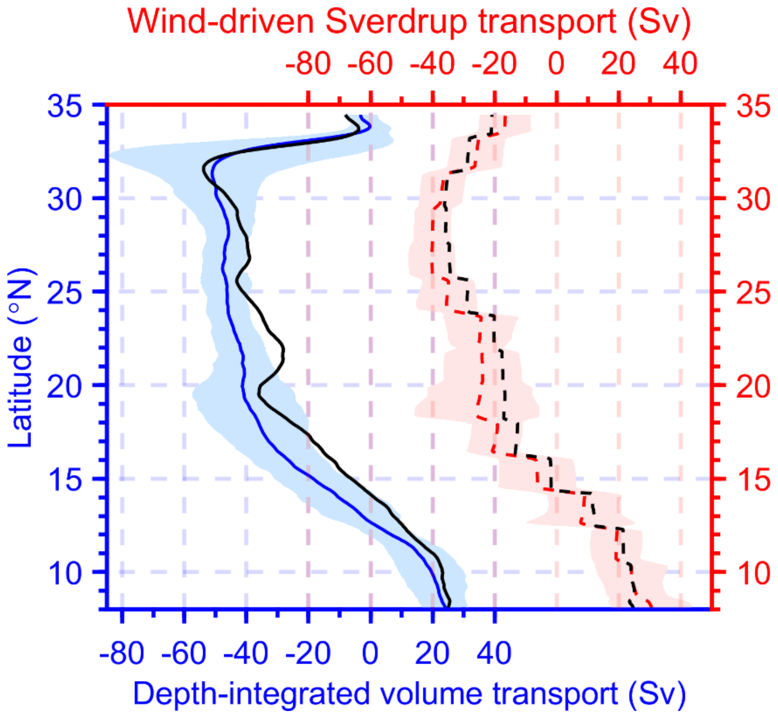

Figure 3.6 Ensemble mean of zonally integrated values in Sv from the east coast to 137 °E of modeled volume transport in the upper 1000 m (solid lines, with reference to the blue axes) and wind-driven Sverdrup transport from the east coast to 137 °E (dashed lines, with reference to the red axes), blue and red lines indicate the ensemble of ten LGM models and black lines indicate values at 0 ka BP. All the values are processed with 0.25 degree running average. Blue shading and pink shading indicate the 95% confidence level of the volume transports at LGM.

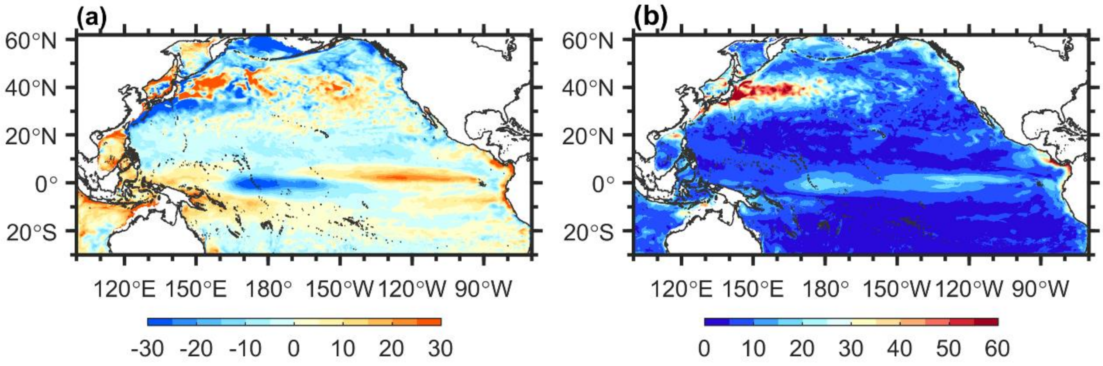

Figure 3.7 (a) Multi-model ensemble of changes in the air-sea heat flux (unit: W/m^2) relative to 0 ka BP, and (b) standard deviation of changes in the air-sea heat flux (unit: W/m^2).

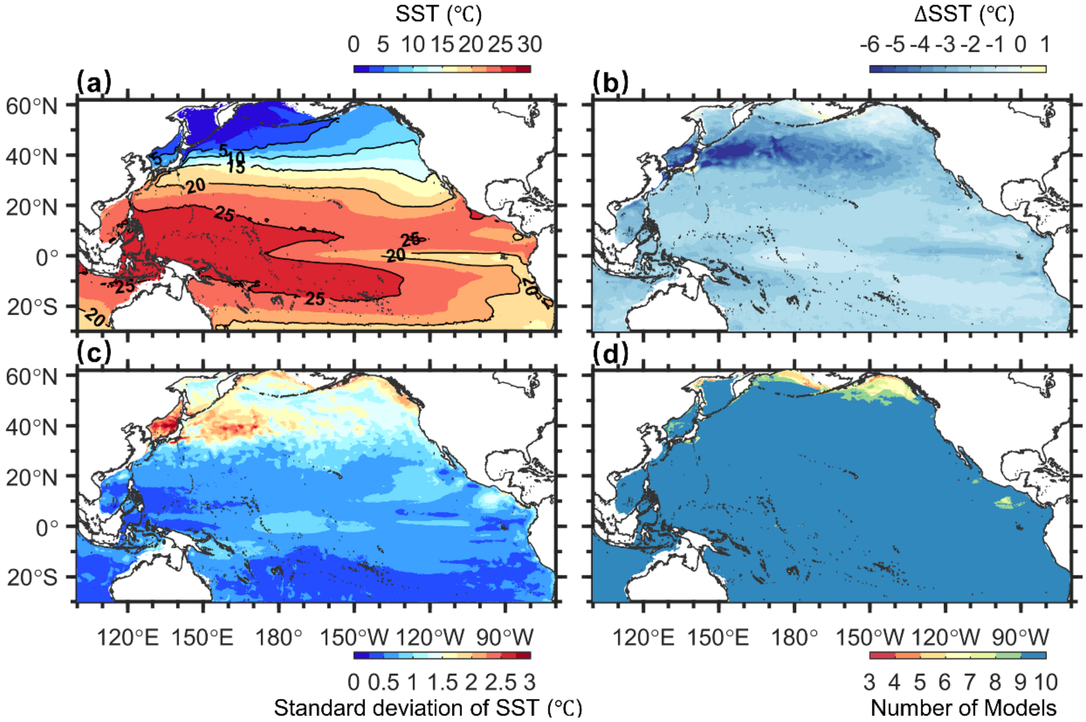

Figure 3.8 (a) Multi-model ensemble of SST (unit: °C) calculated from 10 models during the LGM. (b) Multi-model ensemble means of ΔSSTs (unit: °C) compared to the present day. (c) The standard deviation of the SST (unit: °C). Low values indicate little spread around the mean value and robust results. (d) The number of models in the ensemble showing agreement on the sign of the change.

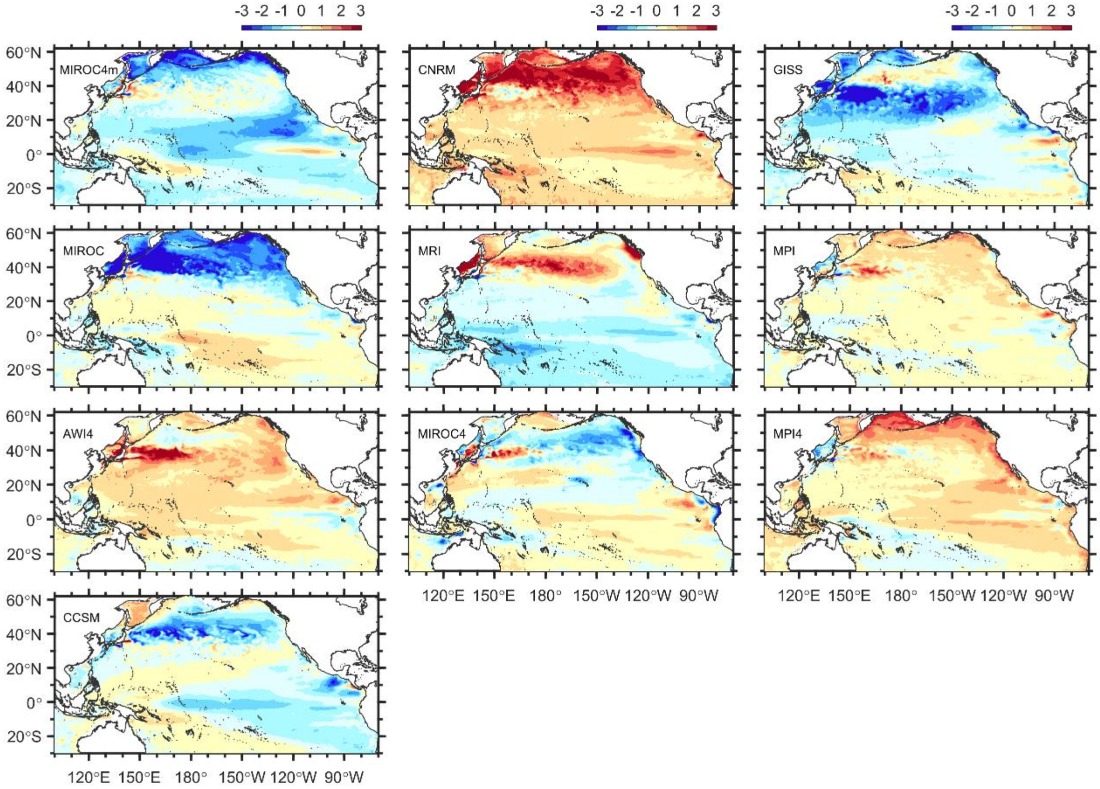

Figure 3.9 Anomaly of annual mean ΔSSTs (unit: °C) for each LGM model, relative to the ensemble mean.

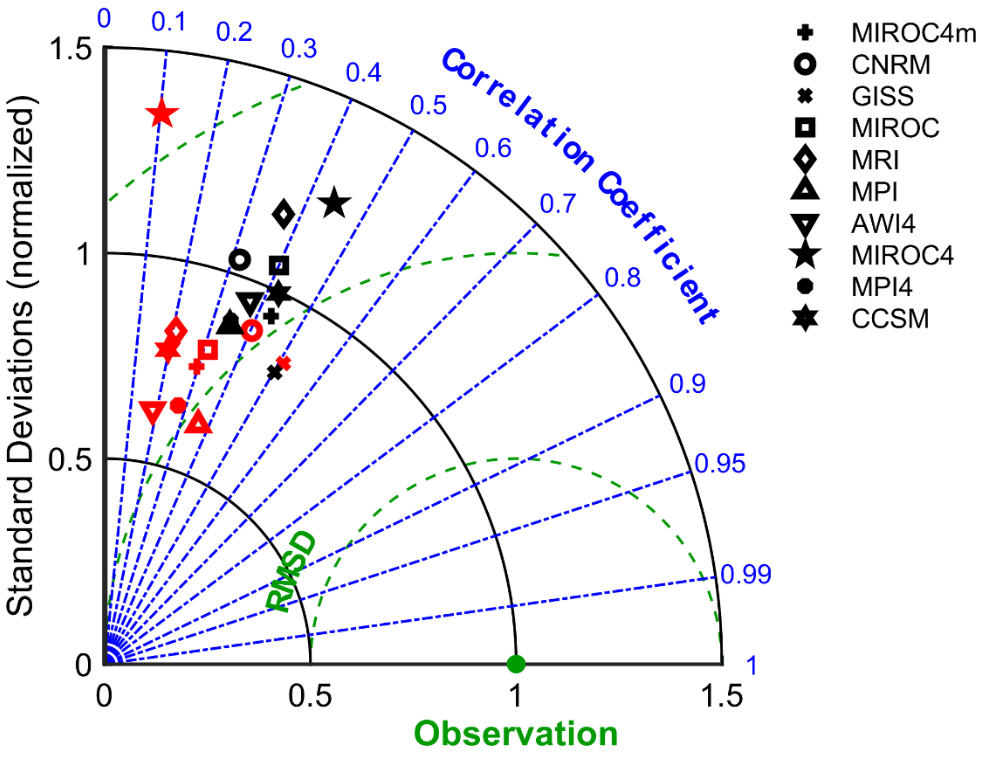

Figure 3.10 Taylor diagram for the normalized pattern statistics of annual mean ΔSSTs (red) and summer ΔSSTs (black) in the region (0°–38° N, 100°–180° E) between the ten LGM models and the reconstructed ΔSSTs in previous observations. Symbols represent different LGM models. The radial distance from the origin shows the normalized standard deviation by the observed data (marked as Observation). The azimuth position gives the correlation coefficient between the model simulation and the observed ΔSSTs, and the normalized centered root-mean-square difference (RMSD) between a model and the observation is proportional to their distance.

Tables

Table 3.1 Basic information on PMIP3/4 models used in this study. Here tauu, tauv, thetao, so, tos, sos, rsds, rsus, rlds, rlus, hfls, and hfss refer to surface northward wind stress, surface eastward wind stress, sea water potential temperature, sea water salinity, sea surface temperature, sea surface salinity, surface downwelling shortwave radiation, surface upwelling shortwave radiation, surface downwelling longwave radiation, surface upwelling longwave radiation, surface latent heat flux, and surface sensible heat flux respectively.

	Model-id	**Country**	**Resolution**		**Reference**	**Variables used in models**
			Atmosphere	**Ocean**		
PMIP3	CNRM-CM5 (CNRM)	France	~1.4°*1.4°*L31	1°*~0.33–1°*L42	Voldoire et al. (2013)	tauu, tauv, thetao, so, tos, sos, rsds, rsus, rlds, rlus, hfls, hfss
	GISS-E2-R (GISS)	USA	2.5°*2°*L40	1.25°*1°*L32	Schmidt et al. (2006)	
	MIROC-ESM (MIROC)	Japan	~2.8°*2.8°*L80	~0.9°*1.4°*L44	Watanabe et al. (2011)	
	MRI-CGCM3 (MRI)	Japan	1.125°*1.1°*L48	1°*0.5°*L51	Yukimoto et al. (2012)	
	CCSM4 (CCSM)	USA	1.25°*~0.9°*L26	1.11°*~0.27–0.54°*L60	Gent et al. (2011)	
	MPI-ESM-P (MPI)	Germany	1.875°*~1.9°*L47	~1.5°*0.1–1.6°*L40	Raddatz et al. (2007)	
PMIP4	AWI-ESM (AWI4)	Germany	1.875°*~1.9°*L47	~0.2–1°*0.2–1°*L46	Shi et al. (2020)	
	MIROC-ES2L (MIROC4)	Japan	~2.8°*2.8*L40	~0.7°*1°*L63	Ohgaito et al. (2021)	
	MPI-ESM1-2 (MPI4)	Germany	1.875°*~2°*L47	~1.5°*0.1–1.6°*L40	Mauritsen & Roeckner (2020)	

Table 3.2 Annual mean volume transports (in Sv) in the upper 1000 m across the sections in thr ten LGM models, ensemble mean of the volume transports and standard deviation (STD).

	Volume transport (Sv)					
	S1 NEC	S3 KC at 16.5° N	S4 East Taiwan	S5 PN	S6 Tokara Strait	S7 ASUKA
0 ka	-38.5	10.96	25.06	23.6	22.8	31.6
MIROC4m	-54.9	24.4	29.2	24.7	24.1	39.2
CNRM	-50.4	24.1	30.1	25.4	24.8	33.8
GISS	-54.5	33.9	26.5	22.8	21.1	37.2
MIROC	-59.0	26.9	30.4	26.9	25.6	44.6
MRI	-56.2	23.2	32.0	26.2	24.8	42.0
MPI	-46.2	16.7	27.1	22.2	21.3	39.8
AWI4	-40.6	15.6	28.0	23.4	22.5	41.4
MIROC4	-64.2	29.1	30.1	25.1	23.7	40.0
MPI4	-45.2	14.8	28.9	24.5	23.6	43.6
CCSM	-55.5	22.7	28.2	25.2	23.8	41.8
Ensemble mean	-52.7	23.1	29.0	24.6	23.5	40.3
STD	7.1	6.1	1.7	1.5	1.5	3.1

Table 3.3 The NEC bifurcation latitude (NBL) and its latitudinal shift in in ten LGM models, negative values indicate southward migration. The wind stress curl intensity ratio (r_{curl}) and the bifurcation slope(s).

	NBL (° N)		Shift of NBL (°)		r_{curl}	s ($x10^{-3}$°/m)	Zero wind-stress curl (° N)	Shift of zero wind-stress curl (°)
	0 m	500 m	0 m	500 m				
0 ka	13.3	17.3			2.24	8.0	15.2	
MIROC4m	12.4	14.4	-0.9	-2.9	1.95	4.0	13.9	-1.2
CNRM	13.9	15.2	0.6	-2.1	1.79	2.6	15.1	-0.1
GISS	12.8	13.5	-0.4	-3.7	2.18	1.5	14.8	-0.4
MIROC	12.4	14.1	-0.9	-3.2	1.80	3.5	13.7	-1.5
MRI	12.1	14.7	-1.1	-2.6	1.80	5.1	13.7	-1.5
MPI	12.4	14.9	-0.9	-2.4	1.94	5.0	15.3	0.1
AWI4	12.3	15.0	-0.9	-2.2	1.94	5.4	15.6	0.4
MIROC4	13.0	14.1	-0.3	-3.2	1.77	2.2	14.5	-0.7
MPI4	12.7	15.1	-0.5	-2.2	1.98	4.8	15.2	0.0
CCSM	12.6	15.0	-0.7	-2.3	2.29	4.9	14.6	-0.6
Ensemble mean	12.6	14.7	-0.7	-2.5	1.97	4.3	14.6	-0.5

Table 3.4 Correlation coefficients and confidence levels between observed and simulated ΔSSTs for each LGM model.

	Correlation coefficients (annual ΔSST)	Confidence level (%)	Correlation coefficients (summer ΔSST)	Confidence level (%)
MIROC4m	0.29	95	0.43	95
CNRM	0.40	99	0.32	< 90
GISS	0.51	99	0.50	99
MIROC	0.31	95	0.40	95
MRI	0.21	< 90	0.37	90
MPI	0.36	95	0.35	90
AWI4	0.18	< 90	0.37	90
MIROC4	0.10	< 90	0.45	95
MPI4	0.27	90	0.34	90
CCSM	0.20	< 90	0.42	95

Chapter 4: Kuroshio and North Equatorial Current

4.1 Introduction

As the origin of the Kuroshio, the NEC bifurcates along the Philippine coast to form the KC and MC, and the flow distribution of the NEC is determined by the meridional movement of the NEC bifurcation latitude (Y. Y. Kim et al., 2004; Qiu & Chen, 2010). The interannual variability of NEC bifurcation latitude is suggested to be related to variations in NEC and KC transport (Y. Y. Kim et al., 2004). As a result, NEC bifurcation plays a vital role in the heat and water mass exchanges between subtropical and tropical circulation in the North Pacific (Lukas et al., 1991; Qiu & Chen, 2010).

In the modern ocean, based on the previously observed temperature and salinity data, Qu and Lukas (2003) showed that the bifurcation latitude of the NEC shifted northward from 13.3° N near the surface to 20° N at a depth of 1000 m. This northward shift with increasing depth has also been shown in previous model simulations (Guo et al., 2019; Y. Y. Kim et al., 2004; J. Li & Gan, 2022).

Millennial-scale changes in NEC bifurcation remains unclear. Dang et al. (2012) reconstructed thermocline water temperatures using planktonic foraminiferal Mg/Ca from sediments of the western tropical Philippines and attempted to infer the movement of the NEC bifurcation by studying the variability in thermocline water temperatures, but the timeline from the foraminiferal data only spanned 13–0 ka BP. Based on the reanalyzed salinity data, the thermocline salinity in the Sulu Sea also reflects the movement of the NEC bifurcation, and Weiss et al. (2021) used the reconstructed thermocline salinity from the Sulu Sea sediment core to show the millennial-scale meridional migration of the NEC bifurcation from 20 to 5 ka BP. Nevertheless, due to the temporal and spatial restrictions of the observational data, the NEC bifurcation from the glacial period to the present remains unclear.

In the last few decades, there has been a surge of interest in the variations in the Kuroshio during the past 40,000 years. One major issue is the paleo-KC pathway in the Okinawa Trough and KE region. The KC was thought to have been deflected eastward into the Pacific due to the land bridge between the Ryukyu Arc and Taiwan at the LGM, reentering the Okinawa Trough in the Early Holocene (Ahagon et al., 1993; Ujiie et al., 1991; Ujiié & Ujiié, 1999; Ujiié et al., 2003). However, many proxies inside the Okinawa Trough, such as planktonic foraminiferal assemblages, oxygen isotopes, sea surface temperature, and sediment characteristics, indicate the inflow of the KC into the ECS during the last glacial period (Amano & Itaki, 2016; Ijiri et al., 2005; Kawahata & Ohshima, 2004; Kim et al., 2015; Li et al., 2018; Xu & Oda, 1999). In addition, the paleo-KC intensity in the Okinawa Trough has attracted substantial attention. It has been suggested that KC intrusion into the Okinawa Trough was reduced during the LGM and the early deglaciation (Ijiri et al., 2005; Li et al., 2018a; Ujiié et al., 2016; Xiang et al., 2007). However, based on the temperature and nutrient conditions, it is possible that the Kuroshio transport during the LGM became stronger (Kubota et al., 2017). Thus far, it remains unclear whether the paleo-KC was stronger or weaker in the Okinawa Trough.

The KE is located on the northern boundary of the North Pacific subtropical gyre. Early studies of planktic foraminiferal assemblages reported that the boundary region of the subtropical-subarctic gyre shifted southward during the last glacial period (Thompson, 1981; Thompson & Shackleton, 1980), and the southward shift of the subarctic boundary was confirmed by the SST gradient in the latitudinal direction (Harada et al., 2004; Seo et al., 2018). The KE was also thought to migrate southward during global glacial climate change (Gallagher et al., 2015; Kawahata & Ohshima, 2002; Yamamoto, 2009). However, Sawada and Handa (1998) suggested northward Kuroshio migrations off the coast of Central Japan from 26 to 24.5 and 21 to 19 ka BP. Though the paleo-KC path and intensity have been investigated and debated, observations have very limited spatial and temporal scales. Therefore, it is difficult to study the Kuroshio evolution during the last glacial period.

The analysis of the LGM results in Chapter 3 show that the changes in the Kuroshio path, Kuroshio intensity, and SST were very close to those of the ensemble mean of the 10 models. Considering that the changes in the Kuroshio system (i.e., KC, KE, and NEC) from the last glacial period to the present day are still poorly understood, we simulated how the Kuroshio system responded to the combined changes during five ages- 0 (i.e., present), 6, 21 (i.e., LGM), 30 and 35 ka BP, using the MIROC4m data.

Section 4.2 describes the calculation of the upper 1000 m of the integrated volume transport stream function. Section 4.3 shows the changes in the Kuroshio (i.e., path, surface current, and strength), the vertical and latitudinal changes in NEC bifurcation latitude, and distributions of the changes in the SSTs. Section 4.4 addresses the changes in the Kuroshio and NEC bifurcation latitude and confirms whether the vertical temperature gradient is a reliable indicator of KC intensity with the modeled water temperatures. Finally, a summary is presented in Section 4.5.

4.2 Data and methods

The meteorological and oceanic data used for the four paleo-experiments (6 ka BP, LGM, 30 ka BP, and 35 ka BP) were provided by the fully coupled atmosphere–ocean general circulation model named MIROC4m (Chan et al., 2011). Based on the equations in Section 2.2.1, the climatological monthly mean meteorological and oceanic data provided by MIROC4m and the net air-sea heat flux (Q_{net}) for each age were obtained.

Regarding MIROC4m, the atmospheric model was employed with 2.8° horizontal resolution and 20 sigma levels, whereas the ocean model had approximately 1.4° horizontal resolution and 43 vertical levels (Chan et al., 2011). The time slice results of MIROC4m were derived from experiments with modern-day land sea mask and ice sheets for PI and 6 ka BP periods and land sea mask and ice sheets for LGM, 30 and 35 ka BP periods. Greenhouse gas levels and orbital parameters were mostly set to their respective values at those times. Some of these experiments have been used as part of other studies, such as those exploring the mid-Holocene (Ohgaito et al., 2013; O'ishi & Abe-Ouchi, 2011) and the LGM (Kageyama et al., 2013; Sherriff-Tadano et al., 2018). For this study, climatological values were calculated from each time slice experiment.

To remove the bias between NCEP/NCAR (standard 0 ka BP) and MIROC4m, we modified the MIROC4m variables using the following equation:

$$\mathrm{F}(\mathrm{x},\mathrm{y}) = \mathrm{F}_{\mathrm{o}}(\mathrm{x},\mathrm{y}) - \Delta\mathrm{F}(\mathrm{x},\mathrm{y}),$$

where $\mathrm{F}(\mathrm{x},\mathrm{y})$ and $\mathrm{F}_{\mathrm{o}}(\mathrm{x},\mathrm{y})$ denote the modified and original monthly averaged variables of MIROC4m, respectively, and $\Delta\mathrm{F}(\mathrm{x},\mathrm{y})$ is the bias for the same variable between PI in MIROC4m and standard 0 ka BP (NCEP/NCAR). The correction was applied to the net air-sea heat flux and eastward and northward wind-stress components.

We compared the air-sea heat flux differences between the paleo-ages and 0 ka BP (Figure 4.1) and determined the zero wind-stress curl positions (Figure 4.2). During the glacial ages (LGM, 30 and 35 ka BP), the ocean lost more heat (>20 W/m^2) to the atmosphere in the Kuroshio region, whose cooling effect has been indicated by variations in subtropical SSTs (Sagawa et al., 2011). Meanwhile, the westerly jet stream shifted southward by ~1.0° in the North Pacific.

The model settings are described in section 2.2.2. Based on the global mean sea level given by Yokoyama et al. (2018, 2019) for the past 35 ka, the reductions in water depth due to the lowering of sea level in four experiments from 35 ka to 6 ka were determined (Table 4.1).

During the LGM, the Tsushima Strait was closed, and the Japan Sea became a semi-closed sea with the Tsugaru Strait open (Figure 4.3).

Each model was forced from an initial no-motion condition with a monthly climatological temperature and salinity (Table 4.1). In addition, the model was forced by the climatological monthly heat flux and wind stresses, and was subsequently integrated for 30 years. The final 5-year results were used in the analysis.

4.3 Results

4.3.1 Kuroshio path, surface velocity, and transport

Figure 4.4 shows the annual mean surface current (0-100 m) in KC and KE regions at five ages. The Kuroshio axis is defined by the maximum velocity along the Kuroshio (Ambe et al., 2004). Based on the annual mean surface velocity, we present the Kuroshio axes for the five ages in Figure 4.5, in which the positions of the seven sections across the Kuroshio are also given. Compared to the modern Kuroshio at 0 ka BP, the paleo-Kuroshio at 6 ka BP shows almost the same position east of Taiwan along the shelf slope of ECS and south of Japan. However, the Kuroshio in the other glacial ages showed a slightly different path from that of the modern one. For example, the paleo-Kuroshio axes east of Taiwan shift shoreward compared to the modern Kuroshio (Figure 4.6a). Under the influence of the climate and coastline shift, the location of the Kuroshio axis at section PN had no migration at 35 ka BP but shifted seaward at the LGM and 30 ka BP (Figure 4.7a). The paleo-Kuroshio in the glacial age tends to shift seaward in the Tokara Strait (Figure 4.6b), and this seaward displacement of the Kuroshio axis during the LGM was also found in the previous model results (Vogt-Vincent & Mitarai, 2020). In addition, the seaward shift distance is likely proportional to the lowered sea level because the KC axis exhibits the southernmost displacement during the LGM, when the sea level is the lowest.

The Kuroshio path south of Japan (i.e., 131.0–136.5° E) was very similar among the five cases (Figure 4.5), especially in the region south of Shikoku (i.e., the ASUKA section; Figure 4.8). However, the glacial KC axes southeast of Japan (i.e., 136.5–142.0° E) migrated northward (Figure 4.9) and present the largest migration of ~1.5° at 140° E. The KE migrated northward at 142° E at 6 ka BP, LGM, and 35 ka BP (Figure 4.10), and southward at 146° E (Figure 4.7b) for 1.0 and 2.0° ranges during 6 ka BP and glacial ages, respectively. In the KE region (i.e., 142–150° E). By comparison, the southward migration of the glacial KE axes ranged from 0.5 to 3.5° at different longitudes. Compared to the latitudinal KE amplitude at 0 ka BP, the paleo-KE axes meandered with smaller amplitudes, and the smallest meandering amplitude occurred at 35 ka BP.

In the area east of Taiwan, little difference was observed in the Kuroshio surface velocity between 6 and 0 ka BP, both of which had a maximum value of 0.93 m/s. The glacial Kuroshio surface velocity was stronger with shoreward movement of its maximum core (Figure 4.6a), with values 1.47, 1.44, and 1.40 m/s in LGM, 30 ka BP, and 35 ka BP, respectively. In the central ECS (section PN in Figure 4.7a), the Kuroshio surface current also show two regimes: a weak one (~0.9 m/s) in 0 ka and 6 ka and a strong one in glacial ages (~1.4 m/s), although their position changes little. Constrained by the thermal wind relation, the horizontal gradient of water temperature, or isotherm slope, increased with the intensification of the surface current during the glacial period (Figure 4.7a). At the exit point of Kuroshio from the Tokara Strait in ECS, its surface current was weaker than that in section PN. However, the glacial surface current (~ 1.0 m/s) is still stronger than the modern one (~ 0.7 m/s) (Figure 4.6b). The Kuroshio was the strongest when at south of Japan but weakened as it reached the KE region. The current speed at section 146 ° E (Figure 4.7b) exceeds 0.4m/s in 0 ka BP, reduced by ~ 0.2 m/s in 6 ka BP and by ~ 0.1 m/s in 30 and 35 ka BP but increased by ~ 0.1 m/s during the LGM.

Based on the annual mean current, the upper 1000 m integrated volume transport stream function was calculated as $\Psi(x,y) = \int_{x_E}^{x}\int_{-1000\,m}^{0} v(x,y,z)dzdx$, where Ψ is the stream function, x_E denotes the eastern boundary of the Pacific, and $v(\mathrm{x},\mathrm{y},\mathrm{z})$ are the northward velocities at points with x, y, and z coordinates (i.e., longitude, latitude, and depth, respectively). In Figure 4.11, the contours at 0 ka BP and 6 ka BP have similar distributions and values. As the 20 and 30 Sv contours show, the KC transports tropical water into the continental shelf-break northeast of Taiwan. In the region southeast of Kyushu, the KC merges with the Ryukyu Current flowing northeastward along the eastern slope of the Ryukyu Islands; therefore, the Kuroshio volume transport is significantly increased after exiting the ECS through the Tokara Strait. In the region south of Japan, anticyclonic recirculation always exists and contributes to the Ryukyu Current. Compared to the stream-function contours at 0 ka BP, the southern boundary of the subtropical gyre in the glacial ages is further south. In addition, there is a larger amount of water transported by NEC to mid-latitude regions in the glacial ages, indicating stronger subtropical gyres in the glacial ages compared to those at 0 and 6 ka BP.

We calculated the volume transport in the upper 1000 m at seven sections (S1–S7; Figure 2.2a) across the main currents in the northwest Pacific subtropical gyre (Table 4.2). This shows that the volume transport values at 0 ka BP are comparable to the observed values, and appear to be very similar to the values at 6 ka BP. However, the volume transport in the glacial ages intensified relative to 0 ka BP. The NEC (i.e., the origin of the Kuroshio) exhibited large significant increases of 16.4, 17.1 and 13.6 Sv in westward volume transports at LGM, 30 ka BP, and 35 ka BP, respectively. This was also evident in the volume transport stream function (Figure 4.11). Based on the values at S1 to S3 (Table 4.2), the Kuroshio bifurcates from NEC, thereby further increasing the northward volume transports, which were 13.4, 14.0, and 9.3 Sv at the LGM, 30 ka BP, and 35 ka BP, respectively, all of which are greater than the volume transport at 0 ka BP. Conversely, the glacial MC exhibited slightly decreased volume transport. Therefore, during the glacial ages, most of the increased NEC transport was supplied to the KC.

The KC flows northward along the east Philippine coast and exchanges water with the South China Sea through the Luzon Strait. The 0 ka BP volume transport in the upper 1000 m across the Luzon Strait was westward and eastward at 25.1 and 18.5 Sv, respectively. Net volume transports were westward and amounted to 6.6, 6.0, 1.4, 1.9, and 3.8 Sv at 0 ka BP, 6 ka BP, LGM, 30 ka BP, and 35 ka BP, respectively. The KC east of Taiwan is separated into two branches, one of which enters the ECS as the Kuroshio mainstream and the other that flows eastward along the southern edge of the Ryukyu Islands. The volume transports of both branches in the glacial ages were ~4.0 Sv, larger than those at 0 ka BP. In the ECS, the KC outflow through the Kerama Gap formed an anticyclonic recirculation in the region southeast of the Kerama Gap, while its volume transport increased by ~2.0 Sv in glacial ages compared to the values at 0 ka BP. Meanwhile, there was a slight increase of ~1.1 Sv in the glacial Kuroshio transport in the PN section. Eventually, the KC in the ECS and the Ryukyu Current merged to form the KC south of Japan. The net volume transport increased to 31.6 Sv (i.e., at 0 ka BP) at section ASUKA. The volume transports reached 39.2, 36.8, and 34.1 at the LGM, 30 ka BP, and 35 ka BP periods, respectively; such increased meridional transports are evident in Figure 4.4.

4.3.2 North Equatorial Current and its bifurcation latitude

The annual mean surface currents in the equatorial region are shown in Figure 4.12, which shows that the westward flow of NEC splits into northward and southward boundary currents of the KC and MC, respectively. The MC turns eastward and feeds the NECC. Near the sea surface (0–100 m), the velocity of the NEC exceeds 0.1 m/s within the broad area between 9° and 15° N. As defined, the NEC bifurcation latitude is the point where the averaged meridional flow within 2° band off the Philippine coast (blue line in Figure 4.12) is zero (Kim et al., 2004). The NEC bifurcates at 14.1° N into western boundary currents at 0 and 6 ka BP. As the comparison of NEC bifurcation latitude shows, this bifurcation shifts southward in the glacial age, which is located at 12.6, 12.5, and 12.7° N at LGM, 30 ka BP, and 35 ka BP, respectively, moving about southward by 1.5°, 1.6°, and 1.4°. Moreover, the NEC strengthens in the glacial age, but with a narrower latitudinal band.

Figure 4.13 shows the vertical structure of the annual mean zonal velocity at section 130° E when the NEC enters the Philippine Sea. The Subtropical Countercurrent (STCC) flows eastward at 19–22° N from 6 ka BP to the present day, but it reaches a depth of 300 m during the glacial age, which is deeper than the depth (~150 m) at present. At 0 and 6 ka BP, the velocity of the NEC exceeds 0.04 m/s in the latitudinal band between 9° and 18.5° N at the surface, and the NEC shifted northward with increasing depth and extended to ~21° N at 400 m. The NECC flows eastward south of 9° N, having two maxima (velocity higher than 0.20 m/s) at the surface at 3.8° N and subsurface (~100 m) at 8° N. Furthermore, the maximum speed of the NEC exceeds 0.24 m/s at ~10.7° N, moving northward to 12.4, 12.0, 11.5° N at LGM, 30 ka BP, and 35 ka BP, respectively. In the glacial age, the depth of NEC deepens, and at the same time, the latitudinal range of the upper NEC shifts southward, resulting in a decrease in the latitudinal amplitude of NECC, so the NECC becomes narrower and only has one maximum velocity core at the surface.

The bifurcation latitude of NEC is usually defined as the location where western currents reverse. The bifurcation of NEC for each age in the upper 500 m is shown in Figure 4.14. The vertical distributions of the NEC bifurcation were very similar at 0 and 6 ka BP. The annual average bifurcation appears at 13.3° N at the surface and it moves toward the north with increasing depth, reaching 17.3° N at 500 m. The latitude of zero meridional velocity at the surface (500 m) moves southward in the glacial age, approaching 12.4° N (14.4° N), 12.2° N

(14.3° N), 12.6° N (14.9° N) at LGM, 30 ka BP, and 35 ka BP, respectively. It is noticeable that the northward tilting extent of the bifurcation from the surface to 500 m decreases during the glacial age, and the smallest tilt amplitude (2°) occurs at the LGM.

As mentioned in Section 3.3.1, the northward flow of the NEC (i.e., the Kuroshio) shows a significant increase in volume transport in the glacial age. Figure 4.14 also demonstrates the enhanced Kuroshio and MC with little change in glacial age.

4.3.3 Past sea surface temperatures in the Kuroshio region

We calculated the modeled ΔSST, and the distributions are presented in Figure 4.15. In the paleo-ocean, the greatest ocean cooling occurred during the LGM, and the most significant cooling area was in the Kuroshio–Oyashio confluence region, cooling more than 1 and 6°C at 6 ka BP and glacial ages, respectively. In the open sea of the subtropical region, the SST at 6 ka BP became cooler in the western area and slightly warmer in the eastern band-like area. In the western equatorial region, the SST at the LGM appears to be 1–2°C lower than the current annual mean SST; however, the SST shows regional warming in the area of 150 –180° E at 30 and 35 ka BP.

The distributions of annual mean ΔSSTs and summer ΔSSTs in the Kuroshio region are depicted in Figure 4.16 and Figure 4.17, respectively. Looking at the modeled ΔSSTs of the Pacific Ocean east of the Ryukyu Islands in Figure 4.16, SST cooling values are less than 0.5°C at 6 ka BP, 2–3°C at LGM, and 1–2°C at 30 and 35 ka BP relative to the present SST. Notably, the strongest cooling occurred during the LGM. In the ECS along the Kuroshio path, SST cooling was greater on the nearshore side than on the offshore side. On the offshore side, the SST cooled little during the 6 ka BP period and approximately 1–2 °C during the glacial period. On the nearshore side, glacial SSTs decreased more, probably due to the weaker surface current along the coastal area. In the northern ECS, there has been a remarkable cooling in the SST_{LGM}

by 4–5 °C because the Tsushima Strait was closed during the lowest stand of sea level, and the influence of the KC weakened. The KC during 30 and 35 ka BP period was still able to transport warm water to the Japan Sea through the Tsushima Strait, so the SSTs were cooler than their temperature today by 3–4 °C. Moreover, due to the shoreward migration of the Kuroshio axis in the glacial age, the SSTs in south-central Japan became warmer. In the KE region, the SST in the glacial age cooled by more than 6°C on the northern side and 1–2°C on the southern side. In addition, the distributions of the summer ΔSSTs (Figure 4.17) show similar characteristics; however, the SST cooling in summer was weaker than the average annual cooling in the western equatorial region of glacial time.

To reconstruct paleo-SSTs, previous studies have used multiple proxies, and some of them, such as alkenone unsaturation ($\mathrm{U}_{37}^{\mathrm{K}'}$), oxygen isotopes, and radiolarians, were used to estimate the annual mean SST. In the ECS, the Mg/Ca ratio has been used as a proxy for SST in summer (Kubota et al., 2010; Sun et al., 2005) or from June to November (R. A. Kim et al., 2015). In our study, we considered the Mg/Ca-derived SST to be the SST from July to September. We collected paleo-SST records from previous literature and interpolated the modeled SST to core coordinates. As each proxy can be uncertain during SST estimation, we calculated the SST differences ($\Delta\mathrm{SST} = \mathrm{SST}_{\mathrm{past}}\text{-}\mathrm{SST}_{0\mathrm{ka}}$) and compared proxy-based ΔSSTs with modeled ΔSSTs, as shown in Figure 4.16 and Figure 4.17. The values of proxy-based ($\mathrm{U}_{37}^{\mathrm{K}'}$, oxygen isotopes, and Mg/Ca ratio) ΔSSTs were consistent with that of modeled ΔSSTs, and modeled ΔSST is mainly within 2°C of the proxy-based estimates, except for the eastern side of the Japan Sea, where the $\mathrm{U}_{37}^{\mathrm{K}'}$-derived SST differed significantly from the model results. Moreover, the radiolarian assemblage and diatom-based Td′ showed large differences from the model results in the southern portion of the South China Sea and the Kuroshio–Oyashio confluence, and these proxies had insufficient observations.

In the KC region, excluding the coastal area, none of the reconstructed paleo-SSTs had a steep drop, suggesting that the paleo-Kuroshio still transported tropical warm water into the Okinawa Trough and had a significant effect on the downstream area. Now that the modeled ΔSST values were comparable to those reconstructed ΔSSTs, the real paleo-Kuroshio paths may be close to the results from our model (Figure 4.5).

4.4 Discussion

4.4.1 Kuroshio path and surface velocity

Compared to the present location of the KC in the ECS, the KC axes shift slightly seaward during the LGM and 30 ka BP (Figure 4.7a). Such a southeastward shift has also been reported in another ocean model study (Vogt-Vincent & Mitarai, 2020) and suggested by a sediment core study (Kubota et al., 2017).

To date, only a limited number of cores have been used to understand glacial KE, and its position remains unclear. Sawada and Handa (1998) examined the temporal variations in latitudinal SST differences (ΔSST) at Izu Ridge (i.e., stations 14, 19, and 20; Figure 4.5) and suggested that the KC axis moved northward in association with a small meander off the coast of central Japan from 21 to 19 ka BP. Variations in latitudinal ΔSST were also calculated by Yamamoto (2009) using three sediment cores (i.e., stations 19, 20, and MD01-2421; Figure 4.5), and the evaluated latitudinal KE shift confirmed a northward shift of more than 1.0° from 26 to 20 ka BP, except for 22 ka BP when the KE axis exhibited no latitudinal shift. In contrast, evidence from pollen transport in the Central Pacific (34° 54.25´ N, 179° 42.18´ E) revealed a minor southward KE shift during glacial periods (Kawahata and Ohshima, 2002).

In our study, the KC axes southeast of Japan (136.5–142.0° E) migrated northward by about 0.8° at 138.5° E during the glacial ages. The northern limit of the KE axis at 6 ka BP, LGM, 30 ka BP, and 35 ka BP exhibited southward migrations of 1.1, 1.9, 2.0, and 2.4°, respectively. Similarly, the mean zonal wind-stress curl (Figure 4.2) reveals that the zero wind-stress curl at 0 ka BP is located at 41.2° N, and it migrates southward by 0.2, 1.1, 0.9, and 1.1° at 6 ka BP, LGM, 30 ka BP, and 35 ka BP, respectively. Therefore, the southward migrations of the KE axes are likely closely related to the zero wind-stress curl positions. Different latitudinal displacements of the KE can change the distribution of glacial sea surface temperature, which will be reported in the next section. We note that the KC path south of Japan depended more on the local topography and upstream conditions rather than the position of the zero wind-stress curl.

4.4.2 Wind-driven Sverdrup-transport stream function

In the North Pacific subtropical gyre, NEC is a westward flow on the southern side and KE is a component of the northern boundary. As the wind fields (Figure 4.2) shifted southward during the glacial ages, the NEC and KE latitudes exhibited southward displacements, indicating a southward shift of the North Pacific subtropical gyre. A more southerly position of the NEC bifurcation results in a stronger Kuroshio transport (Hu et al., 2015; Y.-L. Wang & Wu, 2018; Weiss et al., 2021). Earlier LGM simulations have suggested decreased Kuroshio transport in the ECS during the LGM (Kao et al., 2006; Lee et al., 2013; Vogt-Vincent & Mitarai, 2020; Zheng et al., 2016). However, these models either only considered the effect of sea-level lowering during the LGM or neglected the NEC influence on KC strength. As indicated by the planktonic foraminifera P. obliquiloculata abundance (POA), the KC intrusion into the middle Okinawa Trough was significantly reduced during low sea-level conditions from 40 to 16 ka BP (Chang et al., 2008; D.-W. Li et al., 2018; Z. Xu et al., 2017). In contrast, the reconstructed subsurface water temperature and organic matter in the middle Okinawa Trough suggest that the KC likely had a stronger transport during the LGM (Kubota et al., 2017). In our simulations, the glacial KC in the southern and middle Okinawa Trough increased with a higher surface velocity, which is due to the stronger NEC, as shown in Section 4.3.

Existing multi-proxy reconstructions in the northern Okinawa Trough suggest a weakened Kuroshio intrusion from 35 ka BP to the LGM; the KC reached its present strength at 8 ka BP (Ijiri et al., 2005; Shi et al., 2014; Y. Ujiié et al., 2016; Vats et al., 2020; Yamamoto et al., 2013). In our study, compared to the present, the Kuroshio intrusion into the northern Okinawa Trough was reduced with a weaker current speed in the glacial ages. The Tsushima Strait was closed at the LGM and narrow at 30 and 35 ka BP, leading to a decrease in transport through the Tsushima Strait. Moreover, the KC axis exhibited a southward displacement in the northern Okinawa Trough, which also reduced the northward Kuroshio transport separation.

To quantify the subtropical circulation changes in the five ages considered, we zonally integrated the volume transport from the east coast to 137° E for the annual mean transport stream function at different latitudes (represented by solid lines in Figure 4.18). At 0 and 6 ka BP, the meridional transport was northward south of 14° N, zero at 14° N, and southward north of 14° N. During the three glacial ages, the meridional transport was zero at 13° N, while exhibiting a southward shift (Figure 4.18), with values increasing by approximately 10 Sv from 13 to 25° N, indicating a stronger subtropical gyre. Sawada and Handa (1998) analyzed sediment cores from central Japan and suggested the presence of a stronger subtropical North Pacific circulation from 21 to 19 ka BP. Additionally, an ensemble of general circulation models displayed strengthening of the North Pacific subtropical gyre during the LGM (Gray et al., 2020). Therefore, the North Pacific subtropical gyre tended to be stronger and shifted southward during glacial periods.

Based on Sverdrup theory (Sverdrup, 1947), we used Equation (3.2) to calculate the corresponding wind-driven Sverdrup transport from the east coast to 137° E (dashed lines in Figure 4.18). The enhanced North Pacific subtropical gyre during the glacial ages can be partly explained by the stronger wind-stress curl and trade winds (Figure 4.2). From 13 to 25° N, the wind-driven Sverdrup transport agreed with gyre strengthening during the glacial ages.

However, the Sverdrup transport north of 25° N was weaker in the glacial ages than at 0 and 6 ka BP, which is in contrast to gyre strengthening during these periods. (Figure 4.18). Hogg and Gayen (2020) suggested that surface buoyancy fluxes (i.e., mainly heating and cooling in the ocean surface) are essential for the ocean-gyre transport. A significant amount of cooling (Figure 4.1) was evident over the Kuroshio region during the glacial ages in our model forcing. Therefore, it is possible that the circulation north of 25° N was driven by the buoyancy forcing rather than the wind stress.

4.4.3 Bifurcation latitude of the NEC

As Table 4.3 shows, in our model, the NEC bifurcation at 0 ka BP was located at 13.3° N at the surface, and the position of the bifurcation point shifted northward with increasing depth, reaching 17.3° N at a depth of 500 m, which was consistent with the previously observed results (Qu & Lukas, 2003) as well as the model results (Guo et al., 2019; Y. Y. Kim et al., 2004; J. Li & Gan, 2022). Compared to the modern location of NEC bifurcation, the bifurcation latitude at the surface (500 m) moved southward about 0.1° (0°), 0.9° (2.9°), 1.0° (3.0°), and 0.7° (2.4°) at 6 ka BP, LGM, 30 ka BP, and 35 ka BP, respectively. We found that this northward shift with depth became smaller during the glacial period.

The upper ocean gyres in the Pacific and tropical circulation are mainly driven by the wind (Talley et al., 2011). The classic Sverdrup theory predicts that the bifurcation of NEC should lie where the basin-scale zonally integrated wind stress curl is generally zero (Sverdrup, 1947). In the Pacific Ocean, the long-term change in the annual mean NEC bifurcation corresponded to the latitudinal shift of the zero-wind-stress curl line integrated from east to west (Chen & Wu, 2012). The distributions of the annual mean wind stress curl and zonal integrations of the stress curl are shown in Figure 4.19. The zonally averaged wind stress curl in the subtropical gyre was stronger than that in the tropical gyre. The zero-wind stress curl line was positioned at 15.2, 15.0, 13.9, 13.8, and 14.2° N at 0 ka BP, 6 ka BP, LGM, 30 ka BP, and 35 ka BP, respectively. Therefore, the zero-wind stress curl line shifted to south by 0.2°, 1.2°, 1.4°, and 1.0°, respectively, consistent with the shift of the NEC bifurcation at the surface.

According to the previous 5.5-layer reduced gravity model results (Guo et al., 2019), the intensity difference of the wind stress curl between the subtropical and tropical gyres plays an important role in the poleward tilting bifurcation with increasing depth. As defined in this study, the wind stress curl ratio (r_{curl}) is the ratio of the wind stress curl intensity of the subtropical gyre to that of the tropical gyre, and the bifurcation latitude slope (s) is the degree of tilting. It is assumed that the bifurcation slope increases when the wind-stress curl ratio increases. We calculated the r_{curl} and slope for different ages, as shown in Table 4.3. The wind stress curl ratio at 0 ka BP was 2.24 with a bifurcation slope 8.0×10^{-3} °/m, w similar to the values calculated by Guo et al. (2019). The values for wind stress curl ratio (bifurcation slope) were 2.32 (8.2×10^{-3} °/m), 1.95 (4.0×10^{-3} °/m), 1.83 (4.2×10^{-3} °/m), and 1.88 (4.6×10^{-3} °/m) at 6 ka BP, LGM, 30 ka BP, and 35 ka BP, respectively. The intensity of subtropical circulation was stronger than that of tropical circulation, and the ratio of their intensities was smaller in the paleo-ocean than in the modern ocean. However, the wind stress curl ratio was not positively correlated with the bifurcation slope, as there was a discrepancy during the LGM.

4.4.4 A Kuroshio intensity indicator

KC intensity strongly affects the Okinawa Trough water temperature. Using reconstructed Okinawa Trough water temperatures, many studies have examined Kuroshio intensity variation since the LGM. The $U_{37}^{K'}$ proxy is typically used as an annual mean SST index (Kim et al., 2015) and the TEX_{86} proxy most likely reflects subsurface (i.e., < 200 m) water temperature (Jia et al., 2012; Li et al., 2013; Li et al., 2020; Lin et al., 2017; Ruan et al., 2017; Zhang & Liu, 2018; Zhao et al., 2015). These studies considered that a weaker KC leads to a shallow mixed layer and smaller vertical thermal gradient, whereas a stronger KC results in a deep mixed layer and larger vertical thermal gradient. The vertical thermal gradient can be estimated from the difference between $U_{37}^{K'}$ and TEX_{86} derived temperature, i.e., $\Delta T = SST_{U_{37}^{K'}} - SubST_{TEX_{86}}$;hence, ΔT has been used as an indicator of the KC intensity and evolution (Li et al., 2020; Ruan et al., 2017).

The surface thermal buoyancy flux and local wind speed also affect the depth of the thermocline or the surface mixed layer (Wang et al., 2016). Therefore, it is necessary to confirm the relationship between ΔT and KC intensity in studies of these sediment cores. We calculated the annual mean ΔT from the model results and compared it to the modeled surface current speeds at the two core sites (Table 4.4). According to Table 4.4, a stronger KC corresponds to a higher ΔT.

Thus, the idea that a stronger KC results in a lower ΔT value is incompatible with ocean dynamics. According to the thermal wind relationship, the vertical geostrophic-flow variation is proportional to the horizontal water-temperature gradient; a larger horizontal temperature gradient corresponds to a stronger KC. As described earlier, the SST in the Kuroshio region was affected not only by the Kuroshio speed, but also by the air-sea heat flux and local wind forcing. Consequently, subsurface water temperature, rather than SST, was sensitive to variations in Kuroshio intensity (Kubota et al., 2017).

We hypothesized that the horizontal thermal gradient of subsurface water temperature would be more appropriate as a KC intensity index than the vertical thermal gradient. To confirm this idea, we calculated the difference between the modeled subsurface (i.e., 200 m) water temperatures (i.e., $\Delta T_H = SubST_{DGKS9603} - SubST_{DGKS9604}$) between the DGKS9604 and DGKS9603 cores (Figure 1d). The ΔT_H values were 0.49, 0.50, 2.39, 2.00, and 1.49°C at 0 ka BP, 6 ka BP, LGM, 30 ka BP, and 35 ka BP, respectively. The maximum current speeds in the upper 200 (500) m were 0.92 (0.07), 0.93 (0.07), 1.47 (0.19), 1.44 (0.17), and 1.40 (0.13) m/s at 0 ka BP, 6 ka BP, LGM, 30 ka BP, and 35 ka BP, respectively. There was a significant correlation between ΔT_H and KC speeds; therefore, it is practical to evaluate KC surface strength by using the horizontal subsurface-temperature gradient across the KC.

4.5 Summary

Considering the changes in sea level, air-sea heat flux, and wind stress, our model results provide the evolution of the Kuroshio path, transport, and strength from 35 ka BP to the present. The 6 ka BP KC has the same path as the modern KC. It has been confirmed that, regardless of the sea-level and climate changes, the KC path remains inside the ECS. The Kuroshio axis in the glacial age shows a shoreward moving of its maximum core and the Kuroshio surface current also show two regimes: a weak one (~0.9 m/s) in 0 ka and 6 ka and a strong one in glacial ages (~1.4 m/s). The glacial KC appears to shift southward when it exits the ECS through the Tokara Strait and exhibits the southernmost shift during the LGM. Moreover, the glacial KC off the southeastern coast of Japan migrated northward with a small meander. Relative to present location of the KE axis, the northern limit of the KE axis at 6 ka BP, LGM, 30 ka BP, and 35 ka BP displayed southward migration of 1.1, 1.9, 2.0, and 2.4°, respectively. A comparison with the southward shift of the zero wind-stress curl revealed that the southward migrations of the KE axes may be closely related to the zero wind-stress curl migrations.

The Kuroshio in 6 ka was the same as the modern Kuroshio in transport and strength, but the glacial Kuroshio transport increased with a lower sea level. The NEC and KE are the southern and northern sides of the North Pacific subtropical gyre, respectively, and they exhibit southward migration during the glacial ages, indicating a southward shift of the North Pacific subtropical gyre. In addition, the subtropical gyre in the last glacial period became stronger and migrated southward, which can be partly explained by the stronger wind-stress curl and trade winds in the North Pacific.

The NEC bifurcation at 0ka BP was located at 13.3 °N at the surface, and the bifurcation latitude shifted northward with increasing depth, reaching 17.3°N at depth of 500 m. The bifurcation latitude at the surface (500 m) moves southward about 0.1° (0°), 0.9° (2.9°), 1.0° (3.0°), and 0.7° (2.4°) at 6 ka BP, LGM, 30 ka BP, and 35 ka BP, respectively. The zero-wind stress curl line shifted to south by 0.2, 1.2, 1.4, and 1.0°, respectively, consistent with the shift of the NEC bifurcation at the surface. The northward tilting of the NEC bifurcation became weaker during glacial time, which was not completely determined by the ratio of the wind stress curl intensity of the subtropical gyre to that of the tropical gyre.

In the search for an appropriate KC intensity indicator, we found that the upper-ocean vertical thermal gradient used in some studies was unsatisfactory; therefore, we suggest that it is better to evaluate KC surface strength using the horizontal subsurface-temperature gradient across the KC. This conclusion can facilitate future studies on the Kuroshio path and variations in its strength.

Figures

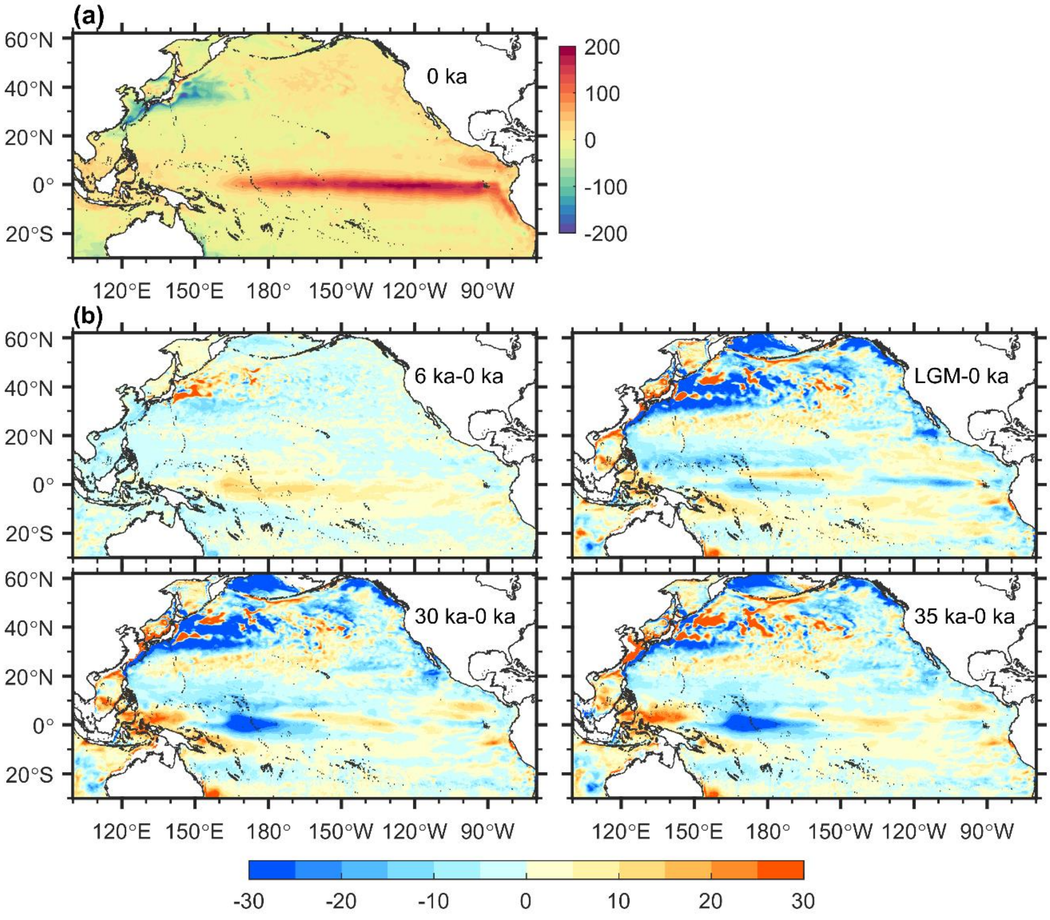

Figure 4.1 (a) Annual mean air-sea heat flux (unit: W/m^2) at 0 ka BP. Positive and negative values indicate ocean warming and cooling, respectively. (b) Differences in air-sea heat flux (unit: W/m^2) between four ages (i.e., 6 ka BP, LGM, and 30 and 35 ka BP) and 0 ka BP.

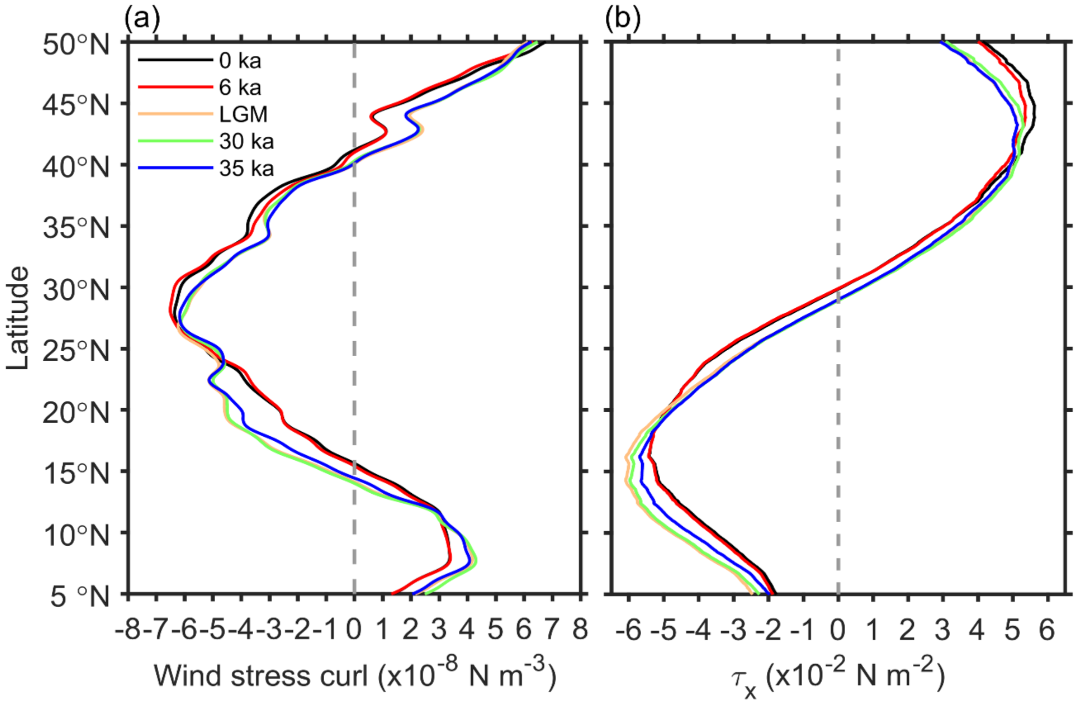

Figure 4.2 (a) Zonal mean wind-stress curls in the North Pacific (i.e., 100° E–80° W) in different ages. The gray dotted line corresponds to zero wind-stress curl. (b) Zonal mean eastward wind-stress component in the North Pacific in different ages.

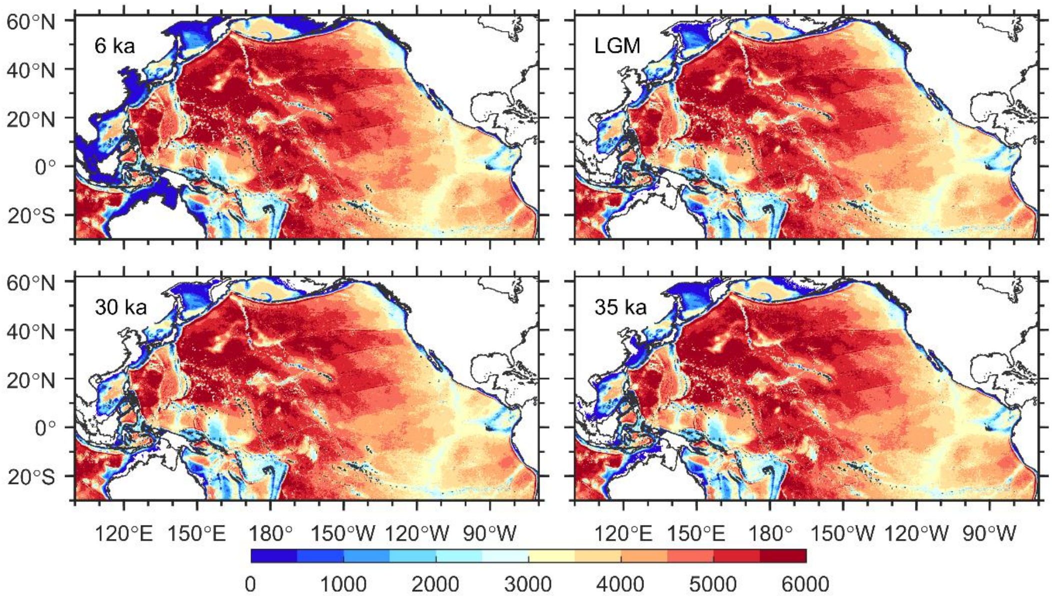

Figure 4.3 Bathymetry (unit: m) map for four ages (i.e., 6 ka BP, LGM, and 30 and 35 ka BP).

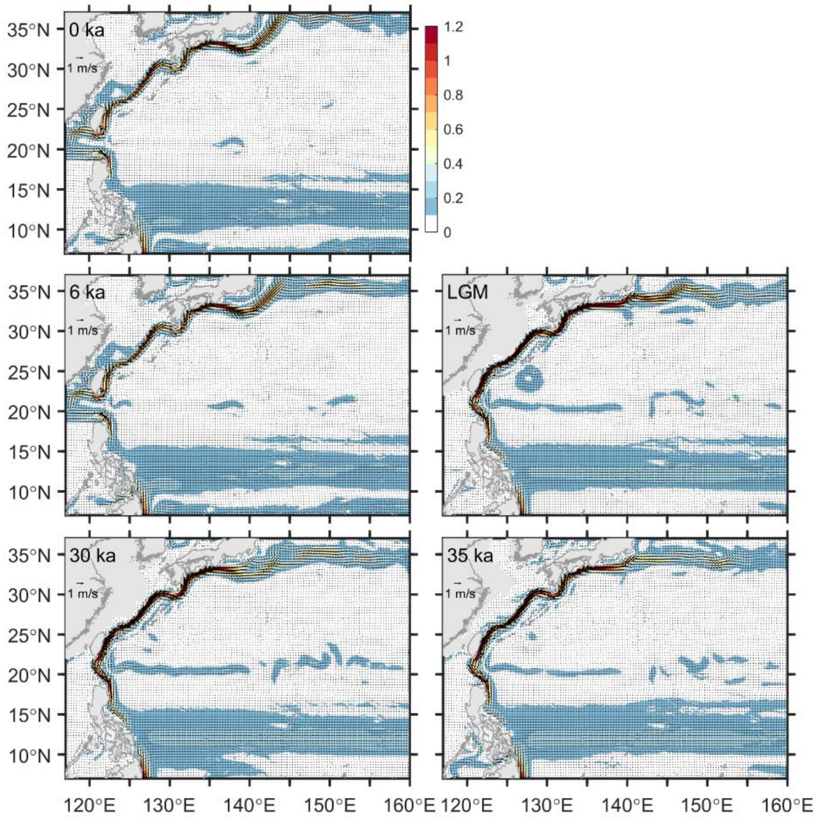

Figure 4.4 Annual mean surface current (0–100 m, unit: m/s) in the Northwest Pacific in five ages. Shading indicates the area where current speed exceeds 0.1 m/s.

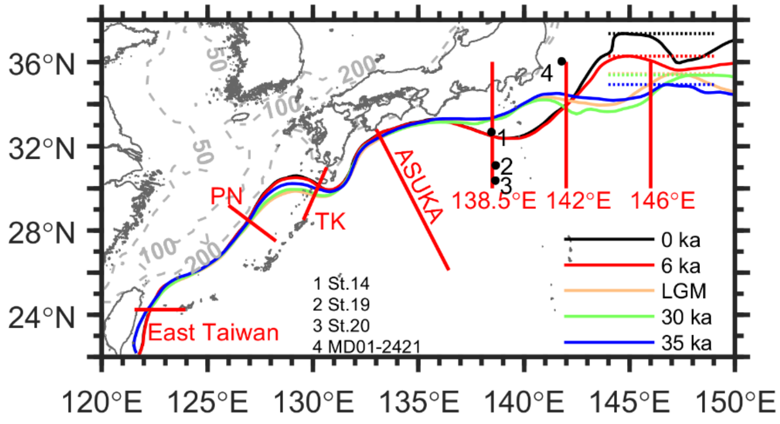

Figure 4.5 Kuroshio axes in five different experiments. Gray dotted lines indicate the East China Sea depths; other dotted lines indicate the northern KE limits. Red lines indicate sections for checking the velocity cores and water temperatures. Black circles (from 1 to 8) are the sediment cores discussed in our study.

(a) East Taiwan

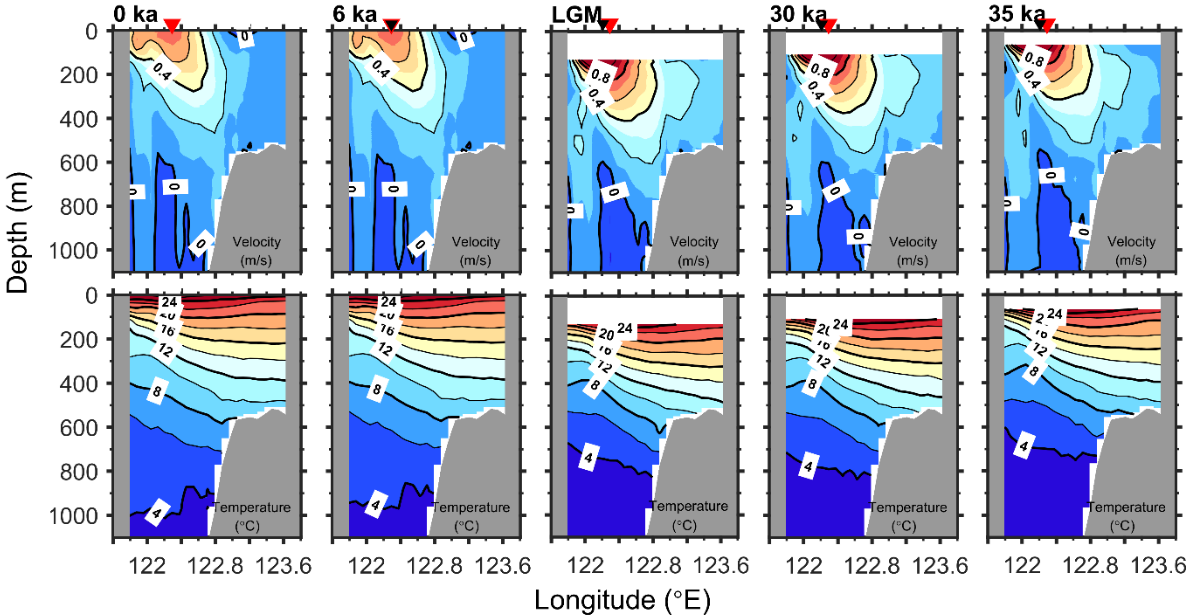

(b) TK line

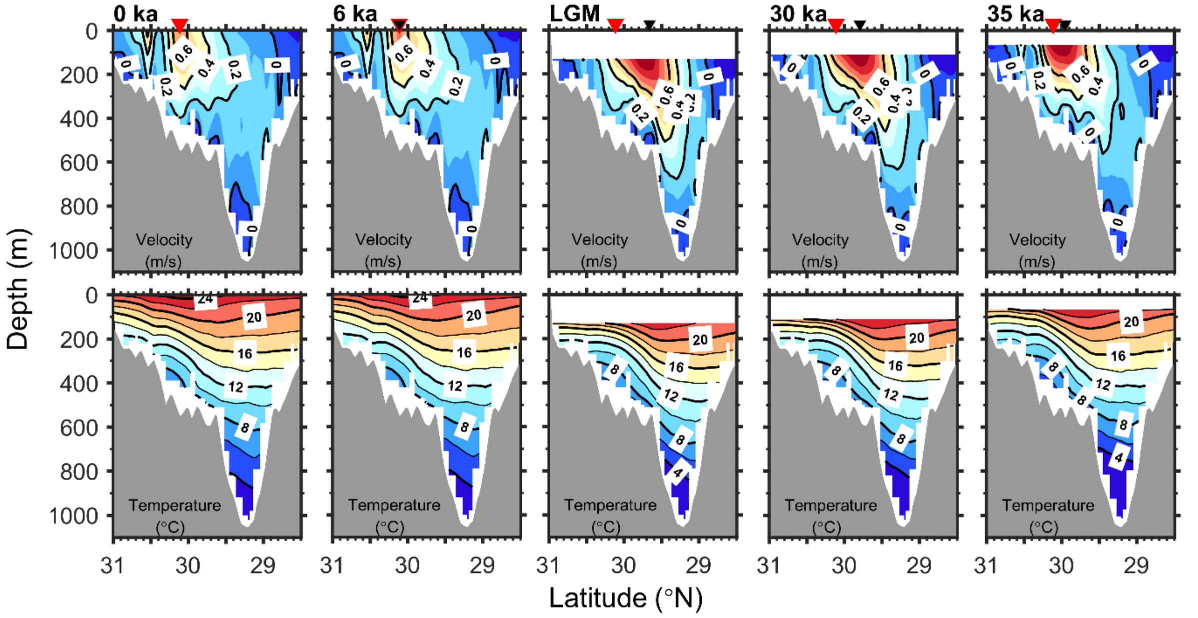

Figure 4.6 Vertical distributions of modeled velocity and potential temperature for the (a) East Taiwan and (b) TK line. Black contours in the upper panels indicate the current speed with a 0.2 m/s interval and those in the lower panels indicate the potential temperature with a 2°C interval. Inverted triangles indicate the locations of maximum current speeds at 0 ka BP (red) and paleo-ages (black).

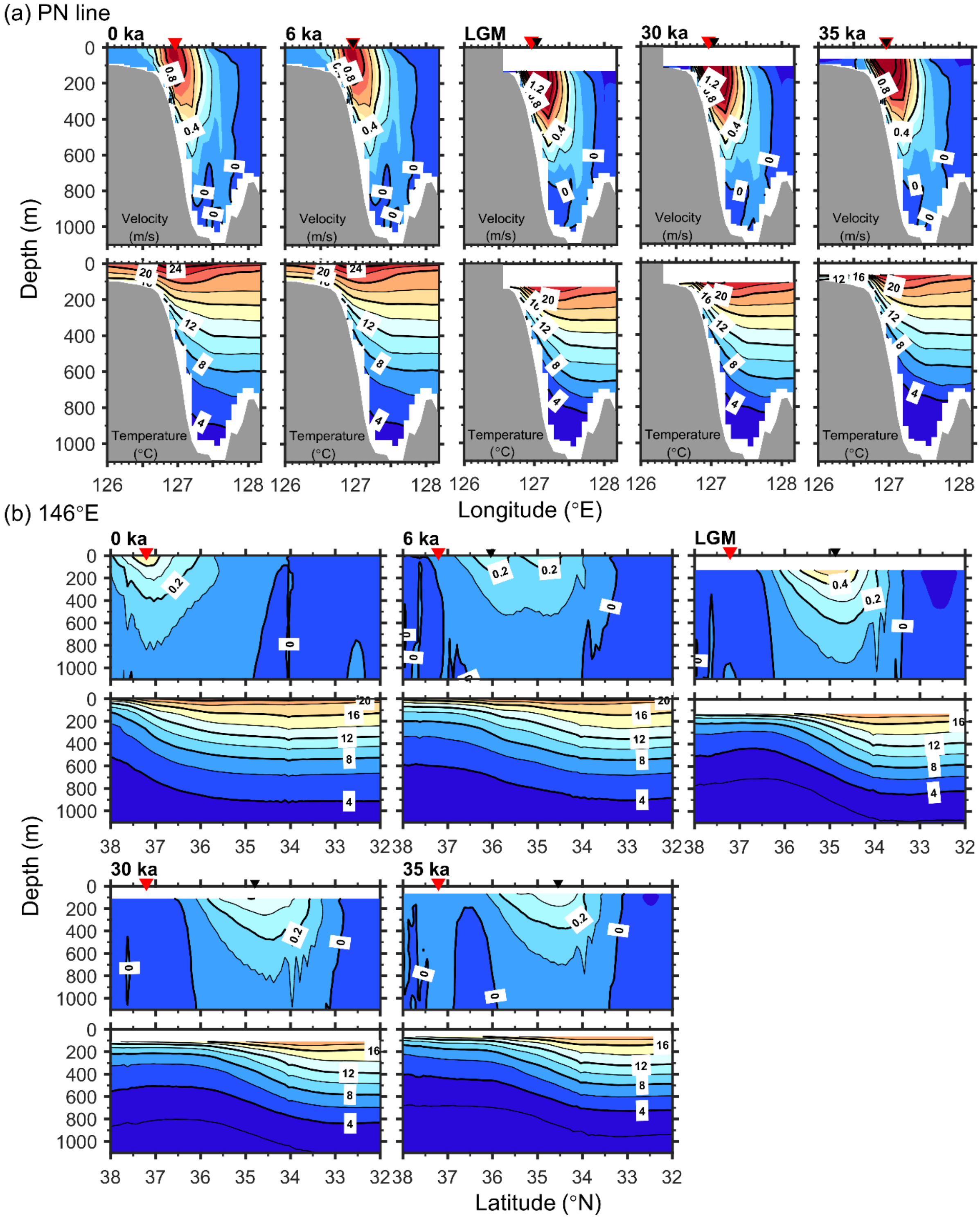

Figure 4.7 Vertical distributions of modeled velocity and potential temperature for (a) PN section and (b) 146° E. Black contours in the upper panels indicate the current speed with a 0.2 m/s interval and those in the lower panels indicate the potential temperature with a 2°C

interval. Inverted triangles indicate the locations of maximum current speeds at 0 ka BP (red) and paleo-ages (black).

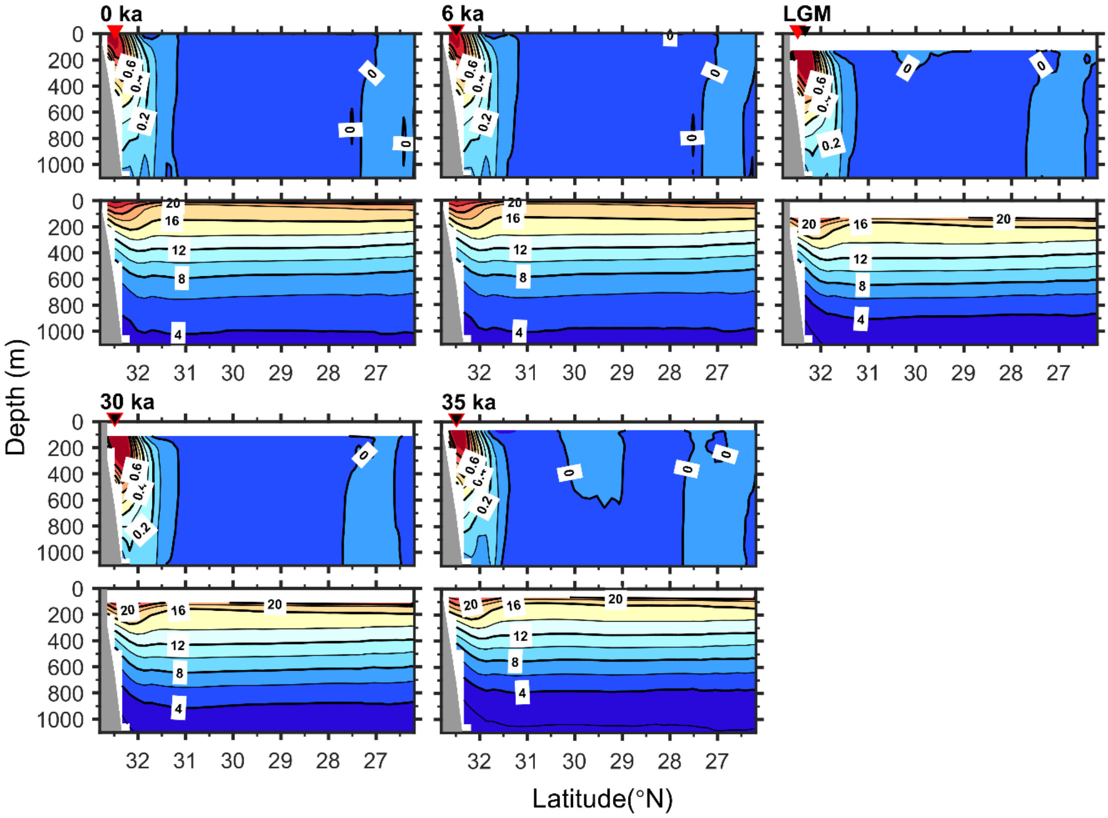

Figure 4.8 Vertical distributions of modeled velocity and potential temperature for the ASUKA line. Black contours in the upper panels indicate the current speed with a 0.2 m/s interval and those in the lower panels indicate the potential temperature with a 2°C interval. Inverted triangles indicate the locations of maximum current speeds at 0 ka BP (red) and paleo-ages (black).

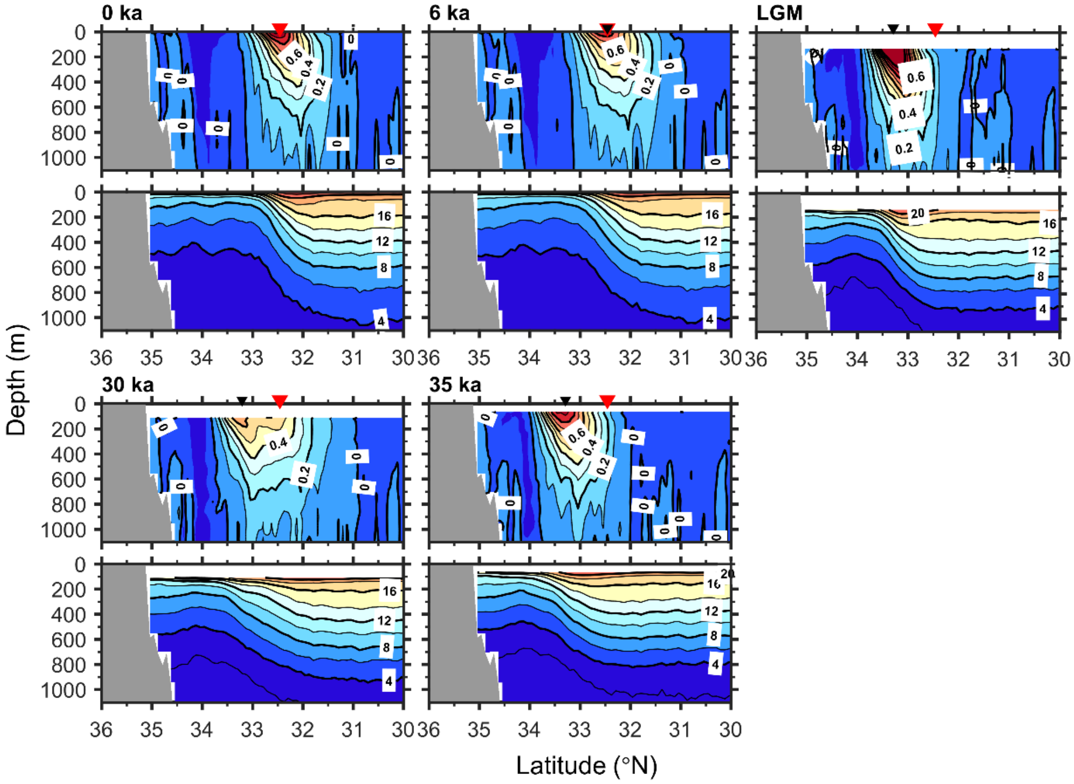

Figure 4.9 Vertical distributions of modeled velocity and potential temperature for 138.5° E. Black contours in the upper panels indicate the current speed with a 0.2 m/s interval and those in the lower panels indicate the potential temperature with a 2℃ interval. Inverted triangles indicate the locations of maximum current speeds at 0 ka BP (red) and paleo-ages (black).

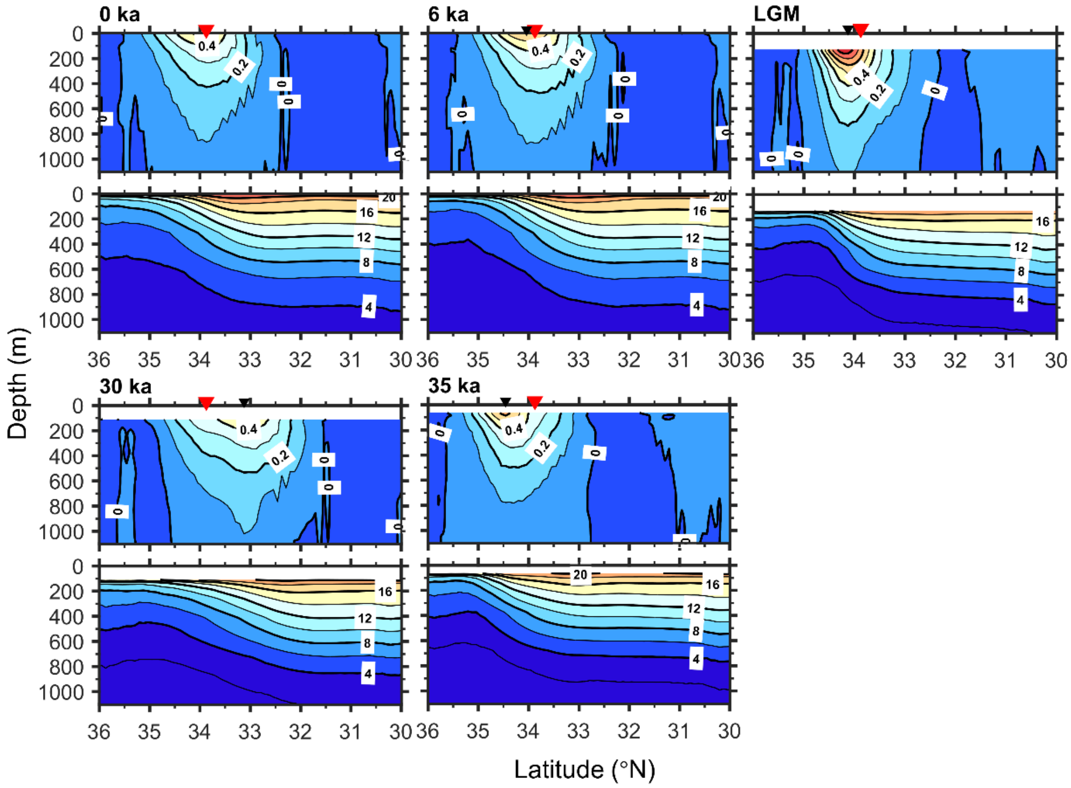

Figure 4.10 Vertical distributions of modeled velocity and potential temperature for 142° E. Black contours in the upper panels indicate the current speed with a 0.2 m/s interval and those in the lower panels indicate the potential temperature with a 2℃ interval. Inverted triangles indicate the locations of maximum current speeds at 0 ka BP (red) and paleo-ages (black).

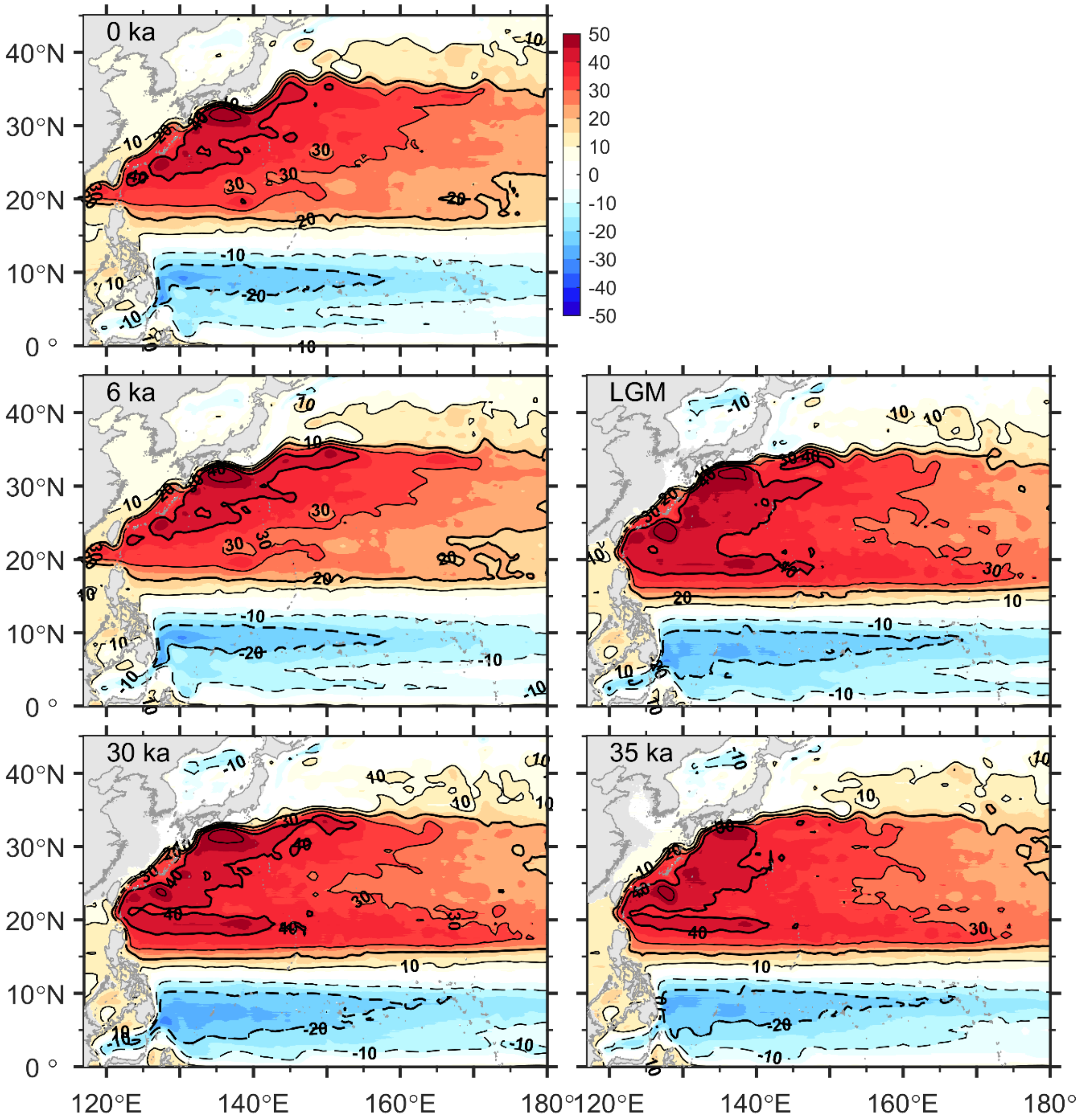

Figure 4.11 Integrated volume-transport stream function modeled for upper 1000 m (unit: Sv; 1 Sv = 10^6 m^3/s) in the five ages.

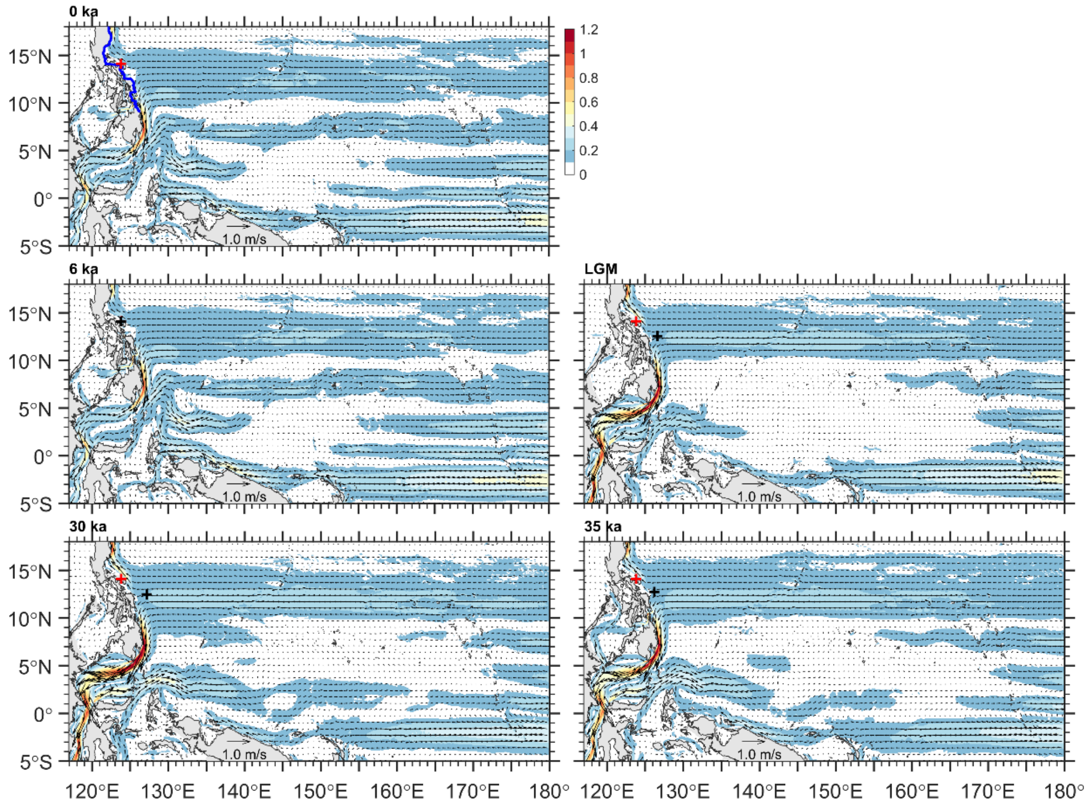

Figure 4.12 Annual mean surface current (0–100 m, unit: m/s). Shading indicates the area where the current speed exceeds 0.1 m/s. The red + indicates the NBL location at 0 ka BP, and the black + indicates the NBL location in paleo-age.

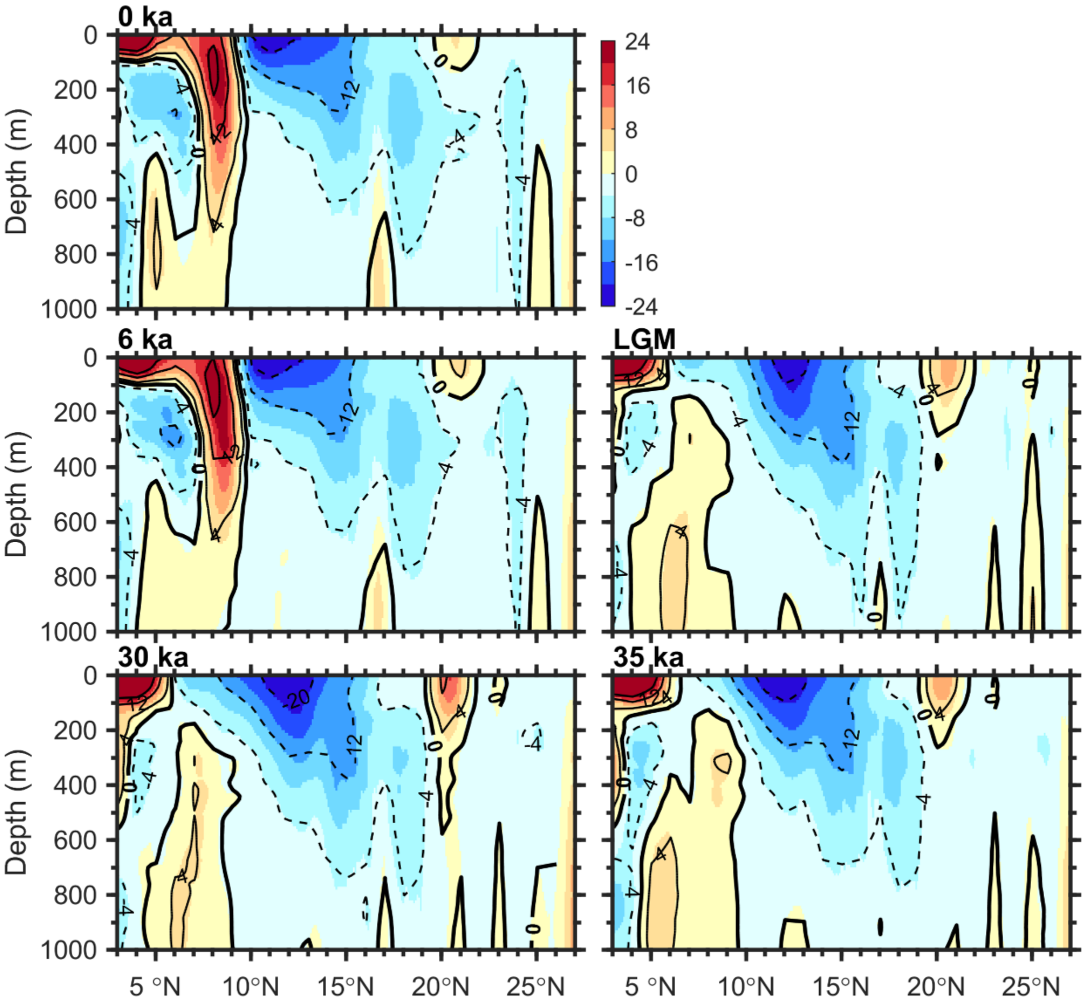

Figure 4.13 Annual mean zonal velocity at a section along 130° E. Shaded colors with contours indicate the zonal velocity U (unit: m/s). A positive value indicates eastward flow.

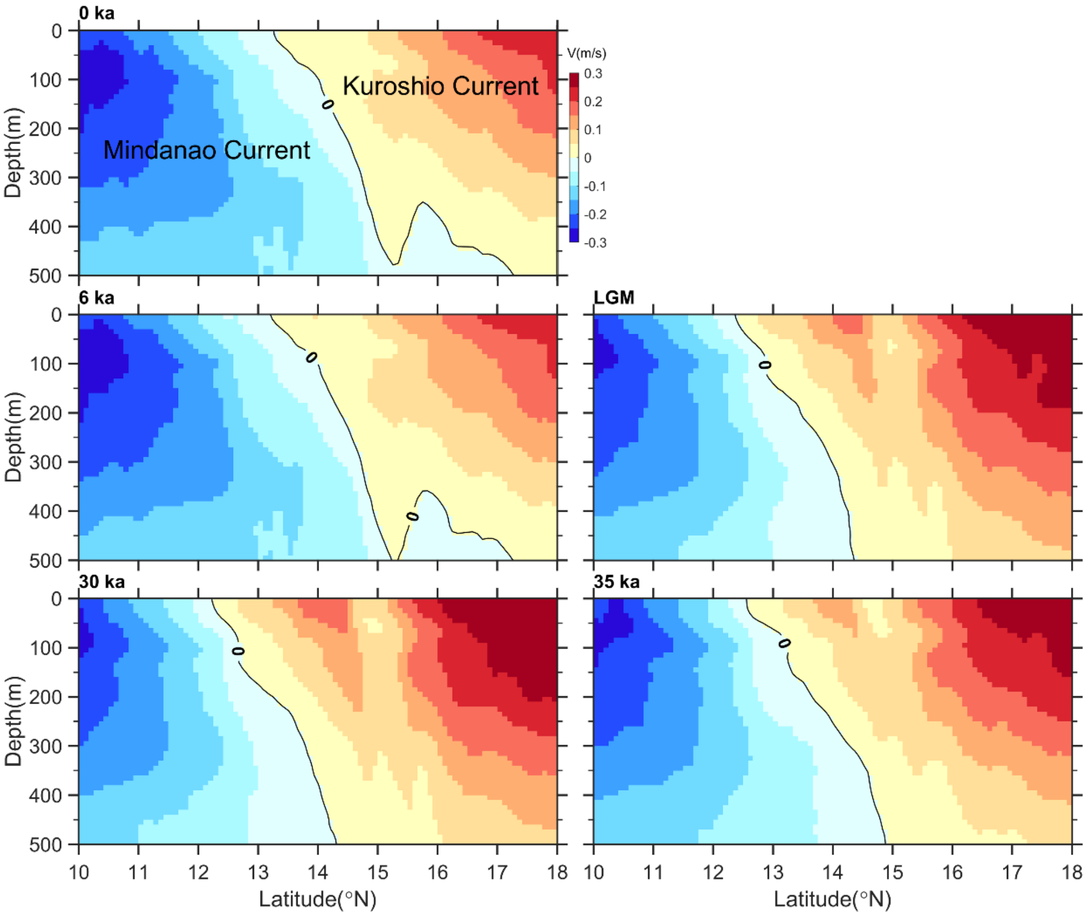

Figure 4.14 Annual meridional velocity (unit: m/s) averaged within a 2° longitude band off the Philippine coast. Positive values indicate northward flow, the Kuroshio Current, and negative values indicate southward flow, the Mindanao Current. The zero-contour velocity indicates the NEC bifurcation.

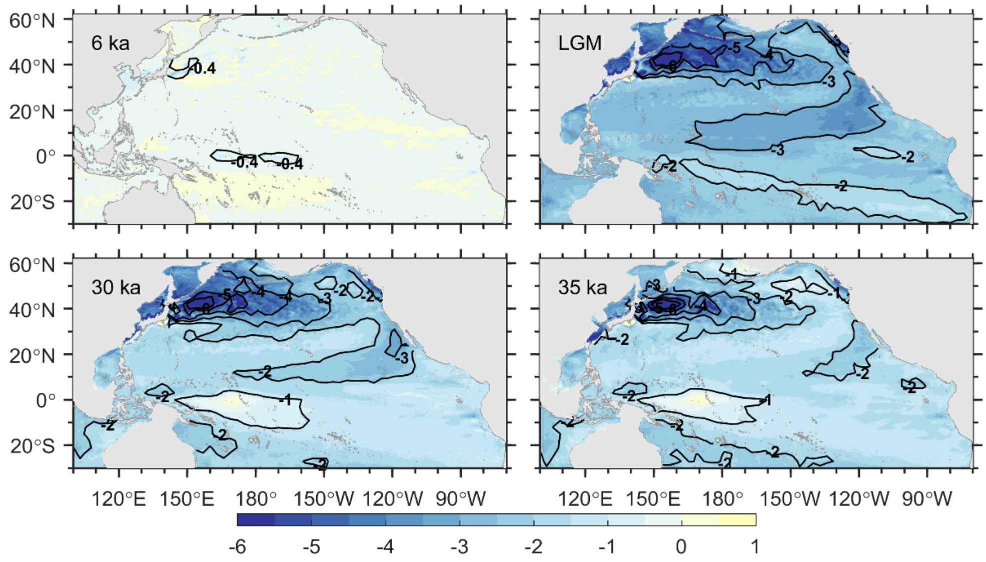

Figure 4.15 The distributions of annual mean ΔSSTs (unit: ℃). Shaded colors indicate model result ΔSST, which is paleo-SST minus SST (0 ka BP).

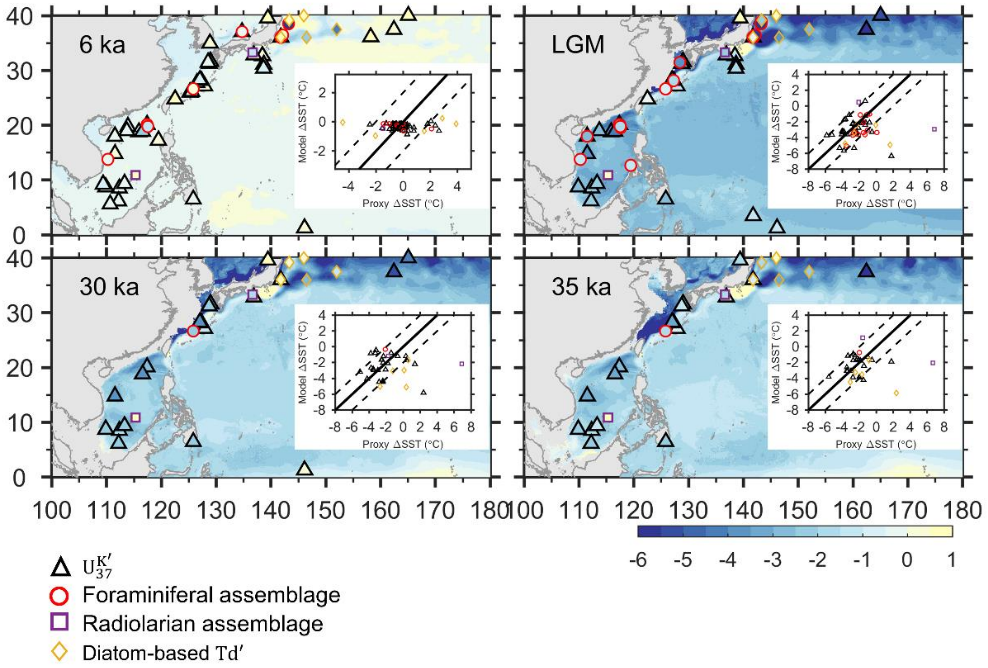

Figure 4.16 The distributions of annual mean ΔSSTs (unit: ℃) in the Kuroshio region. Shaded colors indicate model result ΔSST, which is paleo-SST minus SST (0 ka BP). Symbols represent different proxies used to reconstruct annual mean paleo-SSTs, and the shaded colors inside are proxy-based ΔSSTs. The figures inside compare the modeled SST with the proxy-based SST.

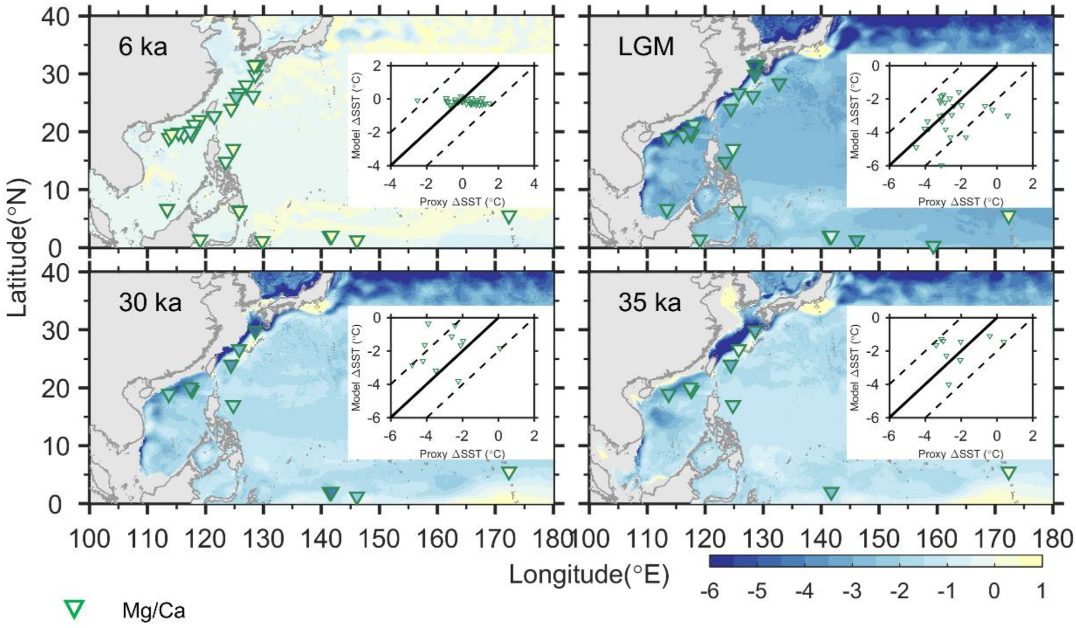

Figure 4.17 Same as Figure 4.13, but for summer ΔSSTs (unit: °C).

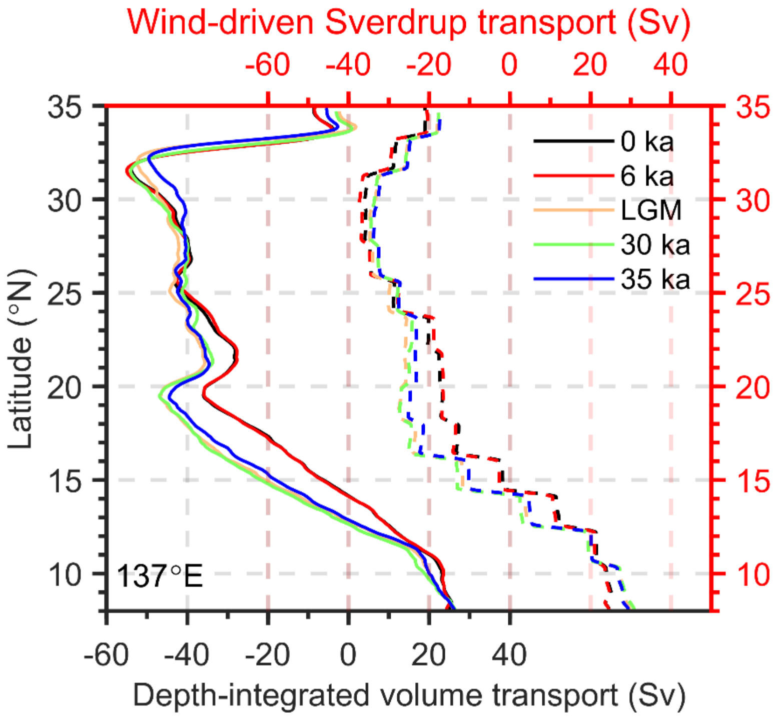

Figure 4.18 Zonally integrated values in Sv from the east coast to 137° E of modeled volume transport in the upper 1000 m (solid lines, with reference to the black axes) and wind-driven Sverdrup transport from the east coast to 137° E (dashed lines, with reference to the red axes). All the values are processed with a 0.25 degree running average.

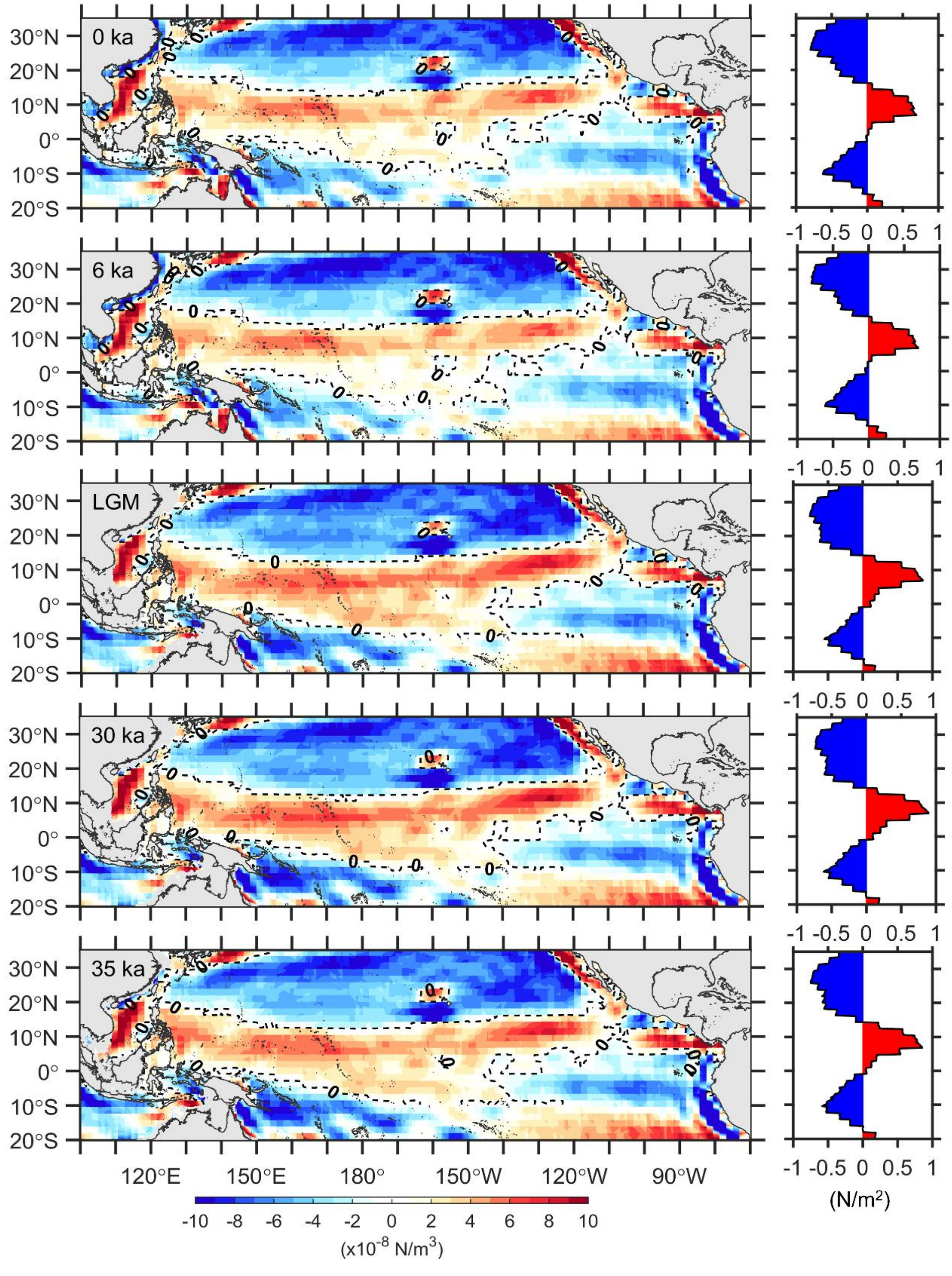

Figure 4.19 (Left) Wind stress curl of annual mean wind stress (shaded colors) and zero wind-stress curl (dashed lines). (Right) Zonally integrated stress curl as a function of latitude.

Tables

Table 4.1 Model settings for the five cases.

Case	**Sea level change (compared to 0 ka BP)**	**Initial velocity**	**Source of data for ocean temperature and salinity (including lateral boundary and sea surface)**	**Air-sea heat flux and wind stress**
0 ka BP	/	0	WOA2018	0 ka (NCEP)
6 ka BP	No change	0	6 ka (MIROC4m*)	6 ka (MIROC4m*)
LGM	-130 m	0	21 ka (MIROC4m*)	21 ka (MIROC4m*)
30 ka BP	-110 m	0	30 ka (MIROC4m*)	30 ka (MIROC4m*)
35 ka BP	-65 m	0	35 ka (MIROC4m*)	35 ka (MIROC4m*)

* MIROC4m data were modified based on the NCEP data.

Table 4.2 Annual mean volume transport in Sv in the upper 1000 m across the sections shown in Figure 2.2a.

Sections	Observations (Sv)	Volume transport (Sv)				
		0 ka	6 ka	LGM	30 ka	35 ka
S1 NEC	-37.6 ± 15.6[a]	-38.5	-38.0	-54.9	-55.6	-52.1
S2 Mindanao Current	-36.1 [b]	-40.6	-41.0	-38.6	-38.2	-39.0
S3 KC at 16.5°N	*	11.0	11.2	24.4	25.0	20.3
S4 East Taiwan	21.5 ± 2.5[c]	25.1	24.9	29.2	28.6	28.3
S5 PN	25.4[d]	23.6	23.6	24.7	24.5	24.2
S6 Tokara Strait	23.03 ± 3.31[e]	22.8	22.8	24.1	24.1	23.4
S7 ASUKA	29.0–40.2[f]	31.6	32.2	39.2	36.8	34.1

* No observations

[a] Schönau & Rudnick (2015). [b] Schönau et al. (2015). [c] Johns et al. (2001). [d] Hinada (1996). [e] Zhu et al. (2017). [f] Nagano et al. (2010).

Table 4.3 The NEC bifurcation latitude (NBL) and its latitudinal shift in paleo-ages. Note that negative values indicate southward migration. r_{curl} indicates the wind stress curl intensity ratio, and s indicates the bifurcation slope.

	NBL (° N)		Shift of NBL (°)		r_{curl}	s (x10^{-3}°/m)	Zero wind-stress curl (° N)	Shift of zero wind-stress curl (°)
	0 m	500 m	0 m	500 m				
0 ka BP	13.3	17.3			2.24	8.0	15.2	
6 ka BP	13.2	17.3	-0.1	0	2.32	8.2	15.0	-0.2
LGM	12.4	14.4	-0.9	-2.9	1.95	4.0	13.9	-1.2
30 ka BP	12.2	14.3	-1.1	-3.0	1.83	4.2	13.8	-1.4
35 ka BP	12.6	14.9	-0.7	-2.4	1.88	4.6	14.2	-1.0

Table 4.4 Modeled sea surface temperature (SST), subsurface temperature (SubST), their difference (i.e., ΔT = SST – SubST; unit: °C), and surface velocity (unit: m/s) at the ODP1202B and M063-05 sediment cores. The depth of SubST at the ODP1202B core is from Ruan et al. (2017) while that at the M063-05 core is from Li et al. (2020).

Period	ODP1202B				M063-05			
	SST (0–30 m)	SubST (30–80 m)	Velocity (0–80 m)	ΔT	SST (0–30 m)	SubST (30–200 m)	Velocity (0–200 m)	ΔT
0 ka BP	25.95	23.01	0.58	2.93	24.91	19.78	0.67	5.14
6 ka BP	25.79	22.85	0.59	2.94	24.74	19.62	0.66	5.11
LGM	22.67	19.27	1.10	3.40	23.06	16.44	1.20	6.61
30 ka BP	23.04	19.21	1.04	3.83	23.84	16.91	1.24	6.93

35 ka BP	23.68	19.82	1.34	3.86	23.68	17.15	1.16	6.52

Chapter 5: Conclusions and future research

5.1 Summary

Based on the meteorological and oceanic data provided by the different climate models, we considered the sea level, air-sea heat flux, and wind stresses and used an ocean model to investigate the ensemble mean of changes in the Kuroshio system during the LGM and the evolution of the Kuroshio path and intensity during the last 35,000 years.

First, the annual mean changes in the Kuroshio and NEC bifurcation during the LGM were examined using downscaled MIROC4m and other 9 climate models from PMIP3/4. The ensemble mean of the 10 models showed that the Kuroshio axis migrated slightly seaward with an increase in volume transport in the ECS (Figure 5.1). While the southward shift (0.2 ± 0.8°) of the zero wind-stress curl was insignificant, the LGM-Kuroshio section at 146° E shifted southward by 0.8–3.1° in 10 models with an average southward shift of 2.0 ± 0.7° relative to the present position.

We compared the zonally integrated volume transport at 137° E with the corresponding wind-driven Sverdrup transport and suggested that the subtropical gyre during the LGM became stronger and migrated southward due to the wind-stress curl in the North Pacific, especially from 14.6 to 31° N. Furthermore, the ensemble of the zero wind-stress curl from 10 models revealed a southward shift of 0.5°, corresponding to the southward movement of NEC bifurcation at the surface (0.7°) and 500 m (2.5°). However, the zero wind-stress curl exhibited large differences in latitudinal shift for different LGM models. It appears that the latitudinal shift of the NEC bifurcation at the surface does not fully correspond to the location of the zero wind-stress curl.

The spatial distribution of ΔSSTs showed a cooling of 1.9 ± 0.5°C in 15° S–15° N latitude band at LGM. In the ECS, there was a significant cooling exceeding 5°C on the nearshore side along the KC axis and a cooling of 1–2°C on the offshore side. The SST in the northern Okinawa Trough appeared to be intensely cooled at the LGM, up to 4–5°C. Additionally, the SST cooling at LGM exceeded 6° in the Japan Sea and the Kuroshio–Oyashio confluence region at 40° N, with large standard deviations. To evaluate the 10 LGM model simulations, available ΔSSTs derived from $U_{37}^{K'}$, oxygen isotopes, and Mg/Ca ratios were compared to the respective simulated values in the Kuroshio region (0–38° N, 100°–180° E). GISS-E2-R in PMIP3 performed best in simulating ΔSSTs, with the highest correlation coefficient and lowest normalized centered root-mean-square difference. In contrast, MIROC-ES2L in PMIP4 performed the poorest, with the largest difference from the observations, especially for the summer ΔSSTs.

Second, the LGM results in MIROC4m were comparable to the ensemble mean results of ten climate models in terms of black current path, intensity, and ΔSST; therefore, we further investigated the changes in the Kuroshio system from 35 ka BP to the present using MIROC4m data for different paleo-ages (6 ka BP, LGM, 30 ka BP, and 35 ka BP). Relative to the present, the Kuroshio during the last glacial period traveled the same path with a higher surface velocity in the ECS, while it migrated northward south of Japan and southward in the KE region. The northern limit of the KE axis at 6 ka BP, LGM, 30 ka BP, and 35 ka BP exhibited southward migrations of 1.1, 1.9, 2.0, and 2.4°, respectively. It was found that the southward migrations of the KE axes were closely related to the zero wind-stress curl positions.

The upper 1000 m depth-integrated volume transport stream function was calculated from the annual mean velocity and showed that the North Pacific subtropical gyre during the glacial period strengthened, and shifted southward. Compared to the wind-driven Sverdrup transport, the transport of the enhanced subtropical gyre could be explained by the stronger wind stress curl from 13 to 25° N. To a certain extent, stronger glacial trade winds enhanced the NEC. Consequently, the Kuroshio transport increased in the southern and middle Okinawa Trough.

NEC bifurcation divides NEC into KC and MC, which affects the intensity of the KC. The NEC bifurcations at 0 ka BP were located at 13.3° N and 17.3° N at the surface and 500 m, respectively. The position of the bifurcation shifted poleward with increasing depth, which also occurred in the paleo-ocean. Compared to the modern location of NEC bifurcation, the bifurcation latitude at the surface (500 m) moves southward about 0.1° (0°), 0.9° (2.9°), 1.0° (3.0°), and 0.7° (2.4°) at 6 ka BP, LGM, 30 and 35 ka BP, respectively. The southward movement at the surface agreed with the shifts in the zero-wind stress curl lines. However, the bifurcation latitude slope was not completely determined by the ratio of the wind stress curl intensity of the subtropical gyre to that of the tropical gyre.

In the North Pacific subtropical region, the SST at 6 ka BP became cooler in the western area and slightly warmer in the eastern band-like area, and SST cooling was most significant at the LGM. Moreover, the SST cooling east of the Ryukyu Islands was up to 0.5°C at 6 ka BP, 2–3°C at LGM, and 1–2°C at 30 and 35 ka BP relative to the present SST. In the ECS along the Kuroshio path, SST cooling was greater on the nearshore side than on the offshore side. In the northern ECS, the SST cooling was significant, reaching 4–5℃ at LGM and 3–4℃ at 30 ka and 35 ka BP. The modeled SSTs were used to confirm that the horizontal gradient of the subsurface temperature is a better indicator than the upper-ocean vertical thermal gradient, which is a commonly used index in paleoceanography.

5.2 Future work

The subjects of analysis in this study were the annual mean results. Considering the seasonal variability of the Kuroshio axis, volume transport, and location of the NEC bifurcation in the present ocean (Nakamura, 2020), did a similar seasonality exist in the paleo-ocean during changes in climate and sea level? Our model is driven by monthly climatological data, which can be used to analyze seasonal variations in the Kuroshio system.

We found that the latitudinal migration of the NEC bifurcation does not correspond to the shift of the zero wind-stress curl, and its poleward tilting degree with increasing depth is fully determined by the ratio of the wind-stress curl intensity of the subtropical gyre to that of the tropical gyre. Therefore, in addition to the effect of the wind field, the effect of air-sea heat flux on the location of NEC bifurcation requires further investigation. In addition, the gyre strength north of 31° N is not consistent with wind-driven Sverdrup transport, which is suspected to be influenced by air-sea heat flux. Hence, the influence of air-sea heat flux on NEC bifurcation gyre strength needs to be explored in the future.

Figures

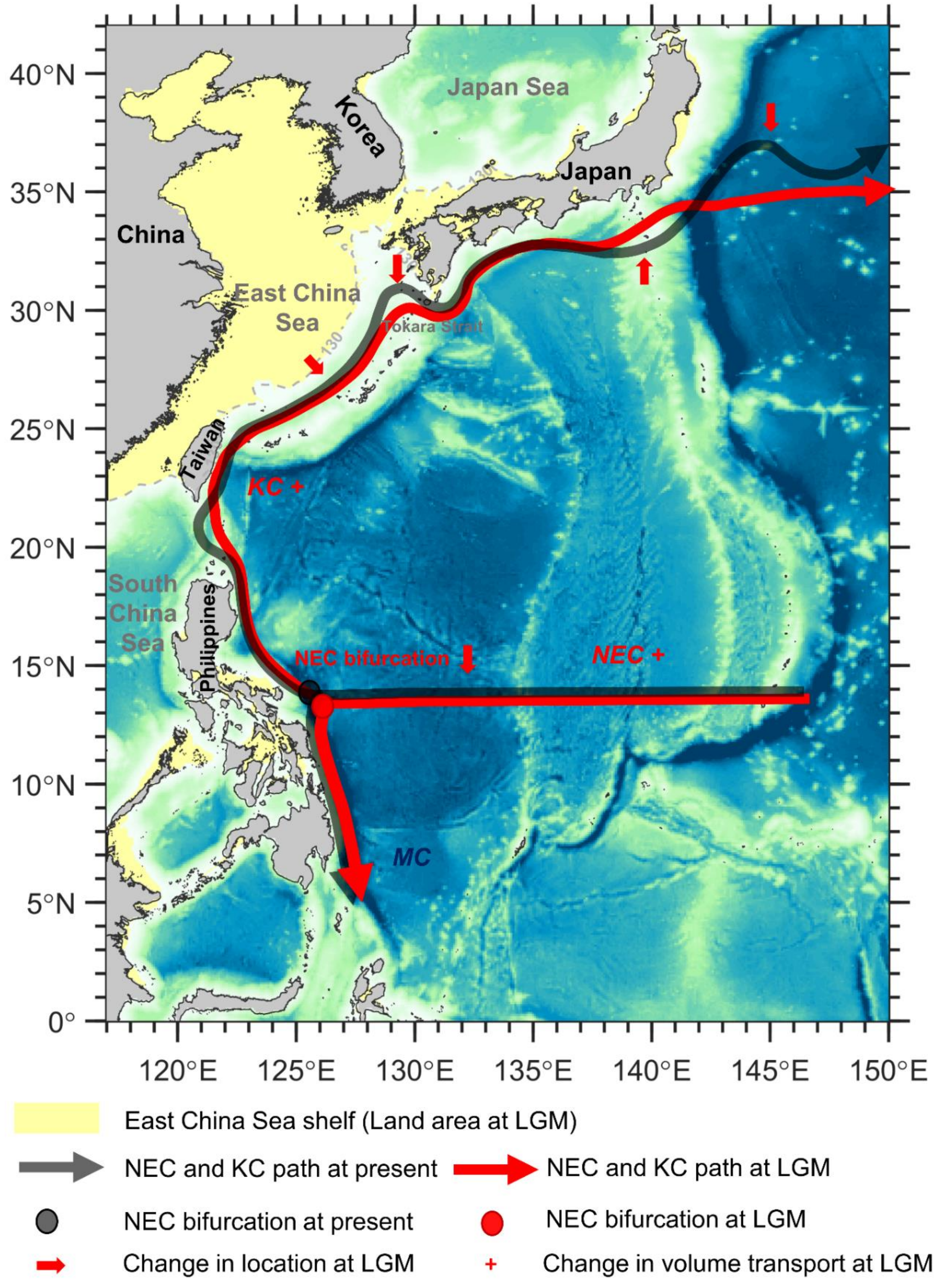

Figure 5.1 The NEC and KC paths at present and during the LGM. Red arrows indicate the migration of the axis at LGM relative to the present. Red + denotes an increase in the volume transport at LGM.

References

Abe-Ouchi, A., Saito, F., Kageyama, M., Braconnot, P., Harrison, S. P., Lambeck, K., Otto-Bliesner, B. L., Peltier, W. R., Tarasov, L., Peterschmitt, J.-Y., & Takahashi, K. (2015). Ice-sheet configuration in the CMIP5/PMIP3 Last Glacial Maximum experiments. *Geoscientific Model Development*, *8*(11), 3621–3637. https://doi.org/10.5194/gmd-8-3621-2015

Ahagon, N., Tanaka, Y., & Ujiié, H. (1993). Florisphaera profunda, a possible nannoplankton indicator of late Quaternary changes in sea-water turbidity at the northwestern margin of the Pacific. *Marine Micropaleontology*, *22*(3), 255–273. https://doi.org/10.1016/0377-8398(93)90047-2

Amano, A., & Itaki, T. (2016). Variations in sedimentary environments in the forearc and backarc regions of the Ryukyu Arc since 25 ka based on CNS analysis of sediment cores. *Quaternary International*, *397*, 360–372. https://doi.org/10.1016/j.quaint.2015.06.017

Amante, C., & Eakins, B. W. (2009). ETOPO1 1 arc-minute global relief model: Procedures, data sources and analysis. US Department of Commerce, National Oceanic and Atmospheric Administration, National Environmental Satellite, Data, and Information Service, National Geophysical Data Center. *Marine Geology and Geophysics Division*, *19*.

Ambe, D., Imawaki, S., Uchida, H., & Ichikawa, K. (2004). Estimating the Kuroshio Axis South of Japan Using Combination of Satellite Altimetry and Drifting Buoys. *Journal of Oceanography*, *60*(2), 375–382. https://doi.org/10.1023/B:JOCE.0000038343.31468.fe

Annan, J. D., & Hargreaves, J. C. (2013). A new global reconstruction of temperature changes at the Last Glacial Maximum. *Climate of the Past*, *9*(1), 367–376. https://doi.org/10.5194/cp-9-367-2013

Chan, W.-L., Abe-Ouchi, A., & Ohgaito, R. (2011). Simulating the mid-Pliocene climate with the MIROC general circulation model: Experimental design and initial results. *Geoscientific Model Development*, *4*(4), 1035–1049. https://doi.org/10.5194/gmd-4-1035-2011

Chang, Y.-P., Wang, W.-L., Yokoyama, Y., Matsuzaki, H., Kawahata, H., & Chen, M.-T. (2008). Millennial-Scale Planktic Foraminifer Faunal Variability in the East China Sea during the Past 40000 Years (IMAGES MD012404 from the Okinawa Trough). *Terrestrial, Atmospheric & Oceanic Sciences*, *19*(4). https://doi.org/10.3319/TAO.2008.19.4.389(IMAGES)

Chen, Z., & Wu, L. (2012). Long-term change of the Pacific North Equatorial Current bifurcation in SODA. *Journal of Geophysical Research: Oceans*, *117*(C6), C06016. https://doi.org/10.1029/2011JC007814

Clark, P. U., Dyke, A. S., Shakun, J. D., Carlson, A. E., Clark, J., Wohlfarth, B., Mitrovica, J. X., Hostetler, S. W., & McCabe, A. M. (2009). The Last Glacial Maximum. *Science*, *325*(5941), 710–714. https://doi.org/10.1126/science.1172873

Dang, H., Jian, Z., Bassinot, F., Qiao, P., & Cheng, X. (2012). Decoupled Holocene variability in surface and thermocline water temperatures of the Indo-Pacific Warm Pool. *Geophysical Research Letters*, *39*(1). https://doi.org/10.1029/2011GL050154

Delworth, T. L., Rosati, A., Anderson, W., Adcroft, A. J., Balaji, V., Benson, R., Dixon, K., Griffies, S. M., Lee, H.-C., Pacanowski, R. C., Vecchi, G. A., Wittenberg, A. T., Zeng, F., & Zhang, R. (2012). Simulated Climate and Climate Change in the GFDL CM2.5 High-Resolution Coupled Climate Model. *Journal of Climate*, *25*(8), 2755–2781. https://doi.org/10.1175/JCLI-D-11-00316.1

Ford, H. L., Ravelo, A. C., & Polissar, P. J. (2015). Reduced El Nino-Southern Oscillation during the Last Glacial Maximum. *Science*, *347*(6219), 255–258. https://doi.org/10.1126/science.1258437

Gallagher, S. J., Kitamura, A., Iryu, Y., Itaki, T., Koizumi, I., & Hoiles, P. W. (2015). The Pliocene to recent history of the Kuroshio and Tsushima Currents: A multi-proxy approach. *Progress in Earth and Planetary Science*, *2*(1), 17. https://doi.org/10.1186/s40645-015-0045-6

Gent, P. R., Danabasoglu, G., Donner, L. J., Holland, M. M., Hunke, E. C., Jayne, S. R., Lawrence, D. M., Neale, R. B., Rasch, P. J., Vertenstein, M., Worley, P. H., Yang, Z.-L., & Zhang, M. (2011). The Community Climate System Model Version 4. *Journal of Climate*, *24*(19), 4973–4991. https://doi.org/10.1175/2011JCLI4083.1

Gray, W. R., Wills, R. C. J., Rae, J. W. B., Burke, A., Ivanovic, R. F., Roberts, W. H. G., Ferreira, D., & Valdes, P. J. (2020). Wind-Driven Evolution of the North Pacific Subpolar Gyre Over the Last Deglaciation. *Geophysical Research Letters*, *47*(6). https://doi.org/10.1029/2019GL086328

Griffies, S. M., Winton, M., Anderson, W. G., Benson, R., Delworth, T. L., Dufour, C. O., Dunne, J. P., Goddard, P., Morrison, A. K., Rosati, A., Wittenberg, A. T., Yin, J., & Zhang, R. (2015). Impacts on Ocean Heat from Transient Mesoscale Eddies in a Hierarchy of Climate Models. *Journal of Climate*, *28*(3), 952–977. https://doi.org/10.1175/JCLI-D-14-00353.1

Guo, H., Chen, Z., & Yang, H. (2019). Poleward Shift of the Pacific North Equatorial Current Bifurcation. *Journal of Geophysical Research: Oceans*, *124*(7), 4557–4571. https://doi.org/10.1029/2019JC015019

Harada, N., Ahagon, N., Uchida, M., & Murayama, M. (2004). Northward and southward migrations of frontal zones during the past 40 kyr in the Kuroshio-Oyashio transition area. *Geochemistry, Geophysics, Geosystems*, *5*(9). https://doi.org/10.1029/2004GC000740

Hewitt, H. T., Roberts, M., Mathiot, P., Biastoch, A., Blockley, E., Chassignet, E. P., Fox-Kemper, B., Hyder, P., Marshall, D. P., Popova, E., Treguier, A.-M., Zanna, L., Yool, A., Yu, Y., Beadling, R., Bell, M., Kuhlbrodt, T., Arsouze, T., Bellucci, A., … Zhang, Q. (2020). Resolving and Parameterising the Ocean Mesoscale in Earth System Models. *Current Climate Change Reports*, *6*(4), 137–152. https://doi.org/10.1007/s40641-020-00164-w

Hinada, T. (1996). Seasonal variation and long-term trends of the oceanographic conditions along a fixed hydrographic line crossing the Kuroshio in the East China Sea. *Oceanogr. Mag.*, *45*, 9–32.

Hogg, A. McC., & Gayen, B. (2020). Ocean Gyres Driven by Surface Buoyancy Forcing. *Geophysical Research Letters*, *47*(16). https://doi.org/10.1029/2020GL088539

Hu, D., Wu, L., Cai, W., Gupta, A. S., Ganachaud, A., Qiu, B., Gordon, A. L., Lin, X., Chen, Z., Hu, S., Wang, G., Wang, Q., Sprintall, J., Qu, T., Kashino, Y., Wang, F., & Kessler, W. S. (2015). Pacific western boundary currents and their roles in climate. *Nature*, *522*(7556), 299–308. https://doi.org/10.1038/nature14504

Ijiri, A., Wang, L., Oba, T., Kawahata, H., Huang, C.-Y., & Huang, C.-Y. (2005). Paleoenvironmental changes in the northern area of the East China Sea during the past 42,000 years. *Palaeogeography, Palaeoclimatology, Palaeoecology*, *219*(3–4), 239–261. https://doi.org/10.1016/j.palaeo.2004.12.028

Ivanovic, R. F., Gregoire, L. J., Kageyama, M., Roche, D. M., Valdes, P. J., Burke, A., Drummond, R., Peltier, W. R., & Tarasov, L. (2016). Transient climate simulations of the deglaciation 21–9 thousand years before present (version 1) – PMIP4 Core experiment design and boundary conditions. *Geoscientific Model Development*, *9*(7), 2563–2587. https://doi.org/10.5194/gmd-9-2563-2016

Jia, G., Zhang, J., Chen, J., Peng, P., & Zhang, C. L. (2012). Archaeal tetraether lipids record subsurface water temperature in the South China Sea. *Organic Geochemistry*, *50*, 68–77. https://doi.org/10.1016/j.orggeochem.2012.07.002

Johns, W. E., Lee, T. N., Zhang, D., Zantopp, R., Liu, C.-T., & Yang, Y. (2001). The Kuroshio East of Taiwan: Moored Transport Observations from the WOCE PCM-1 Array. *Journal of Physical Oceanography*, *31*(4), 1031–1053. https://doi.org/10.1175/1520-0485(2001)031<1031:TKEOTM>2.0.CO;2

Jordi, A., & Wang, D.-P. (2012). sbPOM: A parallel implementation of Princenton Ocean Model. *Environmental Modelling & Software*, *38*, 59–61. https://doi.org/10.1016/j.envsoft.2012.05.013

Kageyama, M., Harrison, S. P., Kapsch, M.-L., Lofverstrom, M., Lora, J. M., Mikolajewicz, U., Sherriff-Tadano, S., Vadsaria, T., Abe-Ouchi, A., Bouttes, N., Chandan, D., Gregoire, L. J., Ivanovic, R. F., Izumi, K., LeGrande, A. N., Lhardy, F., Lohmann, G., Morozova, P. A., Ohgaito, R., … Zhu, J. (2021). The PMIP4 Last Glacial Maximum experiments: Preliminary results and comparison with the PMIP3 simulations. *Climate of the Past*, *17*(3), 1065–1089. https://doi.org/10.5194/cp-17-1065-2021

Kageyama, M., Merkel, U., Otto-Bliesner, B., Prange, M., Abe-Ouchi, A., Lohmann, G., Ohgaito, R., Roche, D. M., Singarayer, J., Swingedouw, D., & X Zhang. (2013). Climatic impacts of fresh water hosing under Last Glacial Maximum conditions: A multi-model study. *Climate of the Past*, *9*(2), 935–953. https://doi.org/10.5194/cp-9-935-2013

Kao, S. J., Wu, C.-R., Hsin, Y.-C., & Dai, M. (2006). Effects of sea level change on the upstream Kuroshio Current through the Okinawa Trough. *Geophysical Research Letters*, *33*(16). https://doi.org/10.1029/2006GL026822

Kawahata, H., & Ohshima, H. (2002). Small latitudinal shift in the Kuroshio Extension (Central Pacific) during glacial times: Evidence from pollen transport. *Quaternary Science Reviews*, *21*(14–15), 1705–1717. https://doi.org/10.1016/S0277-3791(01)00150-0

Kawahata, H., & Ohshima, H. (2004). Vegetation and environmental record in the northern East China Sea during the late Pleistocene. *Global and Planetary Change*, *41*(3–4), 251–273. https://doi.org/10.1016/j.gloplacha.2004.01.011

Kim, R. A., Lee, K. E., & Bae, S. W. (2015). Sea surface temperature proxies (alkenones, foraminiferal Mg/Ca, and planktonic foraminiferal assemblage) and their implications in the Okinawa Trough. *Progress in Earth and Planetary Science*, *2*(1), 43. https://doi.org/10.1186/s40645-015-0074-1

Kim, S., Son, H.-Y., & Kug, J.-S. (2017). How well do climate models simulate atmospheric teleconnctions over the North Pacific and East Asia associated with ENSO? *Climate Dynamics*, *48*(3–4), 971–985. https://doi.org/10.1007/s00382-016-3121-8

Kim, Y. Y., Qu, T., Jensen, T., Miyama, T., Mitsudera, H., Kang, H.-W., & Ishida, A. (2004). Seasonal and interannual variations of the North Equatorial Current bifurcation in a high-resolution OGCM. *Journal of Geophysical Research: Oceans*, *109*(C3). https://doi.org/10.1029/2003JC002013

Kirtman, B. P., Bitz, C., Bryan, F., Collins, W., Dennis, J., Hearn, N., Kinter, J. L., Loft, R., Rousset, C., Siqueira, L., Stan, C., Tomas, R., & Vertenstein, M. (2012). Impact of ocean model resolution on CCSM climate simulations. *Climate Dynamics*, *39*(6), 1303–1328. https://doi.org/10.1007/s00382-012-1500-3

Kondo, J. (1975). Air-sea bulk transfer coefficients in diabatic conditions. *Boundary-Layer Meteorology*, *9*(1), 91–112. https://doi.org/10.1007/BF00232256

Kubota, Y., Kimoto, K., Tada, R., Oda, H., Yokoyama, Y., & Matsuzaki, H. (2010). Variations of East Asian summer monsoon since the last deglaciation based on Mg/Ca and oxygen isotope of planktic foraminifera in the northern East China Sea. *Paleoceanography*, *25*(4), n/a-n/a. https://doi.org/10.1029/2009PA001891

Kubota, Y., Suzuki, N., Kimoto, K., Uchida, M., Itaki, T., Ikehara, K., Kim, R. A., & Lee, K. E. (2017). Variation in subsurface water temperature and its link to the Kuroshio Current in the Okinawa Trough during the last 38.5 kyr. *Quaternary International*, *452*, 1–11. https://doi.org/10.1016/j.quaint.2017.06.021

Lambeck, K., Rouby, H., Purcell, A., Sun, Y., & Sambridge, M. (2014). Sea level and global ice volumes from the Last Glacial Maximum to the Holocene. *Proceedings of the National Academy of Sciences*, *111*(43), 15296–15303. https://doi.org/10.1073/pnas.1411762111

Lee, K. E., Lee, H. J., Park, J.-H., Chang, Y.-P., Ikehara, K., Itaki, T., & Kwon, H. K. (2013). Stability of the Kuroshio path with respect to glacial sea level lowering. *Geophysical Research Letters*, *40*(2), 392–396. https://doi.org/10.1002/grl.50102

Li, D., Zhao, M., Tian, J., & Li, L. (2013). Comparison and implication of TEX^{H}_{86} and $U^{K'}_{37}$ temperature records over the last 356 kyr of ODP Site 1147 from the northern South China Sea. *Palaeogeography, Palaeoclimatology, Palaeoecology*, *376*, 213–223. https://doi.org/10.1016/j.palaeo.2013.02.031

Li, D.-W., Chang, Y.-P., Li, Q., Zheng, L., Ding, X., & Kao, S.-J. (2018). Effect of sea-level on organic carbon preservation in the Okinawa Trough over the last 91 kyr. *Marine Geology*, *399*, 148–157. https://doi.org/10.1016/j.margeo.2018.02.013

Li, J., & Gan, J. (2022). On the North Equatorial Current Spatiotemporal Modes and Responses in the Western Boundary Currents. *Progress in Oceanography*, 102820. https://doi.org/10.1016/j.pocean.2022.102820

Li, Q., Li, G., Chen, M., Xu, J., Liu, S., & Chen, M. (2020). New insights into Kuroshio Current evolution since the last deglaciation based on paired organic paleothermometers from the middle Okinawa Trough. *Paleoceanography and Paleoclimatology*, *35*(12). https://doi.org/10.1029/2020PA004140

Lin, D.-C., Chen, M.-T., Yamamoto, M., & Yokoyama, Y. (2017). Hydrographic variability in the northern South China Sea over the past 45,000 years: New insights based on temperature reconstructions by $U^{K'}_{37}$ and TEX^{H}_{86} proxies from a marine sediment core (MD972146). *Quaternary International*, *459*, 1–16. https://doi.org/10.1016/j.quaint.2017.09.029

Locarnini, R., Mishonov, A., K Baranova, O., P Boyer, T., M Zweng, M., Garcia, H., Reagan, J., Seidov, D., W Weathers, K., R Paver, C., V Smolyar, I., & A Locarnini, R. (2019). *World Ocean Atlas 2018, Volume 1: Temperature*.

Lukas, R., Firing, E., Hacker, P., Richardson, P. L., Collins, C. A., Fine, R., & Gammon, R. (1991). Observations of the Mindanao Current during the western equatorial Pacific Ocean circulation study. *Journal of Geophysical Research*, *96*(C4), 7089. https://doi.org/10.1029/91JC00062

Mauritsen, T., & Roeckner, E. (2020). Tuning the MPI-ESM1.2 Global Climate Model to Improve the Match With Instrumental Record Warming by Lowering Its Climate Sensitivity. *Journal of Advances in Modeling Earth Systems*, *12*(5). https://doi.org/10.1029/2019MS002037

Monteagudo, M. M., Lynch-Stieglitz, J., Marchitto, T. M., & Schmidt, M. W. (2021). Central Equatorial Pacific Cooling During the Last Glacial Maximum. *Geophysical Research Letters*, *48*(3). https://doi.org/10.1029/2020GL088592

Nagano, A., Ichikawa, K., Ichikawa, H., Tomita, H., Tokinaga, H., & Konda, M. (2010). Stable volume and heat transports of the North Pacific subtropical gyre revealed by identifying the Kuroshio in synoptic hydrography south of Japan. *Journal of Geophysical Research*, *115*(C9), C09002. https://doi.org/10.1029/2009JC005747

Nakamura, H. (2020). Changing Kuroshio and Its Affected Shelf Sea: A Physical View. In C.-T. A. Chen & X. Guo (Eds.), *Changing Asia-Pacific Marginal Seas* (pp. 265–305). Springer Singapore. https://doi.org/10.1007/978-981-15-4886-4_15

Nonaka, M., Sasaki, H., Taguchi, B., & Nakamura, H. (2012). Potential Predictability of Interannual Variability in the Kuroshio Extension Jet Speed in an Eddy-Resolving OGCM. *Journal of Climate*, *25*(10), 3645–3652. https://doi.org/10.1175/JCLI-D-11-00641.1

Nooteboom, P. D., Baatsen, M., Bijl, P. K., Kliphuis, M. A., van Sebille, E., Sluijs, A., Dijkstra, H. A., & von der Heydt, A. S. (2022). Improved Model-Data Agreement With Strongly Eddying Ocean Simulations in the Middle-Late Eocene. *Paleoceanography and Paleoclimatology*, *37*(8). https://doi.org/10.1029/2021PA004405

Nooteboom, P. D., Delandmeter, P., van Sebille, E., Bijl, P. K., Dijkstra, H. A., & von der Heydt, A. S. (2020). Resolution dependency of sinking Lagrangian particles in ocean general circulation models. *PLOS ONE*, *15*(9), e0238650. https://doi.org/10.1371/journal.pone.0238650

Ohgaito, R., Sueyoshi, T., Abe-Ouchi, A., Hajima, T., Watanabe, S., Kim, H.-J., Yamamoto, A., & Kawamiya, M. (2013). Can an Earth System Model simulate better climate change at mid-Holocene than an AOGCM? A comparison study of MIROC-ESM and MIROC3. *Climate of the Past*, *9*(4), 1519–1542. https://doi.org/10.5194/cp-9-1519-2013

Ohgaito, R., Yamamoto, A., Hajima, T., O'ishi, R., Abe, M., Tatebe, H., Abe-Ouchi, A., & Kawamiya, M. (2021). PMIP4 experiments using MIROC-ES2L Earth system model. *Geoscientific Model Development*, *14*(2), 1195–1217. https://doi.org/10.5194/gmd-14-1195-2021

O'ishi, R., & Abe-Ouchi, A. (2011). Polar amplification in the mid-Holocene derived from dynamical vegetation change with a GCM: MID-HOLOCENE WARMING BY DYNAMIC VEGETATION. *Geophysical Research Letters*, *38*(14). https://doi.org/10.1029/2011GL048001

Peltier, W. R., Argus, D. F., & Drummond, R. (2015). Space geodesy constrains ice age terminal deglaciation: The global ICE-6G_C (VM5a) model: Global Glacial Isostatic Adjustment. *Journal of Geophysical Research: Solid Earth*, *120*(1), 450–487. https://doi.org/10.1002/2014JB011176

Qiu, B. (2003). Kuroshio Extension Variability and Forcing of the Pacific Decadal Oscillations: Responses and Potential Feedback. *Journal of Physical Oceanography*, *33*(12), 2465–2482. https://doi.org/10.1175/2459.1

Qiu, B., & Chen, S. (2010). Interannual-to-Decadal Variability in the Bifurcation of the North Equatorial Current off the Philippines. *Journal of Physical Oceanography*, *40*(11), 2525–2538. https://doi.org/10.1175/2010JPO4462.1

Qiu, B., Chen, S., Schneider, N., & Taguchi, B. (2014). A Coupled Decadal Prediction of the Dynamic State of the Kuroshio Extension System. *Journal of Climate*, *27*(4), 1751–1764. https://doi.org/10.1175/JCLI-D-13-00318.1

Qiu, B., Nakano, T., Chen, S., & Klein, P. (2017). Submesoscale transition from geostrophic flows to internal waves in the northwestern Pacific upper ocean. *Nature Communications*, *8*, 14055. https://doi.org/10.1038/ncomms14055

Qu, T., & Lukas, R. (2003). The Bifurcation of the North Equatorial Current in the Pacific. *Journal of Physical Oceanography*, *33*, 14. https://doi.org/10.1175/1520-0485(2003)033<0005:TBOTNE>2.0.CO;2

Raddatz, T. J., Reick, C. H., Knorr, W., Kattge, J., Roeckner, E., Schnur, R., Schnitzler, K.-G., Wetzel, P., & Jungclaus, J. (2007). Will the tropical land biosphere dominate the climate–carbon cycle feedback during the twenty-first century? *Climate Dynamics*, *29*(6), 565–574. https://doi.org/10.1007/s00382-007-0247-8

Rio, M.-H., Mulet, S., & Picot, N. (2014). Beyond GOCE for the ocean circulation estimate: Synergetic use of altimetry, gravimetry, and in situ data provides new insight into geostrophic and Ekman currents: Ocean circulation beyond GOCE. *Geophysical Research Letters*, *41*(24), 8918–8925. https://doi.org/10.1002/2014GL061773

Ruan, J., Xu, Y., Ding, S., Wang, Y., & Zhang, X. (2017). A biomarker record of temperature and phytoplankton community structure in the Okinawa Trough since the last glacial maximum. *Quaternary Research*, *88*(1), 89–97. https://doi.org/10.1017/qua.2017.28

Sagawa, T., Yokoyama, Y., Ikehara, M., & Kuwae, M. (2011). Vertical thermal structure history in the western subtropical North Pacific since the Last Glacial Maximum. *Geophysical Research Letters*, *38*(8). https://doi.org/10.1029/2010GL045827

Saito, H., Suzuki, K., Takahashi, M., & Nagai, T. (2019). *Kuroshio current physical, biogeochemical, and ecosystem dynamics*. https://onlinelibrary.wiley.com/doi/book/10.1002/9781119428428

Sasaki, Y. N., & Schneider, N. (2011). Decadal Shifts of the Kuroshio Extension Jet: Application of Thin-Jet Theory*. *Journal of Physical Oceanography*, *41*(5), 979–993. https://doi.org/10.1175/2011JPO4550.1

Sawada, K., & Handa, N. (1998). Variability of the path of the Kuroshio ocean current over the past 25,000 years. *Nature*, *392*(6676), 592–595. https://doi.org/10.1038/33391

Schmidt, G. A., Ruedy, R., Hansen, J. E., Aleinov, I., Bell, N., Bauer, M., Bauer, S., Cairns, B., Canuto, V., Cheng, Y., Del Genio, A., Faluvegi, G., Friend, A. D., Hall, T. M., Hu, Y., Kelley, M., Kiang, N. Y., Koch, D., Lacis, A. A., … Yao, M.-S. (2006). Present-Day Atmospheric Simulations Using GISS ModelE: Comparison to In Situ, Satellite, and Reanalysis Data. *Journal of Climate*, *19*(2), 153–192. https://doi.org/10.1175/JCLI3612.1

Schönau, M. C., & Rudnick, D. L. (2015). Glider observations of the North Equatorial Current in the western tropical Pacific. *Journal of Geophysical Research: Oceans*, *120*(5), 3586–3605. https://doi.org/10.1002/2014JC010595

Schönau, M., Rudnick, D., Cerovecki, I., Gopalakrishnan, G., Cornuelle, B., McClean, J., & Qiu, B. (2015). The Mindanao Current: Mean Structure and Connectivity. *Oceanography*, *28*(4), 34–45. https://doi.org/10.5670/oceanog.2015.79

Seo, I., Lee, Y., Yoo, C. M., & Hyeong, K. (2018). Migration of the Kuroshio Extension in the Northwest Pacific since the Last Glacial Maximum. *Palaeogeography, Palaeoclimatology, Palaeoecology*, *496*, 323–331. https://doi.org/10.1016/j.palaeo.2018.01.048

Sherriff-Tadano, S., Abe-Ouchi, A., Yoshimori, M., Oka, A., & Chan, W.-L. (2018). Influence of glacial ice sheets on the Atlantic meridional overturning circulation through surface wind change. *Climate Dynamics*, *50*(7–8), 2881–2903. https://doi.org/10.1007/s00382-017-3780-0

Shi, X., Lohmann, G., Sidorenko, D., & Yang, H. (2020). Early-Holocene simulations using different forcings and resolutions in AWI-ESM. *The Holocene*, *30*(7), 996–1015. https://doi.org/10.1177/0959683620908634

Shi, X., Wu, Y., Zou, J., Liu, Y., Ge, S., Zhao, M., Liu, J., Zhu, A., Meng, X., Yao, Z., & Han, Y. (2014). Multiproxy reconstruction for Kuroshio responses to northern hemispheric oceanic climate and the Asian Monsoon since Marine Isotope Stage 5.1 (∼88 ka). *Climate of the Past*, *10*(5), 1735–1750. https://doi.org/10.5194/cp-10-1735-2014

Sun, Y., Oppo, D. W., Xiang, R., Liu, W., & Gao, S. (2005). Last deglaciation in the Okinawa Trough: Subtropical northwest Pacific link to Northern Hemisphere and tropical climate. *Paleoceanography*, *20*(4). https://doi.org/10.1029/2004PA001061

Sverdrup, H. U. (1947). Wind-Driven Currents in a Baroclinic Ocean; with Application to the Equatorial Currents of the Eastern Pacific. *Proceedings of the National Academy of Sciences*, *33*(11), 318–326. https://doi.org/10.1073/pnas.33.11.318

Talley, L. D., Pickard, G. L., & Emery, W. J. (Eds.). (2011). *Descriptive physical oceanography: An introduction* (6th ed). Academic Press.

Taylor, K. E. (2001). Summarizing multiple aspects of model performance in a single diagram. *Journal of Geophysical Research: Atmospheres*, *106*(D7), 7183–7192. https://doi.org/10.1029/2000JD900719

Thompson, P. R. (1981). Planktonic foraminifera in the Western North Pacific during the past 150 000 years: Comparison of modern and fossil assemblages. *Palaeogeography, Palaeoclimatology, Palaeoecology*, *35*, 241–279. https://doi.org/10.1016/0031-0182(81)90099-7

Thompson, P. R., & Shackleton, N. J. (1980). North Pacific palaeoceanography: Late Quaternary coiling variations of planktonic foraminifer Neogloboquadrina pachyderma. *Nature*, *287*(5785), 829–833. https://doi.org/10.1038/287829a0

Tierney, J. E., Zhu, J., King, J., Malevich, S. B., Hakim, G. J., & Poulsen, C. J. (2020). Glacial cooling and climate sensitivity revisited. *Nature*, *584*(7822), 569–573. https://doi.org/10.1038/s41586-020-2617-x

Toole, J. M., Millard, R. C., Wang, Z., & Pu, S. (1990). Observations of the Pacific North Equatorial Current Bifurcation at the Philippine Coast. *Journal of Physical Oceanography*, *20*(2), 307–318. https://doi.org/10.1175/1520-0485(1990)020<0307:OOTPNE>2.0.CO;2

Ujiié, H., Tanaka, Y., & Ono, T. (1991). Late Quarternary paleoceanographic record from the middle Ryukyu Trench slope, northwest Pacific. *Marine Micropaleontology*, *18*(1–2), 115–128. https://doi.org/10.1016/0377-8398(91)90008-T

Ujiié, H., & Ujiié, Y. (1999). Late Quaternary course changes of the Kuroshio Current in the Ryukyu Arc region, northwestern Pacific Ocean. *Marine Micropaleontology*, *37*(1), 23–40. https://doi.org/10.1016/S0377-8398(99)00010-9

Ujiié, Y., Asahi, H., Sagawa, T., & Bassinot, F. (2016). Evolution of the North Pacific Subtropical Gyre during the past 190 kyr through the interaction of the Kuroshio Current with the surface and intermediate waters. *Paleoceanography*, *31*(11), 1498–1513. https://doi.org/10.1002/2015PA002914

Ujiié, Y., Ujiié, H., Taira, A., Nakamura, T., & Oguri, K. (2003). Spatial and temporal variability of surface water in the Kuroshio source region, Pacific Ocean, over the past 21,000 years: Evidence from planktonic foraminifera. *Marine Micropaleontology*, *49*(4), 335–364. https://doi.org/10.1016/S0377-8398(03)00062-8

Vats, N., Mishra, S., Singh, R. K., Gupta, A. K., & Pandey, D. K. (2020). Paleoceanographic changes in the East China Sea during the last ~400 kyr reconstructed using planktic foraminifera. *Global and Planetary Change*, *189*, 103173. https://doi.org/10.1016/j.gloplacha.2020.103173

Vogt-Vincent, N. S., & Mitarai, S. (2020). A persistent Kuroshio in the glacial East China Sea and implications for coral paleobiogeography. *Paleoceanography and Paleoclimatology*, *35*(7). https://doi.org/10.1029/2020PA003902

Voldoire, A., Sanchez-Gomez, E., Salas y Mélia, D., Decharme, B., Cassou, C., Sénési, S., Valcke, S., Beau, I., Alias, A., Chevallier, M., Déqué, M., Deshayes, J., Douville, H., Fernandez, E., Madec, G., Maisonnave, E., Moine, M.-P., Planton, S., Saint-Martin, D., … Chauvin, F. (2013). The CNRM-CM5.1 global climate model: Description and basic evaluation. *Climate Dynamics*, *40*(9), 2091–2121. https://doi.org/10.1007/s00382-011-1259-y

Waelbroeck, C., Paul, A., Kucera, M., Rosell-Melé, A., Weinelt, M., Schneider, R., Mix, A. C., Abelmann, A., Armand, L., Bard, E., Barker, S., Barrows, T. T., Benway, H., Cacho, I., Chen, M.-T., Cortijo, E., Crosta, X., de Vernal, A., Dokken, T., … MARGO Project Members. (2009). Constraints on the magnitude and patterns of ocean cooling at the Last Glacial Maximum. *Nature Geoscience*, *2*(2), Article 2. https://doi.org/10.1038/ngeo411

Wang, L., Li, J., Zhao, J., Wei, H., Hu, B., Dou, Y., Sun, Z., Zou, L., & Bai, F. (2016). Solar-, monsoon- and Kuroshio-influenced thermocline depth and sea surface salinity in the southern Okinawa Trough during the past 17,300 years. *Geo-Marine Letters*, *36*(4), 281–291. https://doi.org/10.1007/s00367-016-0448-4

Wang, N., Jiang, D., & Lang, X. (2018a). Northern westerlies during the Last Glacial Maximum: Results from CMIP5 simulations. *Journal of Climate*, *31*(3), 1135–1153. https://doi.org/10.1175/JCLI-D-17-0314.1

Wang, N., Jiang, D., & Lang, X. (2018b). Northern Westerlies during the Last Glacial Maximum: Results from CMIP5 Simulations. *Journal of Climate*, *31*(3), 1135–1153. https://doi.org/10.1175/JCLI-D-17-0314.1

Wang, Y.-L., & Wu, C.-R. (2018). Discordant multi-decadal trend in the intensity of the Kuroshio along its path during 1993–2013. *Scientific Reports, 8*(1), 14633. https://doi.org/10.1038/s41598-018-32843-y

Wang, Y.-L., Wu, C.-R., & Chao, S.-Y. (2016). Warming and weakening trends of the Kuroshio during 1993-2013. *Geophysical Research Letters*, *43*(17), 9200–9207. https://doi.org/10.1002/2016GL069432

Watanabe, S., Hajima, T., Sudo, K., Nagashima, T., Takemura, T., Okajima, H., Nozawa, T., Kawase, H., Abe, M., Yokohata, T., Ise, T., Sato, H., Kato, E., Takata, K., Emori, S., & Kawamiya, M. (2011). MIROC-ESM 2010: Model description and basic results of CMIP5-20c3m experiments. *Geoscientific Model Development*, *4*(4), 845–872. https://doi.org/10.5194/gmd-4-845-2011

Weiss, T. L., Linsley, B. K., & Gordon, A. L. (2021). Pacific North Equatorial Current bifurcation latitude and Kuroshio Current shifts since the Last Glacial Maximum inferred from a Sulu Sea thermocline reconstruction. *Quaternary Science Reviews*, *264,* 106999. https://doi.org/10.1016/j.quascirev.2021.106999

Xiang, R., Sun, Y., Li, T., Oppo, D. W., Chen, M., & Zheng, F. (2007). Paleoenvironmental change in the middle Okinawa Trough since the last deglaciation: Evidence from the sedimentation rate and planktonic foraminiferal record. *Palaeogeography, Palaeoclimatology, Palaeoecology*, *243*(3–4), 378–393. https://doi.org/10.1016/j.palaeo.2006.08.016

Xu, X., & Oda, M. (1999). Surface-water evolution of the eastern East China Sea during the last 36,000 years. *Marine Geology*, *156*(1–4), 285–304. https://doi.org/10.1016/S0025-3227(98)00183-2

Xu, Z., Li, T., Clift, P. D., Lim, D., Nan, Q., Wan, S., Choi, J., Cai, M., & Chen, H. (2017). Sediment provenance and paleoenvironmental change in the middle Okinawa Trough during the last 18.5 ky: Clay mineral and geochemical evidence. *Quaternary International*, *440*, 139–149. https://doi.org/10.1016/j.quaint.2016.07.058

Yamamoto, M. (2009). Response of mid-latitude North Pacific surface temperatures to orbital forcing and linkage to the East Asian summer monsoon and tropical ocean–atmosphere interactions. *Journal of Quaternary Science*, *24*(8), 836–847. https://doi.org/10.1002/jqs.1255

Yamamoto, M., Kishizaki, M., Oba, T., & Kawahata, H. (2013). Intense winter cooling of the surface water in the northern Okinawa Trough during the last glacial period. *Journal of Asian Earth Sciences*, *69*, 86–92. https://doi.org/10.1016/j.jseaes.2012.06.011

Yamamoto, M., Suemune, R., & Oba, T. (2005). Equatorward shift of the subarctic boundary in the northwestern Pacific during the last deglaciation. *Geophysical Research Letters*, *32*(5). https://doi.org/10.1029/2004gl021903

Yanase, W., & Abe-Ouchi, A. (2010). A numerical study on the atmospheric circulation over the midlatitude North Pacific during the last glacial maximum. *Journal of Climate*, *23*(1), 135–151. https://doi.org/10.1175/2009JCLI3148.1

Yokoyama, Y., Esat, T. M., Thompson, W. G., Thomas, A. L., Webster, J. M., Miyairi, Y., Sawada, C., Aze, T., Matsuzaki, H., & Okuno, J. (2018). Rapid glaciation and a two-step sea level plunge into the Last Glacial Maximum. *Nature*, *559*(7715), 603. https://doi.org/10.1038/s41586-018-0335-4

Yokoyama, Y., Purcell, A., & Ishiwa, T. (2019). Gauging Quaternary Sea Level Changes Through Scientific Ocean Drilling. *Oceanography*, *32*(1), 64–71. https://doi.org/10.5670/oceanog.2019.121

Yukimoto, S., Adachi, Y., Hosaka, M., Sakami, T., Yoshimura, H., Hirabara, M., Tanaka, T. Y., Shindo, E., Tsujino, H., Deushi, M., Mizuta, R., Yabu, S., Obata, A., Nakano, H., Koshiro, T., Ose, T., & Kitoh, A. (2012). A New Global Climate Model of the Meteorological Research Institute: MRI-CGCM3 —Model Description and Basic Performance—. *Journal of the Meteorological Society of Japan. Ser. II*, *90A*(0), 23–64. https://doi.org/10.2151/jmsj.2012-A02

Zhang, Y. G., & Liu, X. (2018). Export Depth of the TEX_{86} Signal. *Paleoceanography and Paleoclimatology*, *33*(7), 666–671. https://doi.org/10.1029/2018PA003337

Zhang, Z., Qiu, B., Tian, J., Zhao, W., & Huang, X. (2018). Latitude-dependent finescale turbulent shear generations in the Pacific tropical-extratropical upper ocean. *Nature Communications*, *9*(1), 4086. https://doi.org/10.1038/s41467-018-06260-8

Zhang, Z., Xue, H., Chai, F., & Chao, Y. (2017). Variability of the Pacific North Equatorial Current from 1993 to 2012 based on a 1/8° Pacific model simulation. *Journal of Geophysical Research: Oceans*, *122*(3), 2382–2400. https://doi.org/10.1002/2016JC012143

Zhao, J., Li, J., Cai, F., Wei, H., Hu, B., Dou, Y., Wang, L., Xiang, R., Cheng, H., Dong, L., & Zhang, C. L. (2015). Sea surface temperature variation during the last deglaciation in the southern Okinawa Trough: Modulation of high latitude teleconnections and the Kuroshio Current. *Progress in Oceanography*, *138*, 238–248. https://doi.org/10.1016/j.pocean.2015.06.008

Zheng, X., Li, A., Kao, S., Gong, X., Frank, M., Kuhn, G., Cai, W., Yan, H., Wan, S., & Zhang, H. (2016). Synchronicity of Kuroshio Current and climate system variability since the

Last Glacial Maximum. *Earth and Planetary Science Letters*, *452*, 247–257. https://doi.org/10.1016/j.epsl.2016.07.028

Zhu, X.-H., Nakamura, H., Dong, M., Nishina, A., & Yamashiro, T. (2017). Tidal currents and Kuroshio transport variations in the Tokara Strait estimated from ferryboat ADCP data. *Journal of Geophysical Research: Oceans*, *122*(3), 2120–2142. https://doi.org/10.1002/2016JC012329

Zweng, M. M., Reagan, J., Seidov, D., Boyer, T., A Locarnini, R., Garcia, H., Mishonov, A., Baranova, O. K., Paver, C., & Smolyar, I. (2019). *WORLD OCEAN ATLAS 2018 Volume 2: Salinity*.

Acknowledgements

I am sincerely grateful to my supervisor Prof. Guo Xinyu for his patient instruction and encouragement in my research. I also appreciate his concern and help in daily life. I want to say thank you to the Prof. Morimoto Akihiko, Prof. Hinata Hirofumi, Prof. Kuwae Michinobu, and Dr. Yoshie Naoki for discussions and suggestions in every seminar. My thanks also go to the other members of CMES for providing great discussions and nice academic atmosphere.

Thanks Prof. Miyazawa Yasumasa and Prof. Sergey M. Varlamov in JASTEC for their help with the model. Thanks to Prof. Ayako Abe-Ouchi and Dr. Wing-Le Chan in Tokyo University providing climate model data for multiple periods, my research was able to proceed smoothly. I appreciate their contributions to my research.

Many thanks to my family for their support. Brothers and sisters in CMES, thank you so much for the happiness you brought to my ordinary days, the generous help you gave me in my life, and the sincere comfort you offered me when I was lost.

Thanks China Scholarship Council (CSC) for supporting my stay in Japan.